MODEL AND DESIGN OF AN AIR-COOLED THERMAL MANAGEMENT SYSTEM FOR AN INTEGRATED MOTOR/CONTROLLER

by

Stephanie I. Mueller

**A thesis submitted in partial fulfillment of
the requirements for the degree of**

MASTER OF SCIENCE
(MECHANICAL ENGINEERING)

at the

UNIVERSITY OF WISCONSIN – MADISON

2005

Model and Design of an Air-Cooled Thermal Management System for an Integrated Motor-Controller

Stephanie I. Mueller

Under the supervision of Professor Greg F. Nellis
at the University of Wisconsin – Madison

ABSTRACT

The use of a remote power supply for conventional induction-type electric motors requires that very high frequency, high power pulse-width modulated signals be transmitted through cables over a significant distance. There are losses inherent in this transmission process as well as problems related to the electro-magnetic interference generated by these cables and reliability issues associated with the cables and interconnects. In addition, the current thin lamination manufacturing method for induction motors results in geometrical restrictions, significant losses, and significant material wastes.

The development of a modular permanent magnet machine that is constructed of identical, individual stator poles that are each closely integrated with their own power electronics module seeks to overcome the issues currently plaguing conventional induction-type electric motors. Combining the stator poles of a permanent magnet motor with their own integrated power electronics module-based drive unit within a motor housing has several advantages including increased reliability and improved efficiencies. However, this integrated approach is challenged by the mismatch in the thermal limits between the motor and IPEM. This thesis describes the development of computational models of the motor, air passages, and IPEM which are integrated in order to identify and design the most attractive thermal management system. An experimental verification follows the model results.

Approved:

Professor Greg F. Nellis
Department of Mechanical Engineering
University of Wisconsin – Madison

Acknowledgements

The research in this thesis could not have been possible without the financial support provided in part by the ERC program of the National Science Foundation under Award Number EEC-9731677 for the Center for Power Electronic Systems and the University of Wisconsin-Madison Graduate School.

Table of Contents

List of Figures

List of Tables

List of Symbols

A_c ..... cross-sectional area

A_{copper} ..... copper cross-sectional area

$A_{insulation}$ ..... insulation cross-sectional area

A_{total} ..... total cross-sectional area of winding

B ..... saturation flux density

c ..... specific heat

C_f ..... coefficient of friction

d ..... diameter

d_c ..... diameter of conductor

D_h ..... hydraulic diameter

f ..... frequency

F ..... force

h ..... heat transfer coefficient

$\overline{h}$ ..... average heat transfer coefficient

I ..... current

K ..... system load factor

$\overline{k}$ ..... equivalent thermal conductivity

k_1 ..... thermal conductivity of copper

k_2 ..... thermal conductivity of wire

k_3 ..... thermal conductivity of air

$k_2^{'}$ ..... equivalent conductivity of wire and air

L ..... length

L_w ..... length of winding

$\dot{m}$ ..... mass flow rate

N ..... number of turns in winding

N_f ..... number of fins

Nu ..... Nusselt number

P ..... pressure

P_w ..... wetted perimeter

Pr ..... Prandlt number

$\dot{q}''$ ..... heat flux

$\dot{q}_{loss}$ ..... total energy lost to air stream

$\dot{Q}$ ..... volumetric flow rate

R ..... resistance

Re ..... Reynolds number

R''_{tc} ..... contact resistance

r_w ..... wire radius

t ..... thickness

t_{gap} ..... air gap length between adjacent wires

T ..... temperature

T_{in} ..... inlet air temperature

T_{out} ..... outlet air temperature

t ..... time

t_{ins} ..... wire insulation thickness

V ..... voltage

v.....velocity

$?$.....efficiency

d.....boundary layer thickness

μ..... viscosity

$?$.....density

t ..... shear stress

F_1 .....copper packing factor

F_2 .....insulation packing factor

F_{12}.....equivalent packing factor

1 Introduction

1.1 Background

Electrical machines are used in a vast array of applications throughout the world. Currently, induction-type electric motors use thin laminations of sheet steel which are punched, annealed, and stacked to form the magnetic core of the device as shown in Fig. 1.1. These separate laminated sheets are electrically insulated from one another by a thin layer of silicon or phosphorous and form an assembly with good mechanical strength and magnetic properties. The practice of using steel laminations instead of a solid iron core was developed in order to reduce eddy current losses in the material and therefore improve the overall efficiency of the motor.

Figure 1.1. Steel stator laminations [1.1].

Eddy currents form when localized currents are induced in the material by an alternating magnetic flux. These eddy currents are undesirable as they generate a magnetic flux that opposes the main field flux and also result in ohmic heating. Steel laminations help to decrease the formation of eddy currents by increasing the resistance of the material and restricting the flow of eddy currents, as shown in Fig. 1.2.

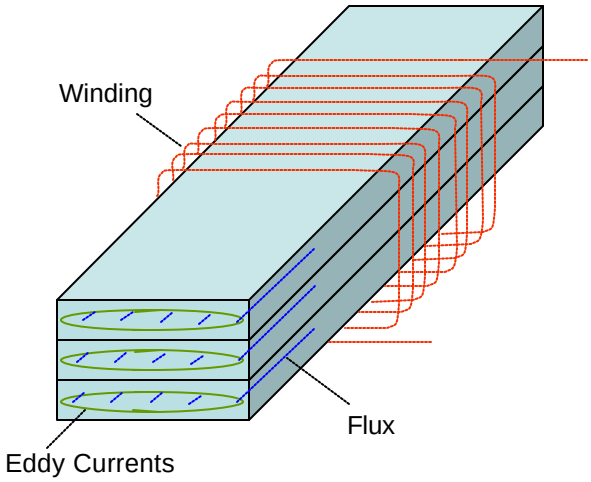

Figure 1.2. Eddy currents restricted by thin laminations [1.2].

The laminations are typically fabricated by a punching process in which a die is used to stamp patterns out of thin sheets of material. The thin sheets are stacked to form the desired magnetic core geometry. This production method has several disadvantages. First, the punching process generates mechanical strain in the laminations which alters the material properties and decreases the performance of the material. Consequently, the punching process must be followed by an annealing process, which adds to the production costs. Second, the punching process inherently results in waste material. The material cost associated with a modern electric motor fabricated via an automated process can be as high as 60% of the final product cost [1.3]; therefore, the amount of scrap material that results from the punching process is substantial.

In recent years the performance of laminated cores has improved though the use of thinner gage sheets and alloying components such as silicon. However, there is limited opportunity for further improvements that do not also result in increased production costs or degraded mechanical properties and therefore reduced reliability. To keep up with the

growing demand for energy efficient, lower cost products, different manufacturing methods are currently being investigated.

1.2 Modular, Integrated Motor/Controller Concept

The overall goal of this research is the development of a modular permanent magnet machine that is constructed of identical, individual stator poles that are each closely integrated with their own power electronics module - a concept referred to as the modular, integrated motor/controller. The specific objective of this thesis is the development of a thermal management analysis for the integrated motor/controller system.

1.2.1 Modular Pole Design

The stator assembly for the modular motor is constructed by combining twelve identical modular pole pieces (for a 6-pole machine) in an alternating pattern in order to create an annular ring with a 90° electrical angular displacement between the two phases. By shaping each pole face in a sinusoidal profile as seen in Fig. 1.3, a net magnetic flux density is created in which the flux varies sinusoidally with angular position along the air gap. This pole configuration makes it possible to obtain a smoothly-rotating sinusoidal flux wave, which is the ideal shape for a flux wave as it produces no torque ripple in the motor, despite the use of concentrated windings [1.4].

(a) (b)

Figure 1.3. Modular concept showing: (a) individual segmented stator pole piece and (b) stator section showing two poles at 90° angular displacement.

The axially-profiled geometries illustrated in Fig. 1.3 would be very difficult to fabricate using a conventional, laminated magnetic core due to the geometrical limitations imposed by the use of laminations, which are essentially two-dimensional. To overcome this obstacle, the stator poles will be manufactured via a casting process using a soft metal composite (SMC) material, such as Somaloy 500™. Somaloy 500™ is manufactured by the Swedish company Höganäs AB [1.5]. The casting process associated with SMC part molding makes it possible to create complex, three-dimensional geometries; the only limitation is that the width-to-length ratio of a geometry should not exceed approximately 3:1 in the pressing direction. Larger aspect ratios result in regions of locally reduced material density which degrades the mechanical and electrical integrity of the component and also complicates the ejection of the component from the die [1.3].

The use of the SMC material has other potential advantages. The molecular structure of the SMC introduces a third dimension of magnetic flux in the material. The increase in flux obtained by using the SMC versus the typical iron laminations makes it possible to

design a smaller, more compact motor with the same output characteristics. The casting process is nearly scrapless and will therefore decrease material costs relative to a laminated core. Compacted powder products can be produced with a high tolerance and therefore require little, if any, final machining and no final annealing process is necessary. Also, the interchangeability of the stator pieces will facilitate part repair and replacement within the motor.

Another advantage of using a soft metal composite is that the material exhibits an almost linear dependence of core loss with magnetizing frequency as opposed to the almost squared dependence of core loss with frequency typical of most lamination steel grades [1.6]. Therefore, with any increase in magnetizing frequency, the core losses in a laminated motor will be much higher than in an equivalent motor constructed from a SMC.

1.2.2 Integrated Power Electronics Module

In addition to the innovative physical design of the stator described above, this project seeks to closely couple an Integrated Power Electronic Module (IPEM) with each modular stator pole. The IPEM is responsible for the switching process required by the pulse-width modulation (PWM) that activates the stator. A typical IPEM consists of one or more power semiconductor modules mounted on a heat sink. The top surface of the IPEM consists of electrical interconnections with a silicon wafer and the bottom surface is dedicated to thermal management.

The integration of the power electronics technology within the motor housing will eliminate the long cable interconnections that currently run between the electrical converter and motor. These cables result in electromagnetic interference (EMI) caused by the high

frequency PWM switching process. The cables are also a major contribution to the drive failure rate. Finally, the tight physical integration of the motor and the control electronics opens new opportunities for creative motor sensor schemes that will improve drive performance and protection capabilities.

However, the concept of directly integrating the IPEM with the stator is challenged by the thermal limitations of the IPEM; the maximum safe temperature for the electronic component is approximately 125°C whereas the motor is typically designed to operate reliably at much higher temperatures. Therefore, the goal of this research is to evaluate the thermal characteristics of the integrated motor/controller system in order to find an optimum configuration scheme.

1.3 Thesis Outline

Chapter 2 describes the motor models that were developed and verified. Chapter 3 describes the flow models of the cooling air through the interior passages of the poles and the motor channel. In Chapter 4, the ANSYS model of the IPEM is detailed. In Chapter 5, these component level finite element models are integrated in various ways in order to provide system-level information that allows for the evaluation and design of various cooling system options. The experimental verification of the modeling approach is covered in Chapter 6.

1.4 References

[1.1] Wingard Hydroblanking, Wingard & Co., Inc., 4205 Menio Drive, Baltimore, MD 21215, www.hydroblanking.com, info@hydroblanking.com, Phone 410-358-2210, Fax 410-358-4573.

[1.2] "Cold Rolled Motor Lamination Sheet," United States Steel Corporation, 600 Grant Street, Pittsburgh, PA 15219, http://www.ussteel.com.

[1.3] Dickinson, P.G., "Using Iron Powder to Enhance the Performance and Reduce the Environmental Cost of Motor Production," Power Electronics, Drives and Machines Post Graduate Conf., School of Electrical, Electronic & Computer Engineering, University of Newcastle upon Tyne, UK.

[1.4] White, R.J., Jahns, T.M., Lipo, T.A., "Torque Analysis and Cogging Torque Minimization in a Modular Permanent Magnet AC Machine with Concentrated Windings," Proc. 2003 CPES Seminar, April 2003.

[1.5] Höganäs AB, SE-263 83 Höganäs, Sweden, http://www.hoganas.com, info@hoganas.com, Phone: +46 (0)42 33 80 00, Fax: +46 (0)42 33 81 50.

[1.6] Krause, R.F., Bularzik, J.H., Kokal, H.R., "A Pressed Soft Magnetic Material for Motor Applications," Magnetics International, Inc., Burns Harbor, IN 46304.

2 Motor Pole Model

Electric motor design is typically accomplished via simple, thermal network models for system level modeling [2.1]. These thermal network models are effective for considering a relatively fixed design where some empirical data can be used to "tune" the model - that is make the predictions agree with experimental values over some range. Therefore, while this approach is effective for mature electric motor systems with simple components, it is not as useful for the design of the thermal management system for the integrated motor/controller system which is characterized by complex thermal paths due to the complicated geometry of the core back and tooth. Also, the air flow patterns through the motor case and stator passages play a critical role in the thermal behavior of the entire system. In addition, the internal details of the IPEM and the critical nature of its placement on each stator pole determine the junction temperature between the IPEM and motor, and therefore the viability of any thermal management system concept. The first objective of this research is therefore to develop thermal models of the key components of the motor/controller system. These models must be sufficiently detailed so as to be predictive yet sufficiently flexible to allow design studies in which different cooling configurations are considered.

To account for all of the geometric details and material properties of the machine prototype, the components of the motor system were modeled using a finite element software package. This chapter describes the motor models that were developed and verified. The commercial software package ANSYS® [2.2] was used to generate the heat transfer models of the motor pole unit cell (consisting of one-half of each of two adjacent

poles each with a winding, tooth, etc.) Where possible, these models have been verified through analytical solutions in the appropriate limit.

2.1 Model Geometry

This section describes the finite element model of the motor pole unit cell developed using the ANSYS software. The ANSYS code required to generate the model is found in Appendix A.

The geometric details of the motor poles are based on the detailed design drawings provided by R. White [2.3] (Appendix B). The machine, which is expected to produce up to 5 kW of shaft power, is constructed of twelve identical stator poles with concentrated windings, as shown in Fig. 2.1 (a). A machine stator assembly is formed by interconnecting twelve of these pole pieces to form an annular ring as shown in Fig. 2.1 (b).

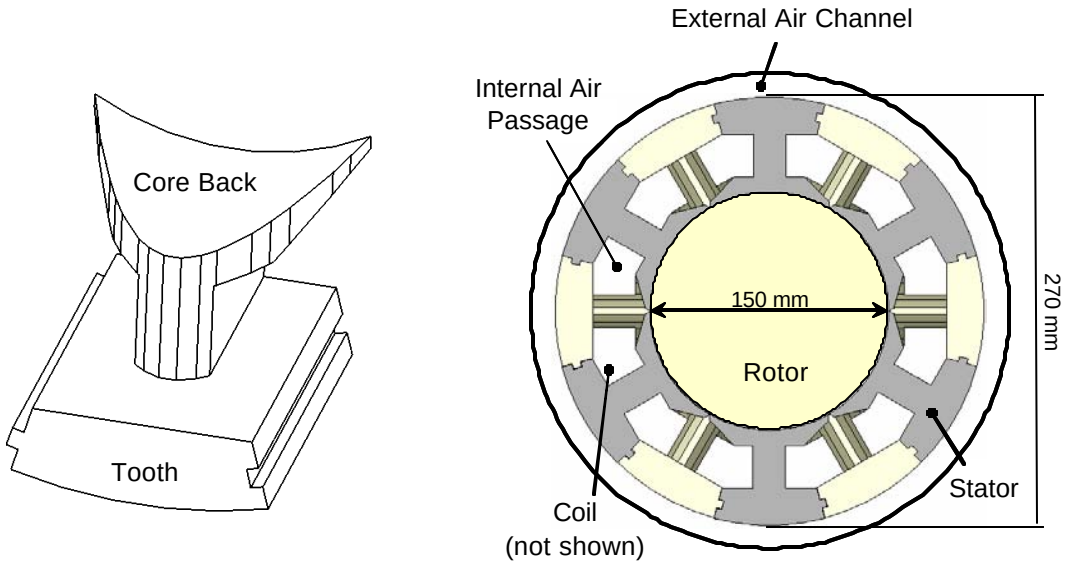

Figure 2.1. Segmented pole piece (a) and modular motor/controller assembly (b).

The thermal model of the machine takes advantage of the symmetry that is inherent in the modular design. A unit cell consisting of one-half of each of two adjacent stator poles is modeled, as shown in Fig. 2.2. Modeling the machine using half-symmetry reduces the complexity of the model and therefore the computational time required by the finite element software. The symmetry in the stator geometry is represented in the finite element model by adiabatic surfaces. To construct the complicated stator geometry using ANSYS, the stator pole piece is broken into four separate segments: the core back, the coil, the tooth, and the motor casing as seen in Fig. 2.3.

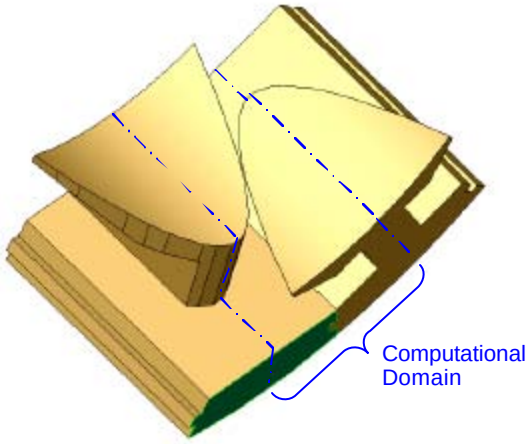

Figure 2.2. Computational domain for model.

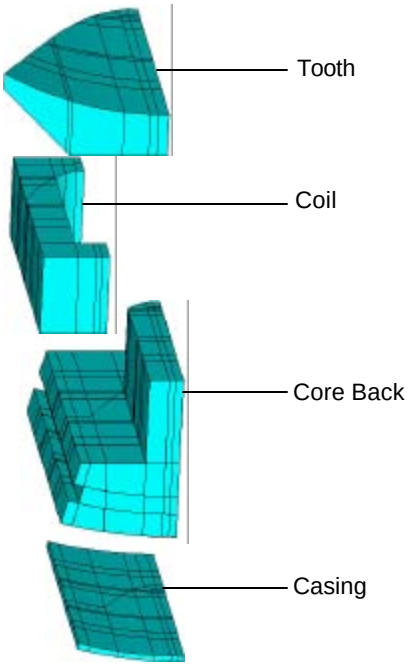

Figure 2.3. Segmented motor pole model pieces.

2.2 Material Properties

The design model is a steady-state, thermal model; therefore, the only material property that is required is thermal conductivity. This section describes how the thermal conductivity of each sub-component of the motor pole model is estimated.

2.2.1 Core Back and Tooth

The core back and tooth are constructed of a soft metal composite (SMC) composed of Somaloy 500™ with Kenolube 0.5% lubricant [2.4]. The material is designed to be cast into complex shapes suitable for advanced motor designs. SMC consists of very fine pure iron powder particles, each coated with an insulating oxide layer on the particle surface as seen in Fig. 2.4 (a). A phenolic resin binder can be added to the powder in order to increase the mechanical strength of the material. Together with a lubricant, the particles are then compacted at a high pressure. The thermal and mechanical properties of SMC differ substantially from lamination steel, as shown in Table 2.1.

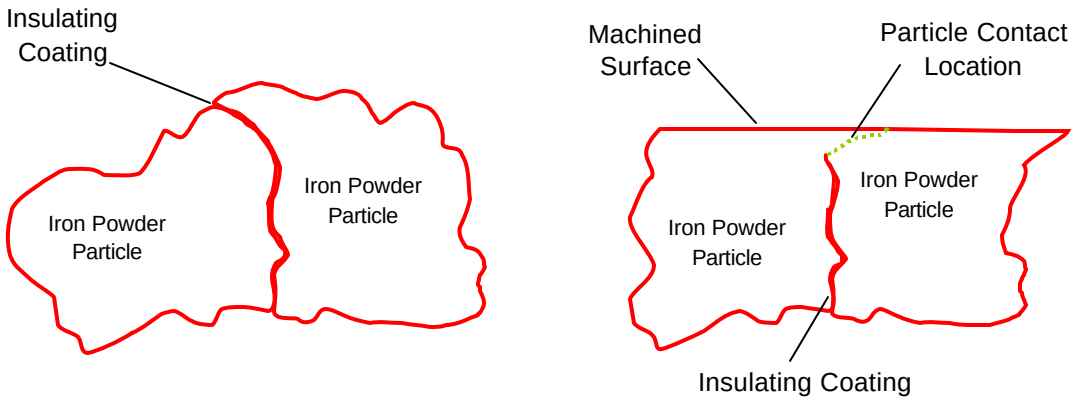

Figure 2.4. Soft metal composite composition [2.5] before (a) and after machining (b).

Table 2.1. Comparison of mechanical properties of SMC and lamination steel [2.6].

Property		**Somaloy 500**	**Lamination Steel (grade 315)**
Density	kg/m^3	7360	7650
Modulus of Elasticity	GPa	92	200
Tensile Strength	MPa	18	500
Thermal Conductivity	W/m-C	18	45 (in the plane of the laminations) 15 (axially, between laminations)

The molecular structure of the SMC presents the possibility that the surface of a machined part will have significantly different properties than the bulk material. When machined, the ductility of the iron causes the powder particles to shear along the plane of the cut, resulting in iron powder particles that are in direct contact with each other along the machined surface, rather than electrically and thermally isolated in a matrix as in the cast material as shown in Fig. 2.4 (b). This contact may alter the material properties along a machined surface. Until thermal testing can be completed and a stator designed and constructed from Somaloy 500™, the exact thermal properties of the SMC will not be known. Therefore, initial modeling results assume that the properties of the core back and tooth material are not changed by any machining operations. The material properties of powdered iron at 100°C are listed at the end of Section 2.2 in Table 2.3.

2.2.2 Motor Windings

The motor windings are typically made of copper wire due to its low resistivity and high ductility, which allows the conductors to be wound tightly together. The wire is coated with an electrically insulating polyimide film, chosen due to its high thermal rating of 220°C and low thermal resistance [2.7].

Due to computational limitations, the FE model of the motor does not simulate the details of all of the individual windings. Rather, an equivalent thermal conductivity is used

to represent the conductivity of the composite structure associated with the copper wire, its insulation, and the air that fills the wire-to-wire void. The effective conductivity of the wire, insulation, and interstitial air composite is estimated using a unit cell consisting of an equilateral triangle that intersects the center of three adjacent wire segments, as shown in Fig. 2.5. The total length of one side of the triangle is the sum of the air gap between two wires, t_{gap}, twice the insulation thickness, t_{ins}, and twice the wire radius, r_w.

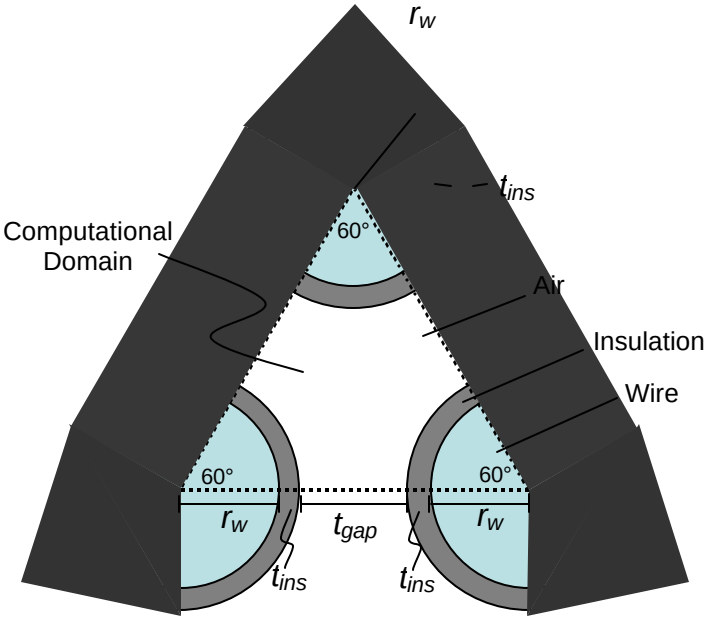

Figure 2.5. Computational domain for packing factor calculations.

The "tightness" of the wire winding is defined by its equivalent packing factor, F_{12}, which is the sum of the packing factor of copper, F_1, and the packing factor of insulation, F_2, calculated according to Eqs. 2-1 and 2-2:

$$f_1 = \frac{A_{copper}}{A_{total}} \tag{2-1}$$

$$f_2 = \frac{A_{insulation}}{A_{total}} \tag{2-2}$$

where A_{copper} and $A_{insulation}$ are the areas of copper and insulating material and A_{total} is the total area in the unit cell. In order to maintain a constant equivalent packing factor, as the wire diameter is increased, both the air gap and insulation thickness must increase proportionally.

The equivalent thermal conductivity of the wire in the transverse direction (i.e., across the packing or in the plane shown in Fig. 2.6 (a) is calculated assuming the conductivity of copper, polyimide, and air listed in Table 2.2 using the two-component material technique presented by H. Kanzaki et al. [2.8].

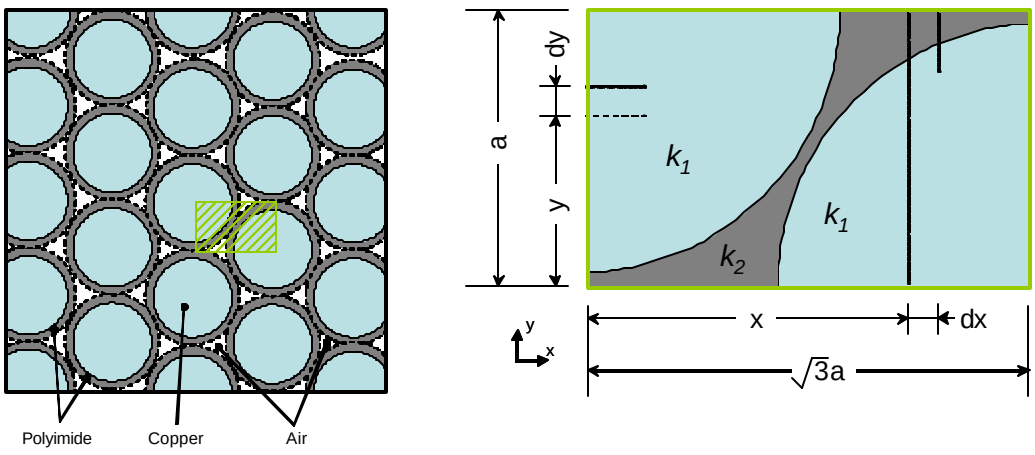

Figure 2.6. Closed-pack-type coil estimation model [2.8].

The two-component material technique requires the calculation of the equivalent conductivity, $k_2^{'}$, of the polyimide insulation and air. Equation 2-3 defines the equivalent conductivity between the two materials.

$$k_2^{'} = \frac{f_2 k_2 + f_3 k_3}{f_2 + f_3} \tag{2-3}$$

Here k_2 and k_3 represent the thermal conductivity of the polyimide insulation and air respectively.

The mean value of the equivalent thermal conductivity for closed-pack-type coils, $\bar{k}$, is calculated using Eq. 2-4:

$$\bar{k} = \frac{\left(\bar{k}_x + \bar{k}_y\right)}{2} \tag{2-4}$$

where $\bar{k}_x$ and $\bar{k}_y$ are the equivalent *x*- and *y*-directional thermal conductivities. Equations 2-5 and 2-6 are derived from the geometry of the hexagonal configuration shown in Fig. 2.6 (b) and are used to calculate the equivalent *x*- and *y*-directional thermal conductivities by integrating between 0<*x*<a and 0<*y*<a.

$$\bar{k}_x = 2\sqrt{3}\left\{\int_0^{1-F} \frac{k_1 k_2^{'}}{\left(k_2^{'} - k_1\right)\sqrt{F^2 - y^2} + \sqrt{3}\,k_1} dy + \int_{1-F}^{1/2} \frac{k_1 k_2^{'}}{\left(k_1 - k_2^{'}\right)\left(\sqrt{3} - \sqrt{F^2 - y^2} - \sqrt{F^2 - (y-1)^2}\right) + \sqrt{3}\,k_2^{'}} dy\right\} \tag{2-5}$$

$$\bar{k}_y = \frac{2}{\sqrt{3}}\left\{\int_0^{\sqrt{3}-F} \frac{k_1 k_2^{'}}{\left(k_2^{'} - k_1\right)\sqrt{F^2 - x^2} + k_1} dx + \int_{\sqrt{3}-F}^{\sqrt{3}/2} \frac{k_1 k_2^{'}}{\left(k_1 - k_2^{'}\right)\left(1 - \sqrt{F^2 - x^2} - \sqrt{F^2 - \left(x - \sqrt{3}\right)^2}\right) + k_2^{'}} dx\right\} \tag{2-6}$$

where k_1 is the thermal conductivity of copper and $F = \sqrt{2\sqrt{3}f_1/p}$. The EES code used for these calculations is found in Appendix C.

At a constant wire diameter and insulation thickness, the equivalent thermal conductivity increases with increasing equivalent packing factor as shown in Fig. 2.7. This is intuitively correct; as more of the space is filled with high conductivity copper, the effective thermal conductivity of the windings will increase.

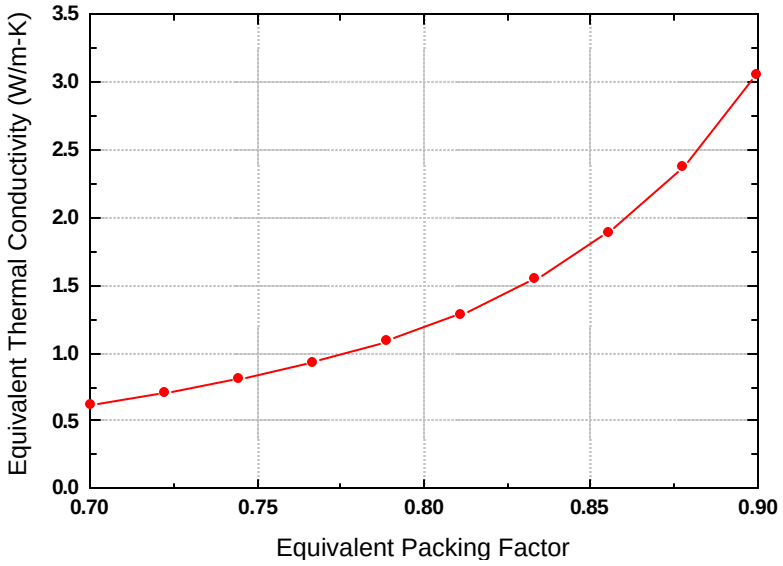

Figure 2.7. Effect of equivalent wire packing factor on equivalent thermal conductivity at d = 1.63 mm and T = 120 °C.

If the thickness of the insulation is maintained at a constant fraction of the wire diameter (1.85%) then the equivalent thermal conductivity of the winding is unaffected by wire diameter for any packing factor, as shown in Fig. 2.8. Even though the size of each unit cell increases as wire diameter increases, the unit cells remain self-similar and therefore the effective conductivity does not change for a given packing factor.

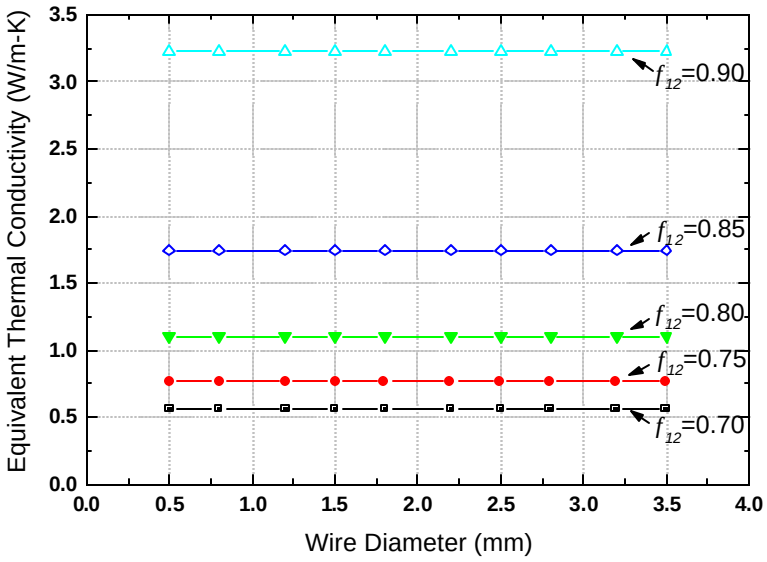

Figure 2.8. Effect of wire diameter on the equivalent thermal conductivity of the winding for different packing factors when a constant insulation thickness to wire diameter ratio (1.85%) is maintained.

In fact, the ratio of insulation thickness to wire diameter does not remain constant as the wire diameter increases. If the specifications associated with the National Electric Manufacturers Association (NEMA) minimum heavy build insulation thickness for film insulated round magnet wire [2.9] (see Appendix D) are used then a slightly different relationship between equivalent thermal conductivity and wire diameter is obtained, as shown in Fig. 2.9. Note that the effect of wire diameter on the equivalent thermal conductivity is still secondary to that of the packing factor. At low packing factors, the equivalent thermal conductivity follows a decreasing trend as wire diameter increases; at a high packing factor of 0.90 the equivalent thermal conductivity increases with increasing wire diameter.

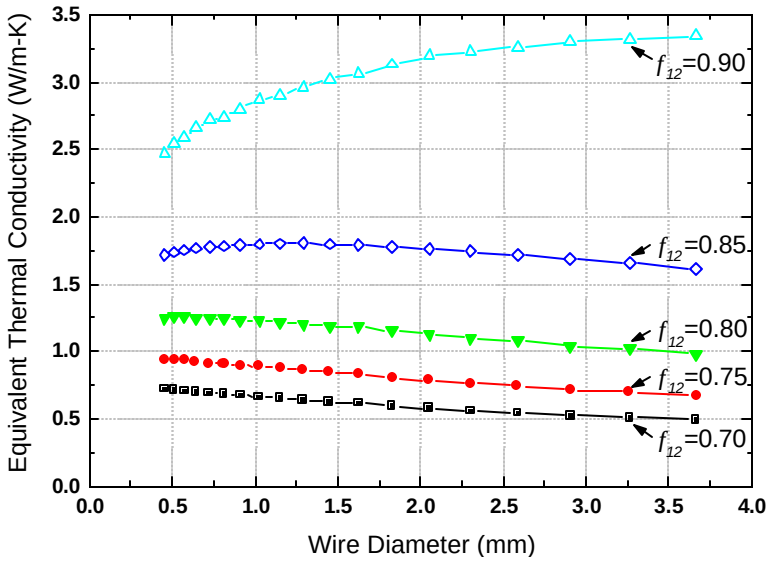

Figure 2.9. Effect of wire diameter on the equivalent thermal conductivity of the winding at different packing factors; the insulation thickness is specified for each wire diameter based on NEMA standards [2.9].

Initial modeling assumes a hexagonal closed-pack-type winding composed of American Wire Gauge (AWG) Size 14 Class 220 round copper magnet wire with a nominal diameter of 1.63 mm. The wire is insulated with a 41 μm polyimide coating based on the NEMA Magnet Wire Standard [2.9].

The equivalent packing factor that can be achieved by machine winding alone is nominally 0.64. This packing factor can be increased with applied pressure, reaching a maximum of 0.81 at approximately 400 MPa as shown in Fig. 2.10. Marks' Standard Handbook for Mechanical Engineers [2.10] states that the standard packing factor for an open-pack winding configuration is 0.785, and there is a theoretical gain of 7% for a closed-pack wire configuration. Since experiments have shown that this gain is neutralized due to tension in the winding, a conservative estimate for the equivalent packing factor of the wire configuration used in the model is assumed to be 0.75.

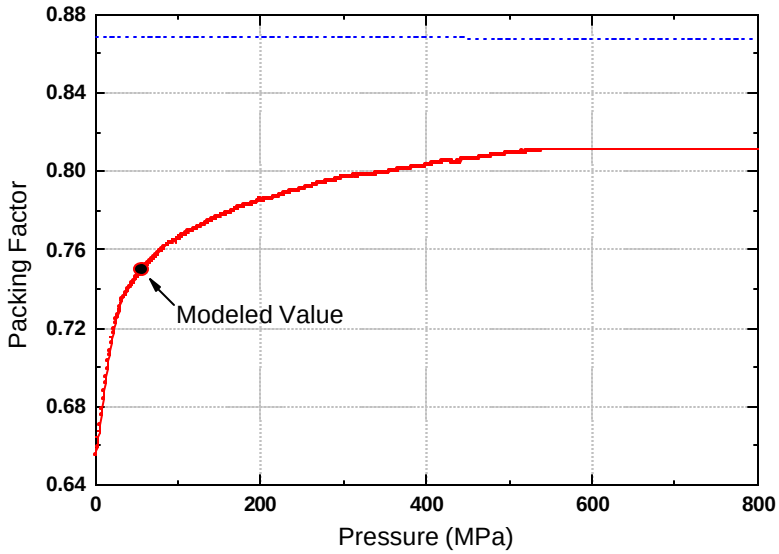

Figure 2.10. Packing factor variation with pressing pressure (dotted line is theoretical maximum) [2.10].

The temperature will affect the equivalent thermal conductivity of the winding by altering the material properties of each of the components. The equivalent conductivity of the winding is shown in Fig. 2.11 as a function of temperature.

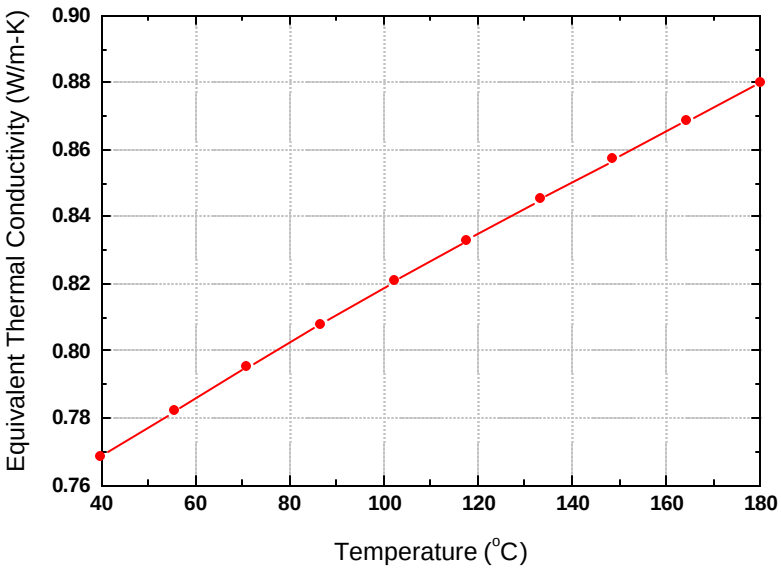

Figure 2.11. Effect of temperature change on equivalent thermal conductivity of winding components with $F_{12} = 0.75$, $d = 1.628$ mm, and $t_{ins} = 40.5$ µm.

The material properties listed in Table 2.2 are used in conjunction with Eqs. 2-3 through 2-6 in order to determine an equivalent conductivity of 0.84 W/m-K for the copper windings at a nominal temperature of 120°C; the effect of temperature is not accounted for in the FE model.

Table 2.2. Material properties of winding components at 120°C [2.11].

Material	Thermal Conductivity [W/m-K]	Packing Factor
Copper	393.5	0.68
Polyimide insulation	0.37	0.07
Air	0.03	0.25

2.2.3 Motor Casing

The motor casing is modeled as an aluminum shell, which is the industry standard because of its high strength and ductility and low mass. Over the anticipated 40°C to 180°C range of operating temperatures the thermal conductivity of aluminum changes by less than 2%; therefore a value of 238 W/m-K is used in the model. Table 2.3 summarizes the properties of the materials used in the stator model.

Table 2.3. Material properties used in stator model.

Component	Material	Density [kg/m^3]	Thermal Conductivity [W/m-K]	Specific Heat [J/kg-K]
Coreback/Tooth	Somaloy 500™	7360	17	447
Coil	Copper	8900	393.5	385
	Polyimide	1350	0.37	-
	Air	0.87	0.03	-
	Equivalent	6410	0.84	-
Casing	Aluminum	2705	238	900

2.3 Thermal Loads

The thermal loading on the motor-pole model is related to the losses associated with the motor. Exact values for these losses are not known because the efficiency of the motor cannot be determined without experimental testing. Therefore, the motor is modeled as having an efficiency of 84%; the motor converts 84% of the electrical energy input into mechanical energy and 16% of the input electrical energy is dissipated in various ways within the motor resulting in a temperature rise within the system. This value is a conservative estimate for an enclosed six pole machine based on the NEMA motor energy efficiency standard [2.12]. A more realistic value for the motor efficiency may be as high as 90% due to the increased efficiency of the motor/controller integration scheme, corresponding to the minimum full-load efficiency for NEMA Premium™ efficiency enclosed electric motors rated 600 volts or less [2.13]. However, the model is generated in a manner that provides a representative thermal loading in order to provide a reasonable design case. This low efficiency assumption provides a strenuous design target for the thermal management system.

2.3.1 Electrical Losses

Losses within the motor manifest themselves as a combination of the electrical dissipation in the conductors and hysteretic and eddy current losses within the core. The breakdown of these losses is an estimate based on discussions with the motor designers. The loss estimates can be adjusted parametrically in the model and serve to establish a base loading which allows various thermal designs to be compared.

The winding loss, referred to as the copper loss, is the heat generated due to the flow of current through the resistance of the windings. When an alternating current is applied to the winding, the resistance of the conductor tends to increase with frequency due to the decrease in effective area of the copper winding associated with the formation of eddy currents and resulting non-uniform distribution of current density in the conductor [2.14]. Based on the data provided by H. Yoshino et al. [2.15] (see Fig. 2.12), the total copper loss accounts for approximately 60% of the total loss of the motor. In the model, the copper loss is applied as a volumetric heat generation imposed uniformly over the winding volume and equal to approximately 60% of the total 16% motor losses (or 10% of the motor input power for a total loss of 500 W given a 5 kW input power).

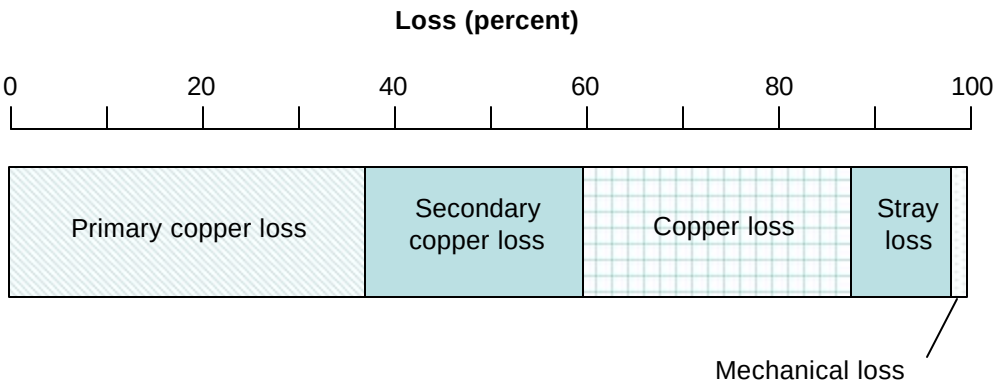

Figure 2.12. Components of energy loss in induction motors [2.15].

When an inductor core is exposed to any time-varying magnetic field, losses are induced within the core material. Core loss is the power dissipated in the initial magnetization of the material and the energy necessary to maintain the magnetization. Hysterestic losses are caused by the stressed regions that form due to the inability of domain walls to move within the composite. In an iron powder composite, hysteresis is reduced through the use of high purity iron particles and a heat treatment following the compaction

of the powder to improve the stressed regions. Eddy currents exist in a laminated core on two separate scales: one related to the eddy currents flowing through the entire cross section of the material and the other related to the eddy currents flowing through individual powder particles [2.14]. The unique magnetic properties of the SMC significantly decrease the eddy current losses that typically result in the lamination layers [2.14]. The losses due to hysteresis and eddy current formation together make up the total core loss.

Based on Fig. 2.12, the core loss in an induction motor is approximately 26% of the total losses. Therefore, in the simulation, the total iron loss is modeled as a uniformly applied volumetric heat load that is equal to 2% and 4% of the motor input power for the tooth and the core-back, respectively (or total loads of 100 W and 200 W for a 5 kW input power). Figure 2.13 summarizes these losses.

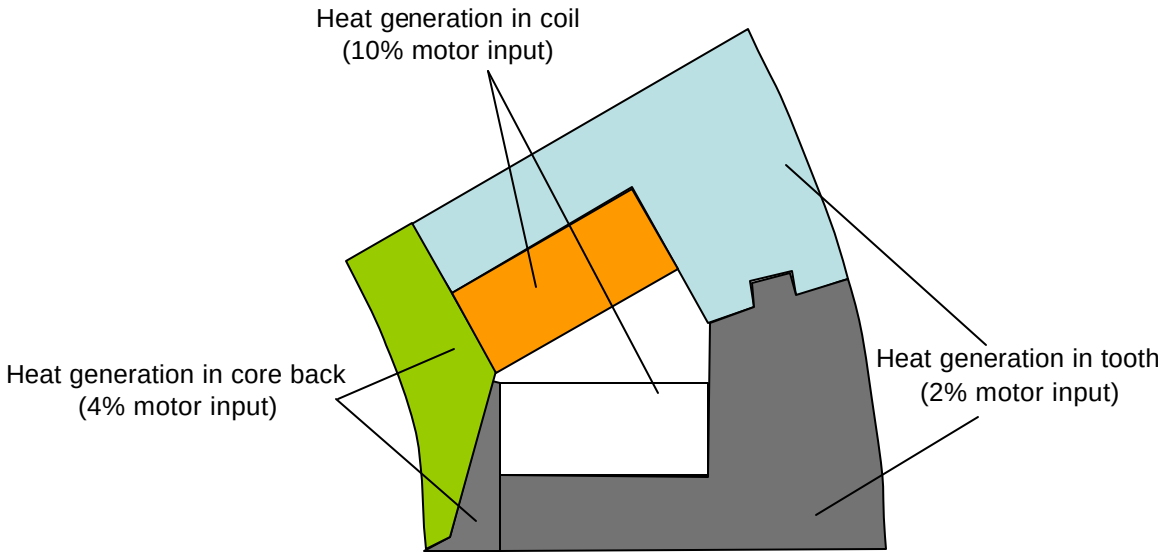

Figure 2.13. Heat generation in motor.

2.3.2 Mechanical Losses

Heat is also generated within the motor due to mechanical friction. The frictional losses at the motor bearings and at the interface between the carbon brushes are assumed to be relatively small compared with the losses mentioned above and also have substantially less impact on the critical temperatures in the motor or IPEM. Therefore, these losses are ignored in the finite element model.

2.4 References

[2.1] White, R.J., Jahns, T.M., Lipo, T.A., "Torque Analysis and Cogging Torque Minimization in a Modular Permanent Magnet AC Machine with Concentrated Windings," Proc. 2003 CPES Seminar, April 2003.

[2.2] ANSYS, ANSYS, Inc., Southpointe, 275 Technology Drive, Canonsburg, PA 15317, http://www.ansys.com, ansysinfo@ansys.com, Phone: (724) 514-3304, Fax: (724) 514-9494.

[2.3] White, R., Wisconsin Electric Machines and Power Electronics Consortium (WEMPEC).

[2.4] Höganäs AB, SE-263 83 Höganäs, Sweden, http://www.hoganas.com, info@hoganas.com, Phone: +46 (0)42 33 80 00, Fax: +46 (0)42 33 81 50.

[2.5] Persson, M., Jansson, P., "Soft Magnetic Composite Materials – Use for Electrical Machines," Electrical Machines and Drives IEE Conference Publication No. 412, September 1995.

[2.6] Dickinson, P.G., "Using Iron Powder to Enhance the Performance and Reduce the Environmental Cost of Motor Production," Power Electronics, Drives and Machines Post Graduate Conf., School of Electrical, Electronic & Computer Engineering, University of Newcastle upon Tyne, UK.

[2.7] Handbook of Polymer Coatings for Electronics – Chemistry, Technology and Applications (2nd Edition), William Andrew Publishing, Norwich, NY, 1990.

[2.8] Kanzaki, H., Sato, K., Kumagai, M., "A Study of an Estimation Method for Predicting the Equivalent Thermal Conductivity of an Electric Coil;" Heat Transfer-Japanese Research, Vol. 21, No. 5, Sep. 1998, pp. 429-433.

[2.9] National Electrical Manufacturers Association Dimensions for Bare and Film Insulated Round Magnet Wire, MW 1000-2003 Part 1, Washington D.C., 2003.

[2.10] Marks' Handbook for Mechanical Engineers, Tenth Edition, ed. Avallone, E., Baumeister, T., McGraw-Hill, Columbus, OH, 1996.

[2.11] Engineering Equation Solver (EES), F-Chart Software, Box 44042, Madison, WI 53744, http://www.fchart.com, info@fchart.com, Phone: (608) 255-0842, Fax: (608) 255-0841.

[2.12] Energy-Efficient Motor Systems Assessment Guide, Office of Energy Efficiency Industrial, Commercial and Institutional Programs, Ottawa, ON, 2001.

[2.13] National Electrical Manufacturers Association, General Specification for Consultants, Industrial and Municipal: NEMA Premium™ Efficiency Electric Motors (600 Volts or Less), Rosslyn, VA, 2003.

[2.14] Skarrie, H. "Design of Powder Core Inductors," Licentiate Thesis, Department of Industrial Electrical Engineering and Automation, Lund University, Sweden, 2001, ISBN 91-88934-19-5.

[2.15] Yoshino, H., Kurata, Y., "Energy-Saving Induction Motors," Mitsubishi Electric ADVANCE, June 2000, pp. 14-16.

3 Air Flow Models

This section describes the finite element model of the air flow through the complex motor passages as well as the analytical models that are used to determine the pressure drop and heat transfer coefficients within the simpler air passages that exist within the motor (Fig. 3.1). The finite element model is used to simulate the air flow through the interior passage formed between two adjacent stator poles. The geometry and grid generation software package CFD-GEOM [3.1] was used to create the intricate geometry and the computational fluid dynamics (CFD) package FLUENT [3.2] was subsequently used to determine the air flow patterns, pressure drop, and heat transfer characteristics. The analytical models use correlations for turbulent flow in order to describe the air flow through the channel that exists between the outside surface of the casing and the motor housing.

The purpose of these models is to determine the thermal-fluid performance of the air passages in a manner that allows integration with the previously described ANSYS motor model. This approach was chosen, as opposed to using ANSYS, to simultaneously predict the flow in the passages and the temperature distribution throughout the motor. The airflow model results are correlated as a function of the inlet air flow velocity, which may be obtained from a resistance analysis of a particular fan/flow passage system. The velocity is determined by matching the hydraulic characteristics of the channel (or in some cases, a set of channels) with the performance curve for a specific fan, as described in Chapter 5. The heat transfer coefficients on the various surfaces where the air interacts with the motor are also determined as a function of air flow velocity.

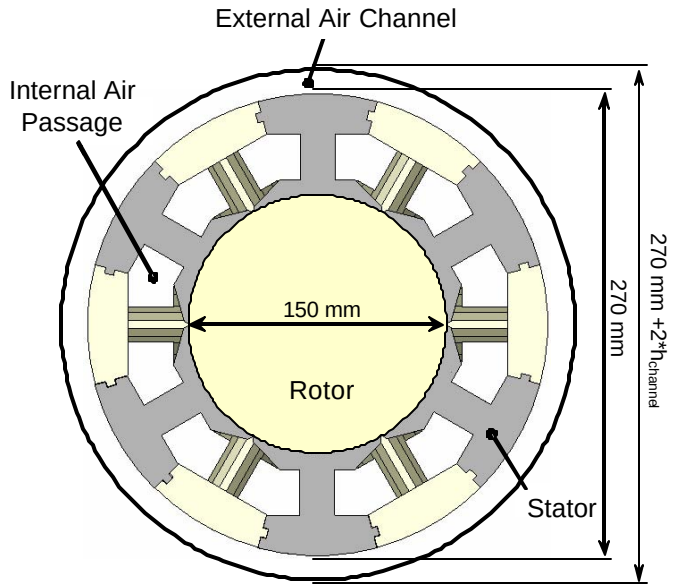

Figure 3.1. Internal and external airflow passages in the motor.

3.1 Interior Passage Model

3.1.1 Geometry

To replicate the intricacies of the geometry of the interior passages of the motor poles, a 3-D CFD geometrical mesh was created, as shown in Fig. 3.2. The model simulates the wall geometries and volume of a single air passage formed between two adjacent poles. The fluid is air, with the material properties found in Table 3.1. The solid surfaces where the air comes into contact with the SMC or the coil material are modeled using a no-slip wall boundary condition.

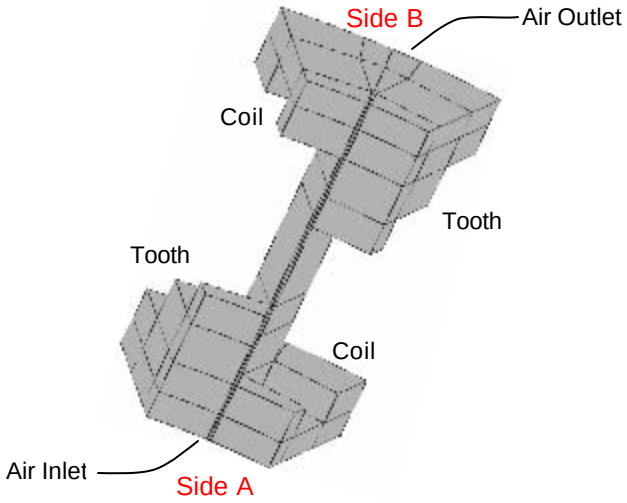

Figure 3.2. 3-D model of an internal air passage.

Table 3.1. Air properties for flow models.

Property	Value
Density	1.225 kg/m^3
Specific Heat	1006.43 J/kg-K
Conductivity	0.0242 W/m-K
Viscosity	1.79e^{-5} kg/m-s

Three different boundary conditions are applied to the 3-D model. The solid wall surfaces on which the fluid comes into contact with the tooth and coil are modeled with a constant wall temperature of 100°C. The air inlet side of the model (Side A) is modeled as a constant velocity inlet with a 27°C inlet temperature. Side B, the air outlet surface, has an outlet pressure boundary, with a back-flow total temperature of 27°C (i.e., any air returning to the model from this surface due to recirculation is assigned a temperature of 27°C) and a uniform pressure equal to ambient conditions.

Once complete, the geometrical mesh is exported to FLUENT, where a turbulent k-epsilon model solver is used to predict the flow and temperature distribution in the passage. The k-epsilon model, which is a semi-empirical model based on model transport equations

for the turbulence kinetic energy (k) and its dissipation rate (e), assumes that the flow is fully turbulent and the effects of molecular viscosity are negligible [3.2]. The velocity and temperature distributions predicted by the CFD package are subsequently used to determine the average heat transfer coefficient over each of the surfaces associated with the core and winding, and the pressure drop through the channel, all as a function of the inlet air velocity (or volumetric flow rate).

3.1.2 Results

Figure 3.3 shows the behavior of the air velocity as it moves through the passage for an average inlet velocity of 4 m/s. As would be expected, the highest velocities occur where the flow becomes constricted in the center of the passage. The figure also shows the wake regions that form on the upper side of the geometry. The air is nearly stagnant in these locations and it is expected that the heat transfer coefficients here are low as well.

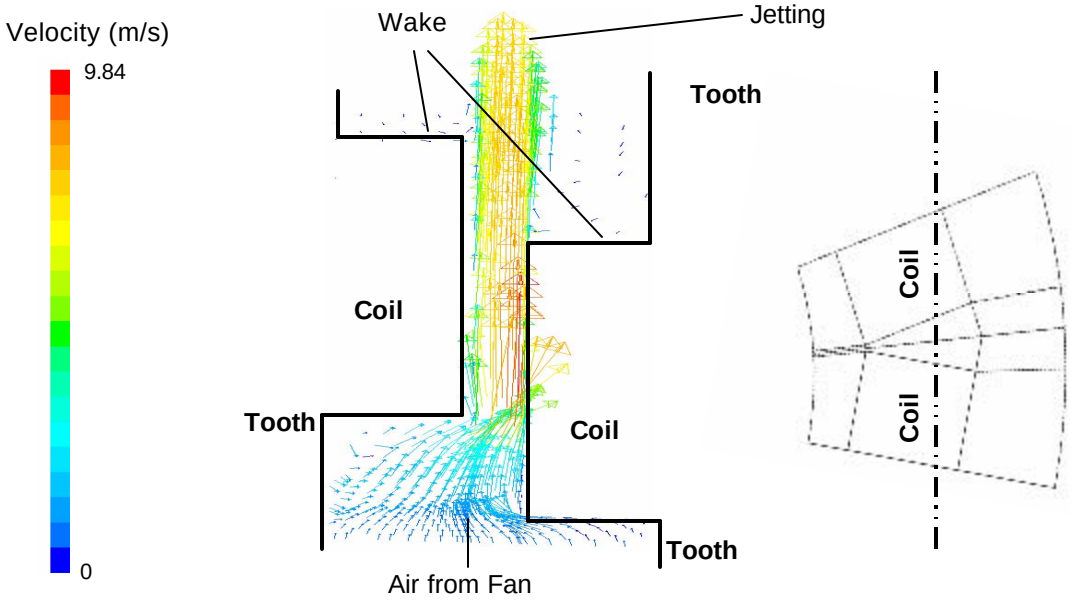

Figure 3.3. Behavior of air velocity through inner passage.

The heat transfer coefficients for the surfaces associated with the air inlet side coil (i.e., Side 1, the coil that is closest to the fan in Fig. 3.3) are illustrated in Fig. 3.4. The largest heat transfer coefficients occur on Surface 1, which is the surface that experiences the highest velocity. Surfaces 3 and 6 are both in the wake region and therefore see the lowest heat transfer coefficients.

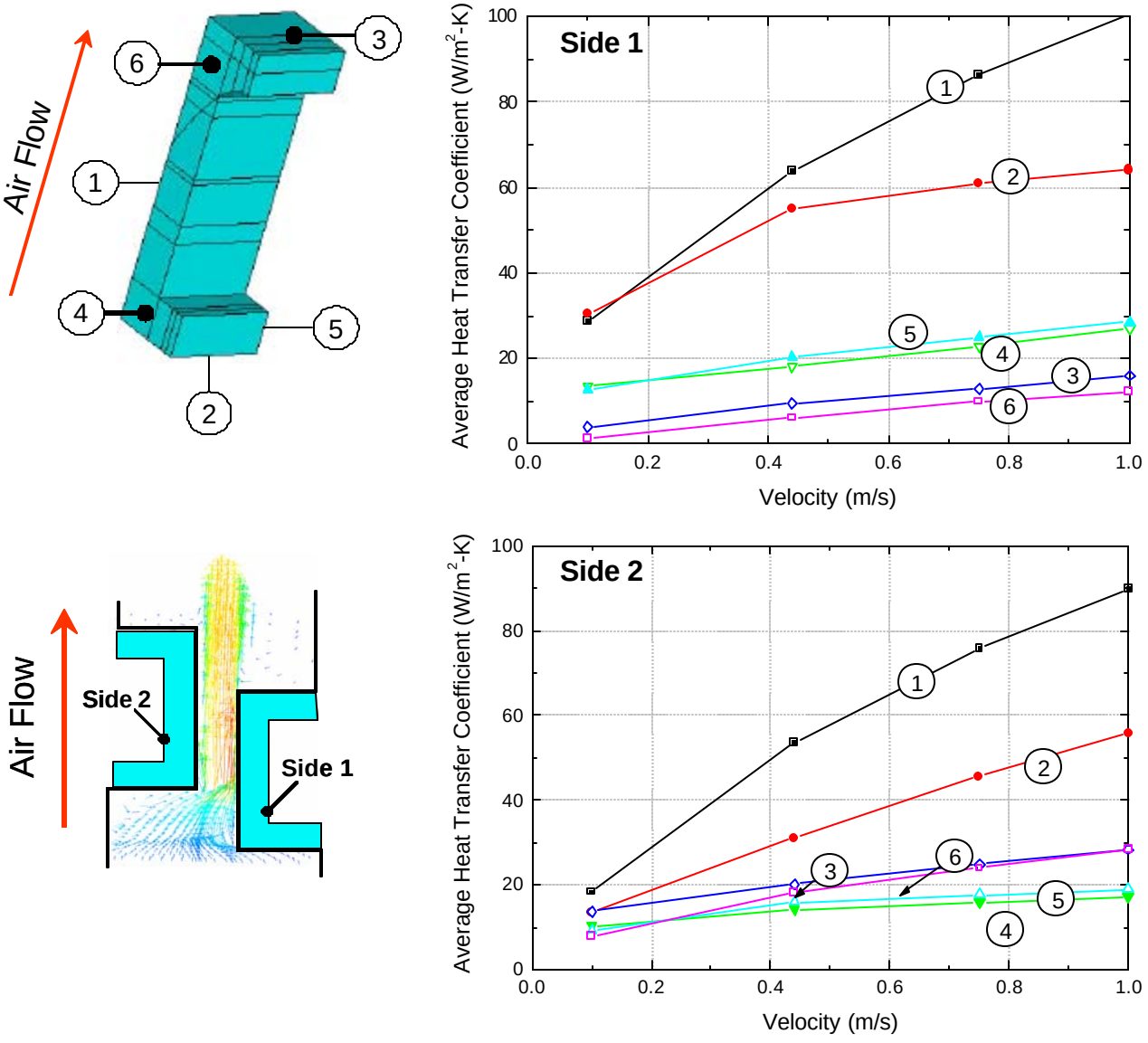

Figure 3.4. Coil surface heat transfer coefficients.

The average heat transfer coefficients on the air inlet side core back are shown in Fig. 3.4. Here, Surface 3 on the underside of the core back experiences the greatest heat transfer coefficients since it is located adjacent to the areas of high velocity in the passage. Surface 1 is a good example of the differences that some surfaces experience if they are located near the inlet or not (i.e., on Side 1 or 2). On Side 1, Surface 1 is directly perpendicular to the incoming air flow. Surface 1 on Side 2, however, is faced away from the direction of air flow, and thus experiences much lower heat transfer coefficients.

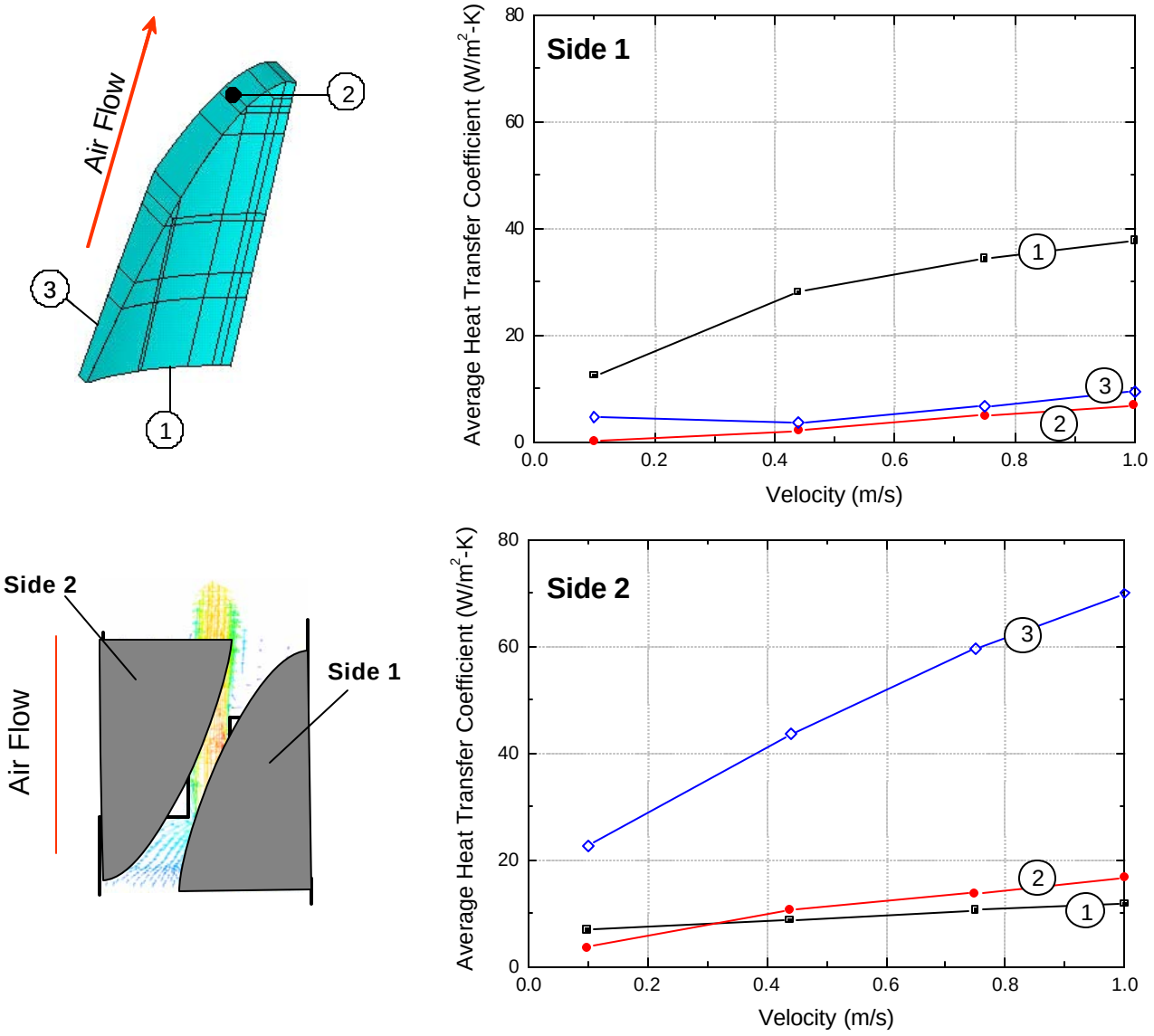

Figure 3.4. Core back heat transfer coefficients.

Figure 3.5 shows the average heat transfer coefficient over the surfaces on the tooth. The highest heat transfer coefficients are along Surface 4, where the velocities are greatest. Since the velocity is greater along the right edge in the center of the passage, the heat transfer coefficients along Surface 4 are slightly greater on Side 1 than Side 2.

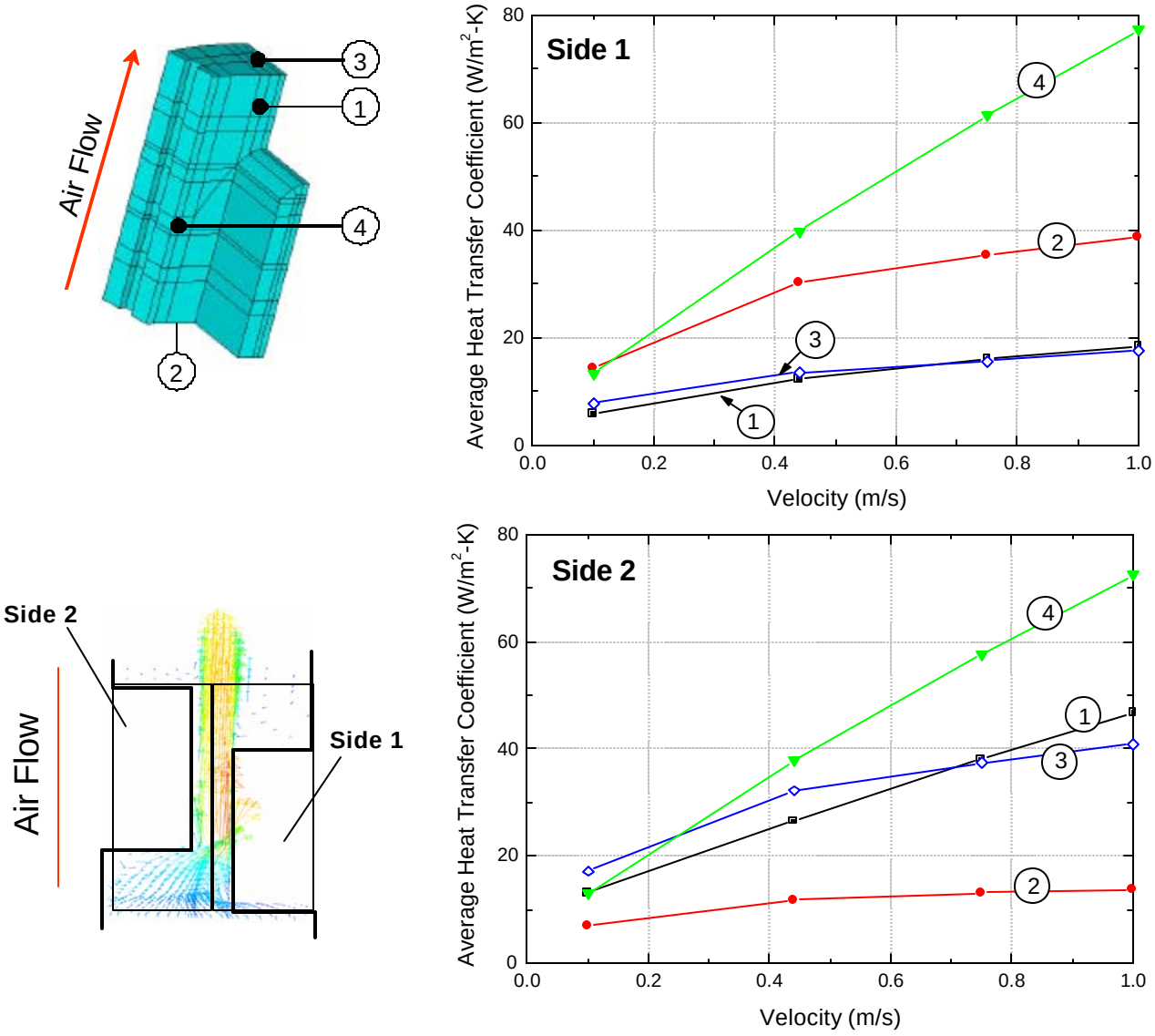

Figure 3.5. Tooth heat transfer coefficients.

Table 3.2 summarizes the average heat transfer coefficients on the various surfaces at one value of the velocity.

Table 3.2. Average heat transfer coefficients (W/m^2-K) at v = 0.44 m/s.

	Position	Coil	Core Back	Tooth
Side 1 (near inlet)	1	63.9	8.7	12.2
	2	55.1	10.5	30.1
	3	9.6	43.6	13.5
	4	18.0	-	39.8
	5	20.4	-	-
	6	6.1	-	-
Side 2 (near outlet)	1	53.7	28.0	26.6
	2	31.1	2.1	11.9
	3	20.2	3.5	32.2
	4	14.0	-	37.9
	5	15.9	-	-
	6	18.2	-	-

3.1.3 Verification

Results from the FLUENT model are verified numerically by evaluating the sensitivity of the results to the grid resolution and also through the analytical calculations that are described in the following sections.

3.1.3.1 Grid Insensitivity

The inner passage model was run using three different grids, all with the same geometry but a different number of cells: Course – 18,128 cells, Medium – 28,936 cells, and Fine – 48,364 cells. Figures 3.6 and 3.7 show the effect of the number of cells on the heat transfer coefficient on the surfaces of the tooth and coil. Since there is little change between the average heat transfer coefficient values in the Medium and Fine grids, the Fine grid is assumed to provide an accurate representation of the average heat transfer values on the walls of the motor.

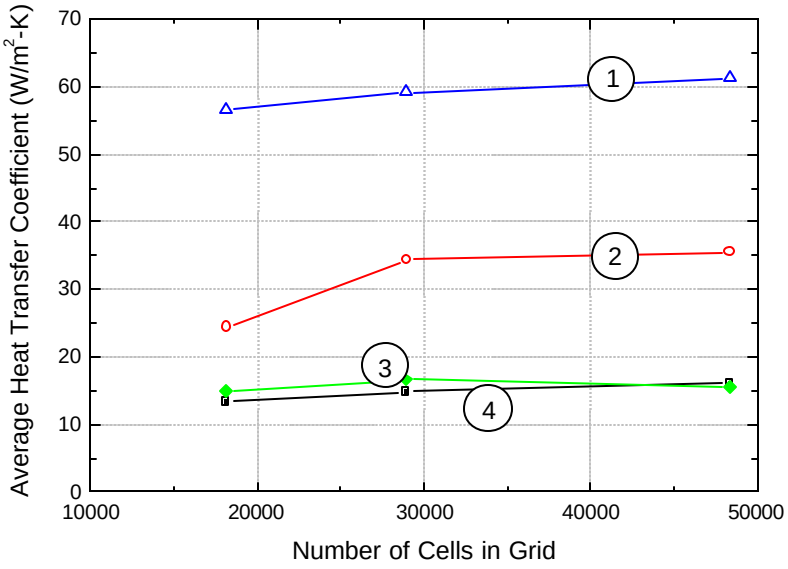

Figure 3.6. Effect of number of cells on average heat transfer coefficient for air inlet side surfaces of motor tooth at v = 0.75 m/s.

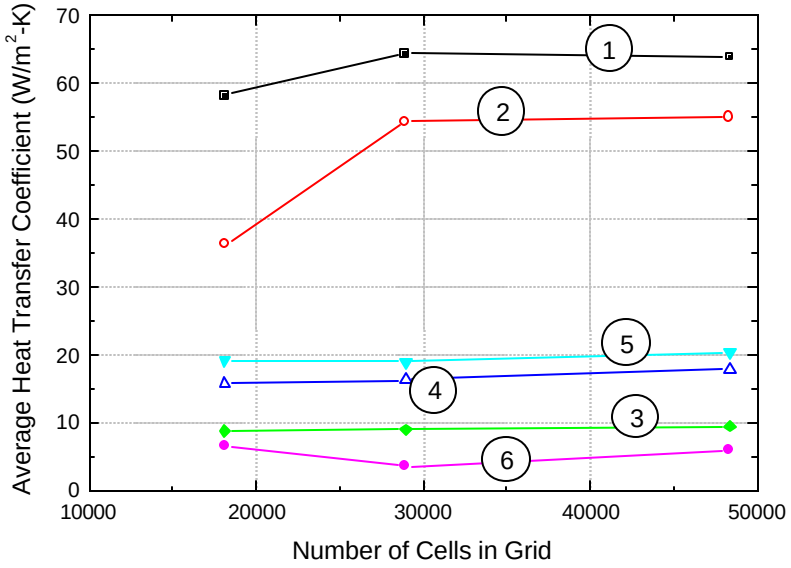

Figure 3.7. Effect of number of cells on average heat transfer coefficient for air inlet side surfaces of motor coil at v = 0.44 m/s.

3.1.3.2 Analytical Solution

The inner passage average heat transfer coefficients can be evaluated approximately using the hydraulic diameter of the section of the passage that is under analysis. The

following is an example calculation for the narrowest section of the passage. Figure 3.8 shows the location and geometry of the area of interest.

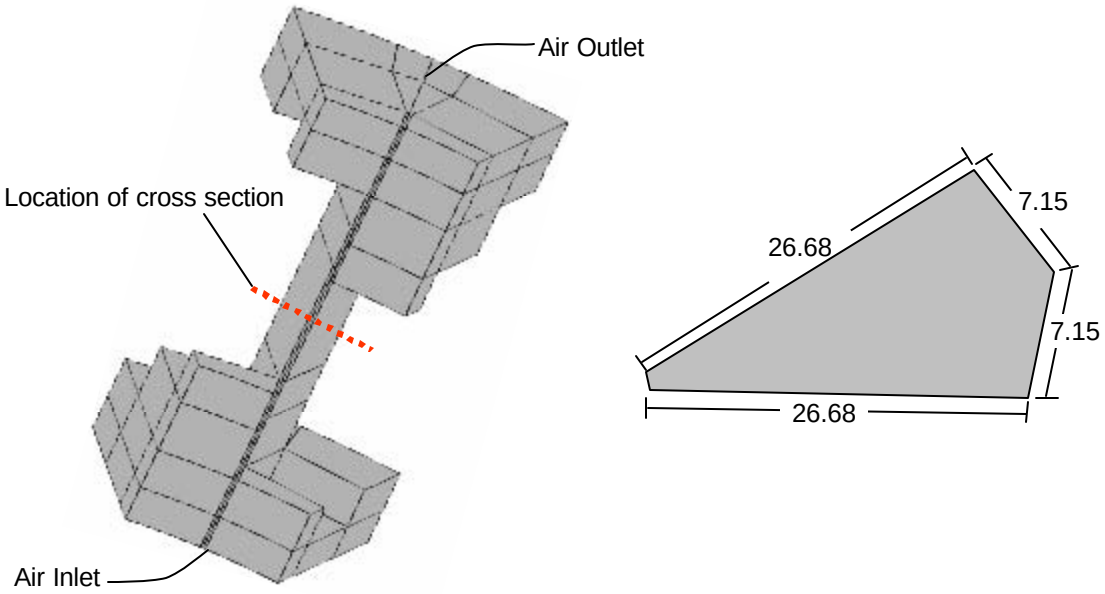

Figure 3.8. Location and dimensions of cross-sectional area at midpoint of inner passage.

A hydraulic diameter (D_h) of 11.28 mm is calculated according to:

$$D_h = \frac{4A_c}{P_w} \tag{3-1}$$

where A_c is the cross-sectional area and P_w is the wetted perimeter of the section. Assuming turbulent fully-developed flow within this section of the passage, Eqs. 3-2 and 3-3 [3.3] are used to calculate the average heat transfer coefficient, $\overline{h}$.

$$Nu = 0.023 \mathrm{Re}^{\frac{4}{5}} \mathrm{Pr}^{n} \tag{3-2}$$

$$Nu = \frac{\overline{h} D_h}{k} \tag{3-3}$$

where Re is the Reynolds number of the passage, Pr is the Prandtl number, n is a dimensionless exponent equal to 0.4 (the air is being heated), and k is the thermal conductivity of the air. For a representative inlet velocity of 8 m/s, the Reynolds number is calculated to be 6120 in the passage. These calculations result in an average heat transfer coefficient of 62.8 W/m^2-K along Surface 1 of the coil, corresponding to a 2.2 percent error relative to the FLUENT results predicted for Surface 1.

3.2 Channel Model

The air flow through the channel between the motor housing and the outside surface of the casing is calculated analytically assuming the channel geometry shown in Fig. 3.9. As with the air passage model, the properties for the air within the channel are found in Table 3.1. Air enters the channel with a uniform velocity and an inlet temperature of 40°C. A temperature boundary condition of 127°C is applied to the wall surfaces of the pole outer surface.

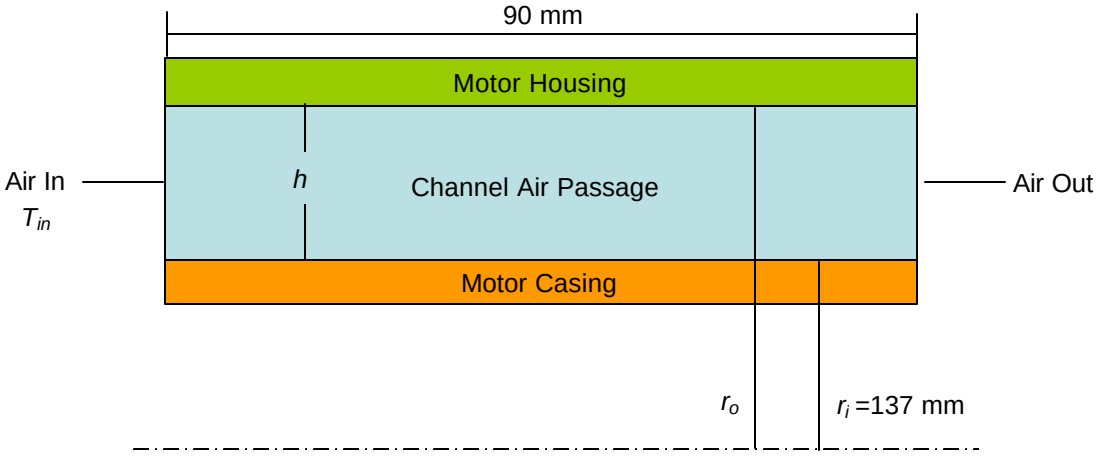

Figure 3.9. Channel passage geometry.

The channel may be analyzed either as a tube or flat plate; the choice is based on the boundary layer thickness, *d*, which is calculated according to [3.3]:

$$d = 0.37 x \mathrm{Re}_x^{\frac{-1}{5}} \tag{3-4}$$

where x is the distance into the channel and Re_x is the local Reynolds number. Based on Eq. 3-4, if the channel inlet velocity is greater than 0.07 m/s then the boundary layer thickness is less than the channel height of 10mm. Therefore, the air flow can be adequately analyzed as flow over a flat plate.

Turbulent flow occurs across a flat plate when the Reynolds number is greater than approximately 1×10^5. Using 90 mm as the plate length, the inlet velocity must be greater than 16 m/s for turbulent flow to develop within the channel. The local heat transfer coefficient, Nu_x, within the channel is then calculated using Eq. 3-5 [3.3]:

$$Nu_x = 0.0296 \mathrm{Re}_x^{\frac{4}{5}} \mathrm{Pr}^{\frac{1}{3}} \tag{3-5}$$

where the local Reynolds number, Re_x, and the Prandlt number, Pr, are calculated using the air properties found in Table 3.1. Figure 3.10 shows the local heat transfer values as a function of position, x, into the channel for various air flow inlet velocities.

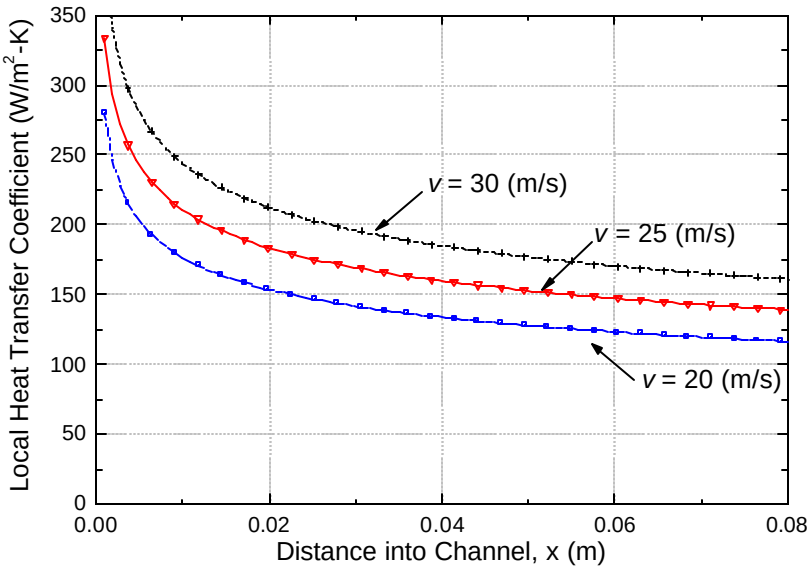

Figure 3.10. Local heat transfer coefficient in channel at various inlet velocities.

The pressure drop within the channel is calculated using the force balance shown in Fig. 3.11:

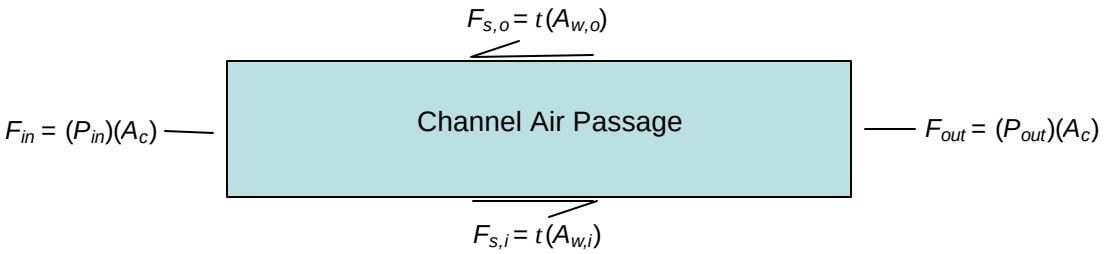

Figure 3.11. Force balance on channel.

where the forces at the inlet and outlet, F_{in} and F_{out}, are equal to the product of the pressure, P_{in} and P_{out}, and the channel cross-sectional area, A_c. The shear forces, $F_{s,o}$ and $F_{s,i}$, are equal to the product of the shear stress, t, and the wetted area, $A_{w,o}$ and $A_{w,i}$. Rearranging the terms in the force balance yields an expression for the pressure drop in the channel:

$$\Delta P = t \frac{A_{w,o} + A_{w,i}}{A_c} \tag{3-6}$$

where Eq. 3-7 defines the shear stress using a coefficient of friction (C_f).

$$t = \frac{C_f \, r \, v^2}{2} \tag{3-7}$$

where ? is the density of air, v is the air inlet velocity, and the coefficient of friction for turbulent flow can be computed according to [3.3]:

$$C_f = 0.0592 \, \mathrm{Re}_x^{\frac{-1}{5}} \tag{3-8}$$

The pressure drop in the channel is shown as a function of volumetric flow rate in Fig. 3.12.

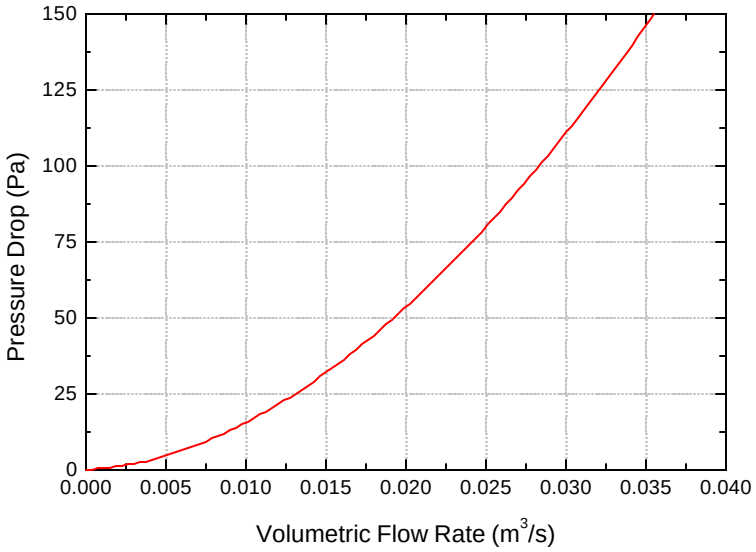

Figure 3.12. Pressure drop in channel.

3.3 References

[3.1] CFD-GEOM, CFD Research Corporation, 215 Wynn Drive, Huntsville, AL 35805, www.cfdrc.com, Phone: (256) 726-4800, Fax: (256) 726-4806.

[3.2] FLUENT, Fluent USA, 10 Cavendish Court, Centerra Park, Lebanon, NH 03766, www.fluent.com, Phone: (603) 643-2600, Fax: (603) 643-3967.

[3.3] Incropera, F., Dewitt, D., Introduction to Heat Transfer – Fourth Edition, John Wiley and Sons, NY, 2002.

4 IPEM Model

This section describes the finite element model of the IPEM which was developed using the ANSYS software. The ANSYS code required to generate the model can be found in Appendix E.

4.1 Model Geometry

The IPEM internal model, which consists of a chip mounted on a direct-bond copper (DBC) layer and base plate as shown in Fig. 4.1, remains the same regardless of the cooling configuration. The model dimensions are based on the detailed dimensions reported by Martens [4.1] and summarized in Table 4.1.

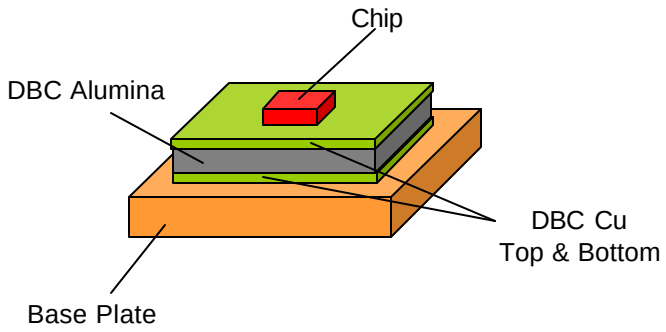

Figure. 4.1. IPEM geometry with finned heat sink.

Table 4.1. IPEM model dimensions.

	Length [cm]	**Width [cm]**	**Height [cm]**
Chip	1.00	1.00	0.075
DBC Cu Top	2.50	2.50	0.025
DBC Alumina	2.50	2.50	0.064
DBC Cu Top	2.50	2.50	0.025
Base Plate	2.80	2.80	0.50
Heat Sink	12.50	12.50	1.00

The IPEM interacts with the motor environment differently depending on the cooling configuration. This thermal interaction occurs through the heat sink, which is either conductively mounted to a surface (for example the motor) or thermally communicates with the air flow via a finned heat sink, as shown in Fig. 4.2. The thermal model of the IPEM takes advantage of the symmetry that is inherent in the modular design and therefore uses a half-symmetry model of the IPEM; the plane of symmetry is represented by an adiabatic surface. The details of the thermal communication between these volumes and the operating environment vary depending on the configuration being evaluated. For example, the fins on the finned heat sink in Fig. 4.2 are modeled using an equivalent heat transfer coefficient as described in detail in the next section.

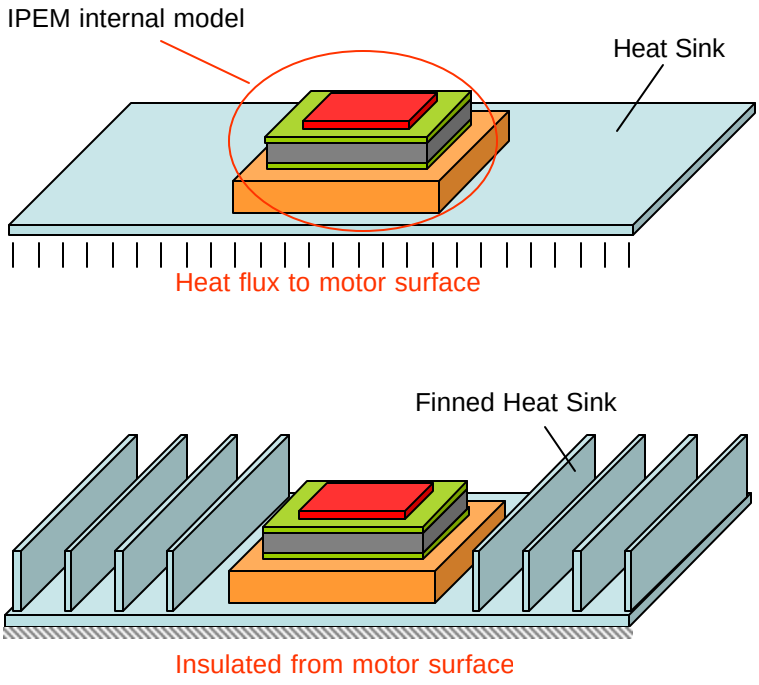

Figure 4.2. IPEM heat sink configurations.

4.2 Material Properties

Like the motor pole model, the IPEM design model considers only steady-state operation and therefore the only properties that are required are the thermal conductivity of each material. This section describes how the thermal conductivities of each of the four sub-components of the IPEM model were estimated.

4.2.1 Chip

The semi-conducting chip is modeled as silicon. Figure 4.2 shows that, over a temperature range between the ambient conditions of 40°C and the maximum operating temperature of 120°C, the thermal conductivity of silicon decreases. In ANSYS, the temperature dependence of silicon was modeled using temperature values interpolated from tabular data [4.4].

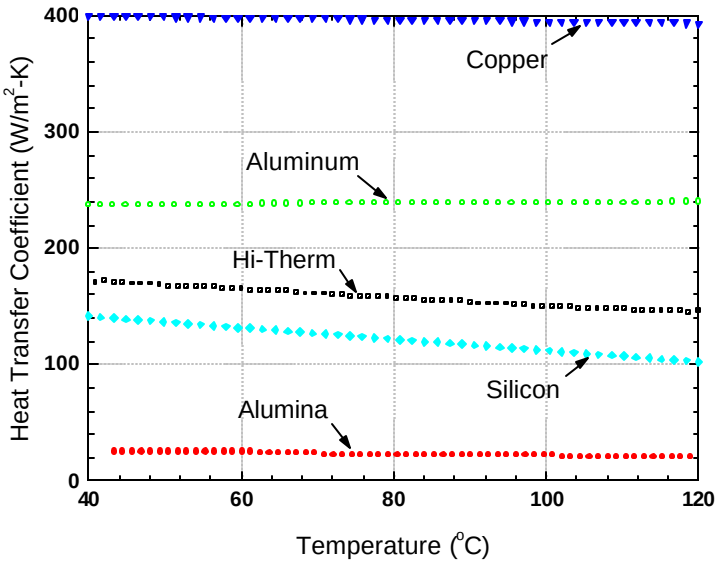

Figure 4.3. Thermal conductivities of IPEM materials as a function of temperature.

4.2.2 Double Bond Copper

The chip is mounted upon a piece of DBC which consists of a core of dielectric material such as alumina or aluminum nitride that is encased thinner layers of copper. The purpose of the DBC is to provide voltage isolation between the IPEM and the surroundings while still providing an effective thermal path. Martens [4.1] assumed that the DBC would use an alumina dielectric which has a relatively low thermal conductivity of 20 W/m-K. The dielectric material assumed for this model is the more advanced Hi-Therm™ aluminum nitride [4.2] which is a high purity ceramic with superior microstructural and chemical uniformity. The thermal conductivity of Hi-Therm™ is almost eight times that of alumina, as shown in Fig. 4.2. Therefore, the temperature rise of the chip, under equivalent operating conditions, is nominally reduced by 20°C. The top and bottom layers of the DBC and the base plate are modeled as copper with a temperature dependant thermal conductivity with values interpolated from the tabular data [4.4].

4.2.3 Heat Sink

The heat sink provides the communication between the IPEM and the thermal environment. The heat sink base is modeled explicitly in the simulation because a large part of the internal thermal resistance is related to lateral heat spreading. In some cooling configurations, the heat sink is conductively coupled to a surface whereas in others, the heat sink is finned in order to interact with a cooling air flow. In the case where the heat sink is interfaced to a solid surface, the temperature over the region of contact is specified and the contact conductance between the heat sink and the mating structure is accounted for at the system model level, as described in Chapter 5. In the case where the heat sink is finned, the

fins are not explicitly modeled; rather, an effective heat transfer coefficient is applied to the finned surface which takes into account the combination of conduction and convection through the fins. The calculation of the effective heat transfer coefficient is described in the next section. The heat sink base material is modeled as aluminum, with a thermal conductivity of 200 W/m-K.

4.3 Thermal Loads

Due to the 120°C maximum temperature limit of the chip, the estimated 20 W/cm^2 of power that is generated within the semi-conducting chip [4.1] is not an insignificant amount of heat. Therefore, it is important to accurately model the thermal loadings incident on the IPEM. A volumetric heat generation is applied to the top 10% of the chip thickness to model the typical concentration of the dissipation that occurs in the upper layer of power devices [4.3]. Therefore, the chip geometry is broken into two volumes; the top section consists of 10% of the total chip thickness and a uniform, volumetric heat generation is applied to it. The bottom section contains the remaining 90% of the chip and has no heat generation.

4.3.1 Contact Resistance

In any composite material, an additional resistance is present at the interface of adjacent materials due to the local effects of surface roughness. At the microscopic scale, the surfaces are not perfectly smooth and therefore conduction of heat between the materials can only occur at those locations where physical contact exists between the two materials. This results in a temperature difference between the two contact surfaces (Fig. 4.4). The contact resistance, $R''_{t,c}$, is defined as [4.4]:

$$R''_{t,c} = \frac{T_A - T_B}{\dot{q}''} \tag{4-1}$$

where T_A and T_B are the temperatures of the bulk materials on either side of the interface and $\dot{q}''$ is the heat flux through the interface. In many conditions the materials themselves are highly conductive, yet the air that fills the gaps between the contact points is highly non-conductive. As a result, it is often the case that contact resistance is a significant contribution to the overall resistance of a composite [4.4].

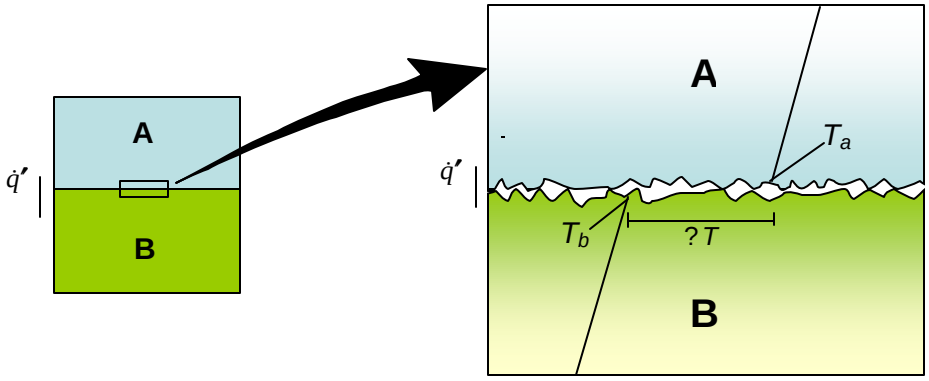

Figure 4.4. Temperature drop due to thermal contact resistance [4.4].

To simulate a practical mounting condition between the component interfaces, a thermal contact resistance of 0.25 K-cm^2/W [4.5], which corresponds approximately to a silicone grease joint under 50 psi, is applied to the contact surfaces between the chip and DBC, DBC and base plate, and base plate and heat sink.

4.3.2 Surface Convection

To determine the relative significance of convection from the top surface of the IPEM, a simplified resistance network shown in Fig. 4.5 is constructed. To simplify the analysis, all surfaces on the model are assumed to be adiabatic with the exception of the top

surface of the chip, and the bottom surface of the base plate, which is assumed to have a surface temperature, T_s, of 80°C.

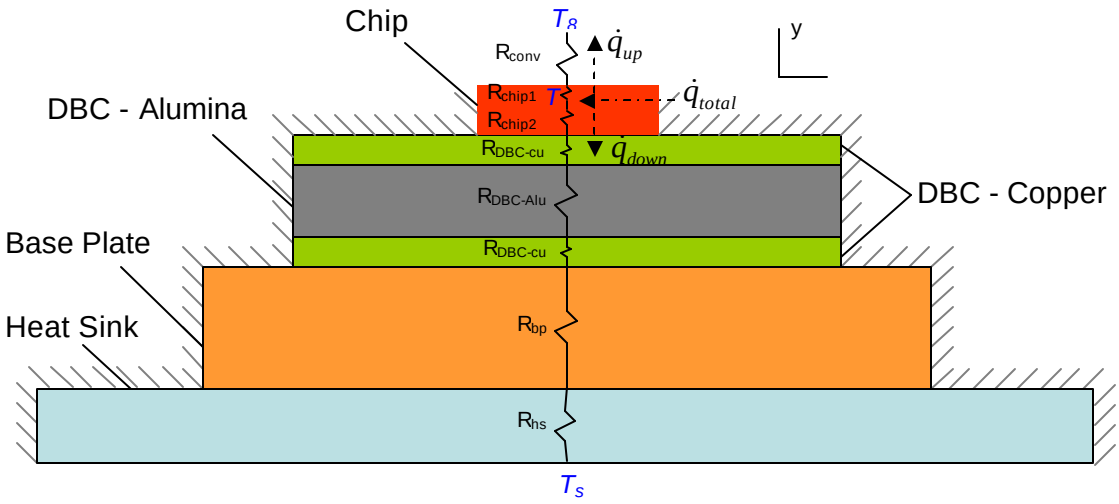

Figure 4.5. IPEM resistance network.

For the convection effects to be significant, the energy that escapes from the top surface of the chip must be on the same order as that which is removed through the base plate. These quantities are calculated using an energy balance:

$$\dot{q}_{total} = \dot{q}_{up} + \dot{q}_{down} \tag{4-2}$$

where $\dot{q}_{down}$ and $\dot{q}_{up}$ represent the heat flowing upwards from the chip surface and downwards from the bottom surface of the base plate respectively and $\dot{q}_{total}$ is the 20 W of power that is generated within the semi-conducting chip. The heat flows $\dot{q}_{down}$ and $\dot{q}_{up}$ are calculated using the general equation:

$$\dot{q} = \frac{\Delta T}{R_{total}} \tag{4-3}$$

where ΔT is the temperature difference across the path and R_{total} is the total resistance across the path.

The total resistance from the top surface to the ambient air is simply the resistance due to the convection from the chip surface, R_{conv}:

$$R_{conv} = \frac{1}{\bar{h} A_c} \tag{4-4}$$

where A_c is the chip cross-sectional area and $\bar{h}$ is the heat transfer coefficient, calculated to be equal to 258 W/m^2-K using:

$$\bar{h} = \frac{\overline{Nu}\, k}{L} \tag{4-5}$$

where k is the conductivity of air at ambient conditions. Laminar flow conditions are likely to exist over top surface of the chip for any reasonable velocity based on the calculation of a Reynolds number (Re) at the surface equal of 4257 using Eq. 4-6:

$$\mathrm{Re} = \frac{\rho v L}{\mu} \tag{4-6}$$

where ρ is the density and μ is the viscosity of air at ambient conditions of 40°C and 1 atm. The air is assumed to be traveling across the length, L, of the chip at a velocity, v, of 10 m/s. The average Nusselt number, $\overline{Nu}$, is calculated using the convection heat transfer correlation for external laminar flow over a flat plate [4.4]:

$$\overline{Nu} = 0.664\, \mathrm{Re}^{1/2}\, \mathrm{Pr}^{1/3} \tag{4-7}$$

where Pr is the Prandtl number of air at the same ambient conditions. Combining Eqs. 4-6 and 4-7, the convective resistance was calculated to be 38.8 W/m^2-K.

The conductive resistance in between the heat generation region and the base plate is the combination of the conduction resistances in the network shown in Fig. 4.5. The conduction resistance, R_{cond}, of each material is calculated using:

$$R_{cond} = \frac{t_i}{k_i A_i} \tag{4-8}$$

where t_i, k_i, and A_i correspond to the thickness, conductivity, and cross-sectional area of each material, respectively.

Using Eq. 4-3, $\dot{q}_{up}$ is calculated to be 1.12 W and $\dot{q}_{down}$ is calculated to be 18.9 W. The amount of heat lost to ambient via convection is therefore relatively small, approximately 5% of the total. Based on this investigation, the convection from the top surface of the chip is neglected in the IPEM mode and the surface is assumed to be adiabatic.

4.3.3 Fin Resistance

To enhance the heat transfer between the heat sink and cooling air in some cooling configurations, fins are incorporated with the heat sink. An analytical model was developed using the Engineering Equation Solver (EES) software [4.6] in order to estimate the effective heat transfer coefficient, h_{eff}, that can be applied to the surface of the heat sink in order to represent the presence of the fins without requiring an explicit model of each fin. The fin model also enables some optimization of the finned surface geometry, including the spacing and placement of the fins on the heat sink base surface.

The equation for the equivalent thermal resistance of a single fin is similar to that of convection resistance with the addition of an overall efficiency of the finned surface term, $?_o$, as shown in Eq. 4-9.

$$R_{fin} = \frac{1}{h_o hA} \tag{4-9}$$

Here A is the total fin surface area. Therefore, h_{eff} of the finned surface is equal to:

$$h_{eff} = h_o h \tag{4-10}$$

The overall efficiency is defined by Eq. 4-11 through Eq. 4-20.

$$h_o = 1 + \frac{N A_f}{A_t}\left(1 - h_f\right) \tag{4-11}$$

Here N is the number of fins, $?_f$ is the efficiency of a single fin, and A_f and A_t are the fin surface area and the total surface area respectively. The total surface area is defined by:

$$A_t = N A_f + A_b \tag{4-12}$$

where A_b is the exposed surface area of the base (i.e., the unfinned area). The fin surface area is defined by:

$$A_f = 2w L_c \tag{4-13}$$

where w is the fin width in the flow direction. The corrected fin length, L_c, is based on assuming equivalence between heat transfer from the actual fin with tip convection and heat transfer from a longer, hypothetical fin with an adiabatic tip [4.4]:

$$L_c = L + \left(\frac{t}{2}\right) \tag{4-14}$$

where L is the actual length and t is the thickness of the fin. The efficiency of each individual fin is calculated according Eq. 4-15 assuming an adiabatic fin tip:

$$h_f = \frac{\tanh(mL_c)}{mL_c} \tag{4-15}$$

where m is the fin constant:

$$m = \sqrt{\frac{h \cdot P}{k \cdot A_c}} \tag{4-16}$$

where k is the conductivity of the fin. P is the fin perimeter A_c is the fin cross-sectional area.

The heat transfer coefficient, h, through the fins is calculated by assuming two adjacent fins behave as parallel plates. The bulk velocity through each set of parallel plates is calculated using the resistance flow network described in Chapter 5.

4.4 References

[4.1] Martens, T. "Double-Sided Cooling of IPEMs using Miniature Heat Pipes," Masters Thesis, Departments of Electrical and Mechanical Engineering, University of Wisconsin, Madison, 2003.

[4.2] Hi-Therm™ Aluminum Nitride, Marcus Materials Co., 9 Renee Court, Northgate Commons, Newark, DE 19711, http://www.mcelwee.net, Phone: (302) 731-7519, Fax: (302) 691-4794.

[4.3] Chow, T.P. and Shen, Z., "An Analytical IGBT Model for Power Circuit Simulation," Proceedings of the 3rd Intl. Symposium on Power Semiconductor Devices and ICs (ISPSD), pp. 79-82, April 22-24, 1991.

[4.4] Incropera, F.P., DeWitt, D.P., Fundamentals of Heat and Mass Transfer - 4th Ed., John Wiley & Sons, Inc., NY, 1996.

[4.5] Yovanovich, M.M., Culham, J.R., Teertstra, P., "Calculating Interface Resistance," Electronics Cooling, May 1997.

[4.6] Engineering Equation Solver (EES) V7.041, F-Chart Software, Box 44042, Madison, WI 53744, www.fchart.com, info@fchart.com, Phone: (608) 836-8531, Fax: (608) 836-8536.

5 Model Integration

The motor pole, air passage, and IPEM models that were developed and described in Chapters 2, 3, and 4, interact based on conductive coupling or thermal contact with air flowing through the system. In order to model an integrated system it is necessary to determine the air velocities and heat transfer coefficients within the system. These calculations are dependent on the placement of the IPEM within the system as well as the air flow passages available. The first section of this chapter describes the overall modeling approach used to interface the computational-level models in order to study the system level performance of an arbitrary thermal management configuration. The rest of this chapter is then broken down into separate sections describing the two motor pole/IPEM configuration schemes that have been configured. Section 5.2 describes the methodology and calculations associated with directly affixing (i.e., conductively coupling) the IPEM to the motor. In Section 5.3, the previously described calculations are altered to take into account the effects of thermally insulating the IPEM from the motor pole.

5.1 Basic Modeling Approach

Figure 5.1 shows an overview of the entire modeling approach. Because there is so much integration between the different component models, the modeling approach is somewhat complex.

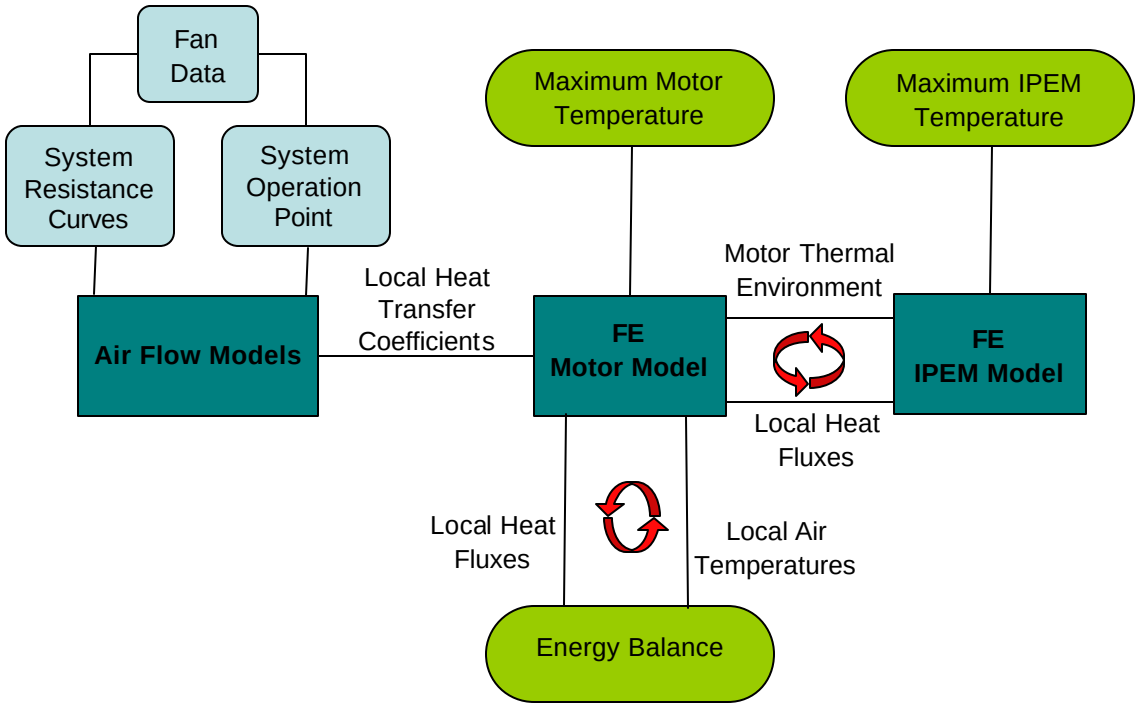

Figure 5.1. Overview of system modeling approach.

The first step of the modeling approach involves obtaining the distribution of the flow through the system using the component resistance curves associated with the model geometry and the fan curve data. Once the system operating point is determined, the local heat transfer coefficients over all of the exposed surfaces may be calculated using the air flow models; these heat transfer coefficients are then used as inputs to the motor model. The local air temperature distribution within the motor is determined using an iterative process based on the energy balances for the air flow. There is also an interaction between the motor and the IPEM, depending on where the IPEM is located. The effects of the motor/IPEM interaction must be accounted for in both models. The result of this system level model is the maximum temperature for each component.

5.2 IPEM Thermally Affixed to Stator

Figure 5.2 shows the first motor pole/IPEM thermal management strategy which was the original concept for the modular motor/controller system. Here the IPEM is conductively coupled to the stator, with the bottom of the baseplate of the IPEM thermally attached to the tooth of the stator pole. As shown in Fig. 5.3, in this configuration the IPEM is not air cooled and therefore a finned heat sink is not used.

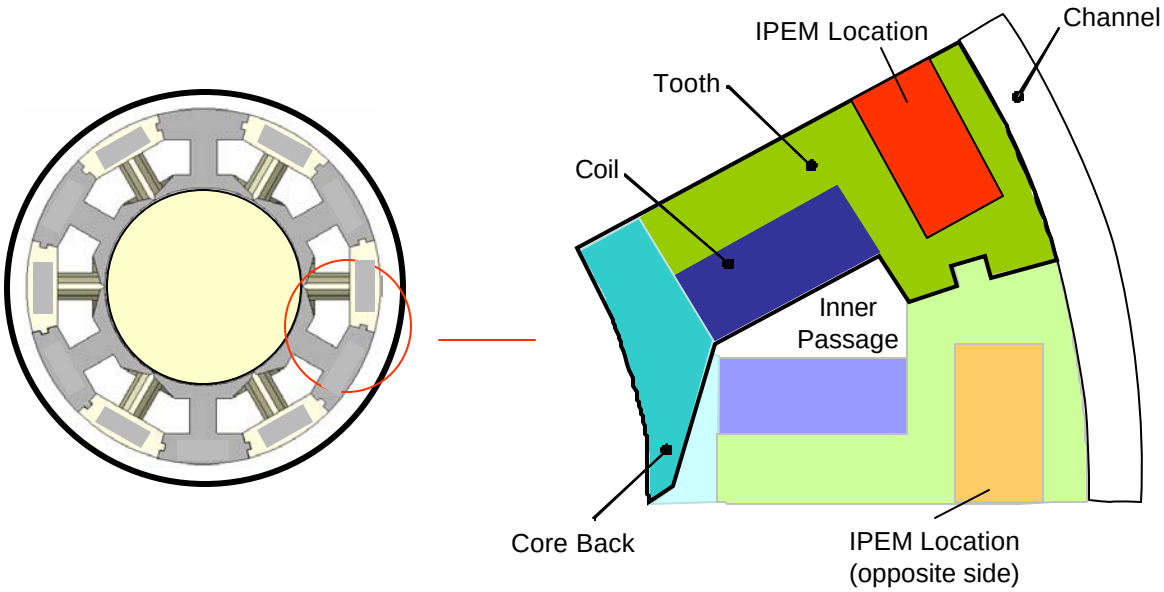

Figure 5.2. IPEM placement for initial configuration scheme.

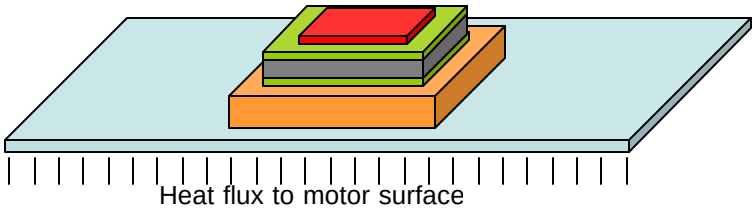

Figure 5.3. IPEM geometry for initial configuration scheme.

5.2.1 Local Heat Transfer Coefficients

The first step in modeling any of the cooling configurations is to determine the distribution of the flow through the system. By coupling the motor model described in Chapter 2 and the inner passage and channel models described in Chapter 3, the total system resistance curves are determined. The system resistance curves are used to calculate the heat transfer coefficients on the motor surfaces and determine the air temperatures within the motor passages.

The motor is cooled assuming a self-circulation cooling method, in which a fan mounted directly on the armature shaft of the motor provides the cooling air. When the armature rotates, the fan drives the cooling air through the air passages within the motor. To calculate the heat transfer coefficients, the air flow through the internal passage and the channel and the local velocities seen on the surfaces within these passages must be determined based on the simultaneous consideration of the characteristics of the fan used to force air through the air passage and the fluid resistance associated with these passages. Because of the relatively large pressure drop between the ambient air and the interior passages of the motor, the NuAire SMD [5.1] fan is modeled due to its relatively low pressure drop over a range of volumetric flow rates. The fan performance curve, determined using the performance data provided by the manufacturer, is shown in Fig. 5.4.

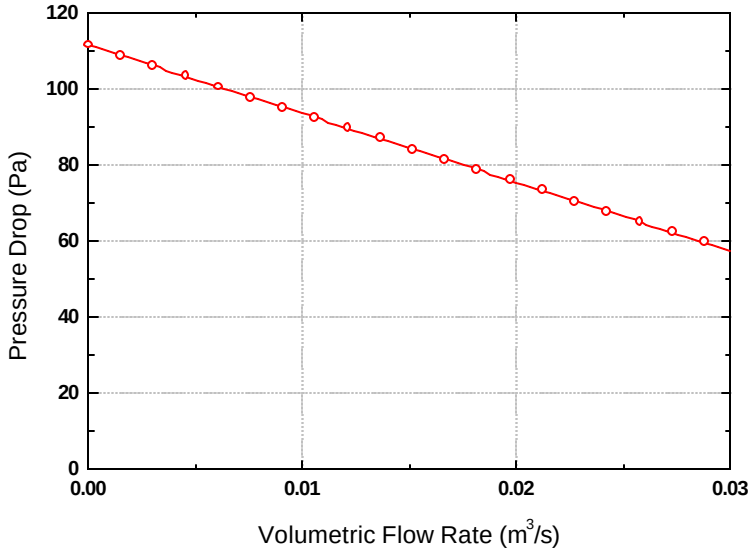

Figure 5.4. Fan performance curve.

The pressure drop data predicted by the FLUENT simulations of the interior passage and channel models are used to create system resistance curves which are power law expressions of the pressure drop (ΔP) as a function of airflow ($\dot{Q}$):

$$\Delta P = K\ r\ \dot{Q}^{n} \tag{5-1}$$

where K is the system load factor which is adjusted to match the FLUENT results, ? is the density of air, and n is a constant that varies between 1 and 2 depending on whether the flow is completely laminar (n = 1) or completely turbulent (n = 2); n is also adjusted to match the FLUENT results. Equations 5-2 and 5-3 are obtained by applying a power-fit curve to the pressure drop versus volumetric flow rate data using the Engineering Equation Solver (EES) software [5.2] and are used to represent the pressure drop as function of airflow for the interior passage and the channel.

$$\Delta P_{passage} = 2.79e^{4}\ \dot{Q}_{passage}^{1.39} \tag{5-2}$$

$$\Delta P_{channel} = 1.56e^{7}\ \dot{Q}_{channel}^{1.90} \tag{5-3}$$

The interior passage and channel are in parallel; therefore, the system curve presented by both passages to the fan may be constructed by realizing that at any given value of the pressure difference, ? *P*, the total air flow rate is equal to the sum of the air flow through the interior passage and the channel. This is shown in Fig. 5.5.

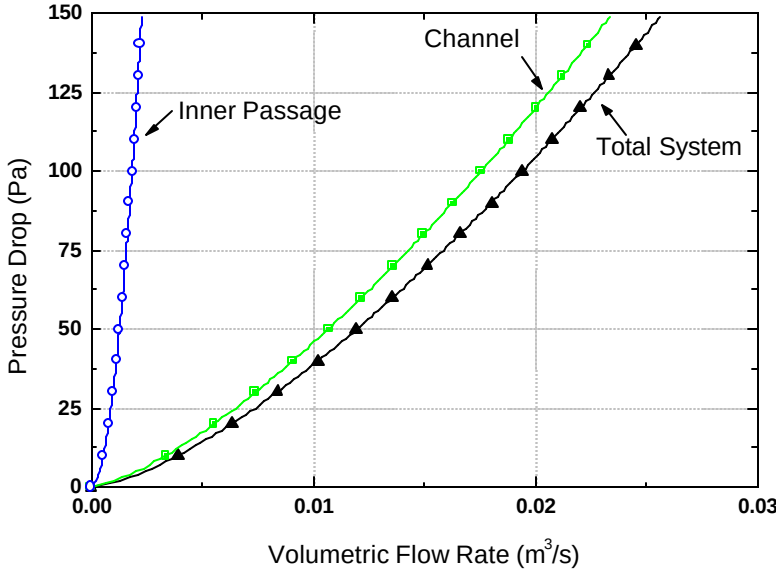

Figure 5.5. System resistance curves.

The point of operation for the system is the intersection between the total system resistance curve and the fan performance curve, as shown by the small circle in Fig. 5.6.

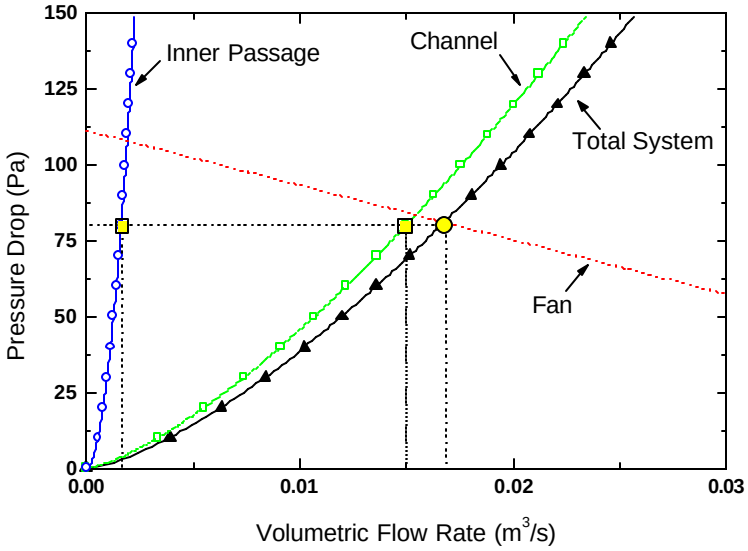

Figure 5.6. System point of operation.

The distribution of the total flow through the interior passage and channel is calculated using the volumetric flow rate of the passage and channel at the pressure drop that corresponds to the point of operation of the system. These points are indicated by the small squares in Fig. 5.6. The inlet velocity to the passage, v, is defined by:

$$v = \frac{\dot{Q}}{A_c} \tag{5-4}$$

where A_c is the cross-sectional area for the air flow at the inlet to the passage. Using Eq. 5-4 the air velocity at the inlet to the interior passage for each pole segment and the circumferential, external channel is determined.

The velocity through the inner passage can be used to determine the heat transfer coefficients for the boundary conditions of the motor model based on the previously described CFD results. As shown in Fig. 5.7, a vertical line at the 0.46 m/s inlet velocity allows the heat transfer coefficient for each surface to be established.

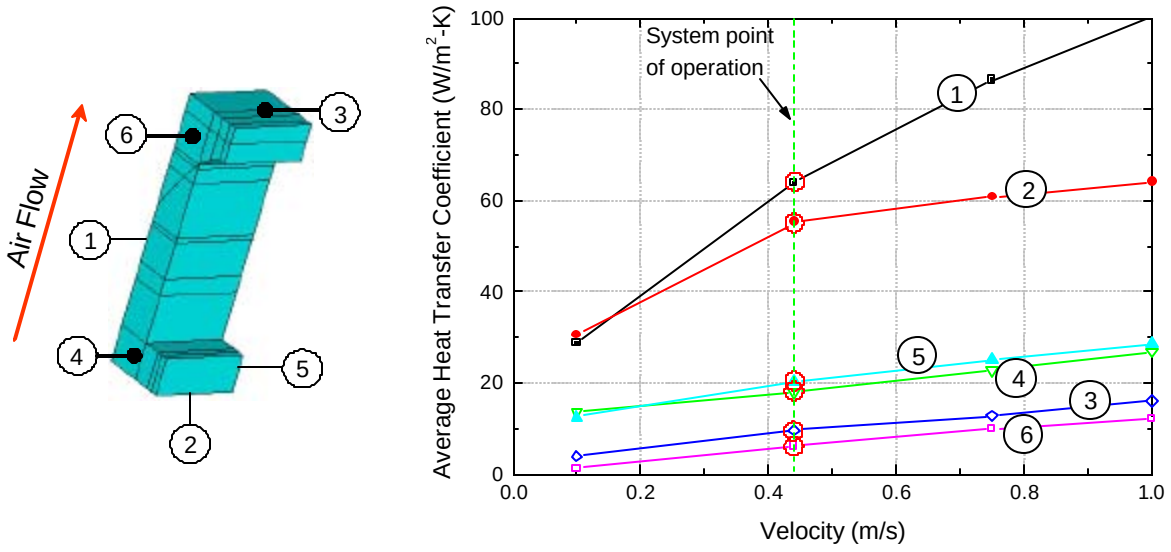

Figure 5.7. Heat transfer coefficients on Side 1 of the coil at v = 0.46 m/s system point of operation.

The same procedure is used for the other surfaces in the inner passage of the motor. Table 5.1 summarizes the heat transfer coefficients for all surfaces in the inner passage for both the air inlet (Side #1) and air outlet (Side #2) positions at an air velocity of 0.46 m/s.

Table 5.1. Heat transfer coefficients (W/m^2-K) for motor pole surfaces at v = 0.46 m/s.

		Side #1	Side #2
Coil	**1**	63.88	53.67
	2	55.11	31.14
	3	9.60	20.16
	4	18.01	14.02
	5	20.45	15.88
	6	6.09	18.20
Core Back	**1**	8.71	28.04
	2	10.52	2.12
	3	43.64	3.52
Tooth	**1**	12.18	26.56
	2	30.13	11.86
	3	13.53	32.21
	4	39.82	37.90

The heat transfer coefficients along the surface of the channel are determined using the calculated 30.7 m/s velocity through the channel and the EES model for the channel described in Chapter 3. For input into the ANSYS model, the channel is broken into three separate segments and the average heat transfer coefficient within each section is applied to the model. Figure 5.8 shows these heat transfer coefficients along the 90 mm length of the channel.

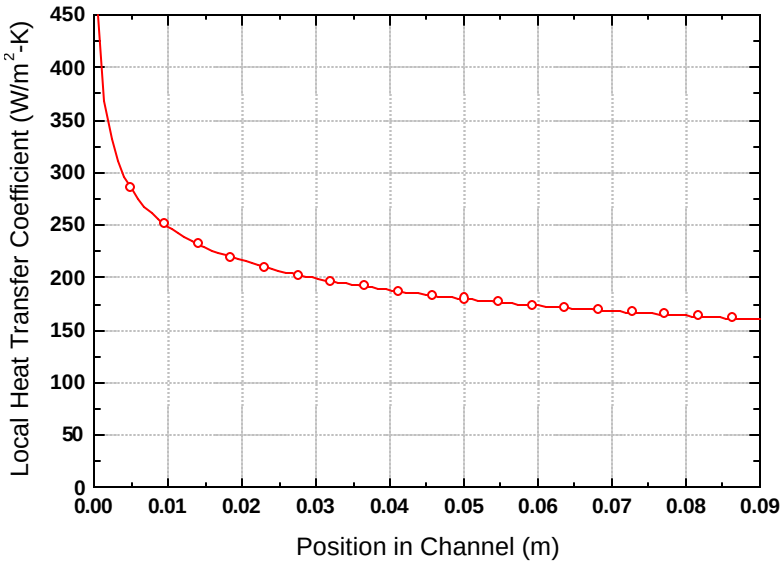

Figure 5.8. Local heat transfer coefficients in channel at v = 30.7 m/s.

5.2.2 Local Air Temperatures

The heat transfer coefficients over each surface of the motor provide only part of the boundary condition; the local air temperatures exposed to those surfaces must also be specified. There is a finite flow rate of air and therefore it is substantially heated as it passes through the motor; this sensible temperature rise may account for a significant fraction of the total temperature rise experienced by the motor and the IPEM. Instead of trying to determine the exact temperature at every point along the inner passage of the motor, the

passage is broken into several sections, Zones A, B, and so on. The average temperature within these sections is calculated using an iterative process and applied as a boundary condition to the motor model.

Figure 5.9 shows the iteration process, which is initiated by assuming that the air temperature within the zone is equal to the air temperature entering the motor, or T_8 (ambient air or air that has been slightly heated by its passage through the fan). The motor model is run and used to determine the heat flux from the surfaces of the motor within the zone. An energy balance, Eq. 5-5, is used to relate the heat flux in the zone, $\dot{q}''$, to the bulk temperature rise of the air using the air flow heat capacity rate:

$$\dot{q}'' = \dot{m} c \left(T_{out} - T_{in} \right) \tag{5-5}$$

where $\dot{m}$ is the mass flow rate of the air, c is the specific heat of the air, and T_{in} and T_{out} are the temperatures at the zone inlet and exit. The heat flow calculated in ANSYS is used in Eq. 5-5 to calculate the bulk temperature rise within the section. If the error between the calculated average temperature, T_{avg}, in the zone and the initial guess temperature, T_g, is greater than 1% then T_{avg} is used as the new guess value for the air in the zone and the motor model is run again. This iterative process is repeated until the error between the guess temperature and the zone outlet temperature calculated from the model is less than 1%.

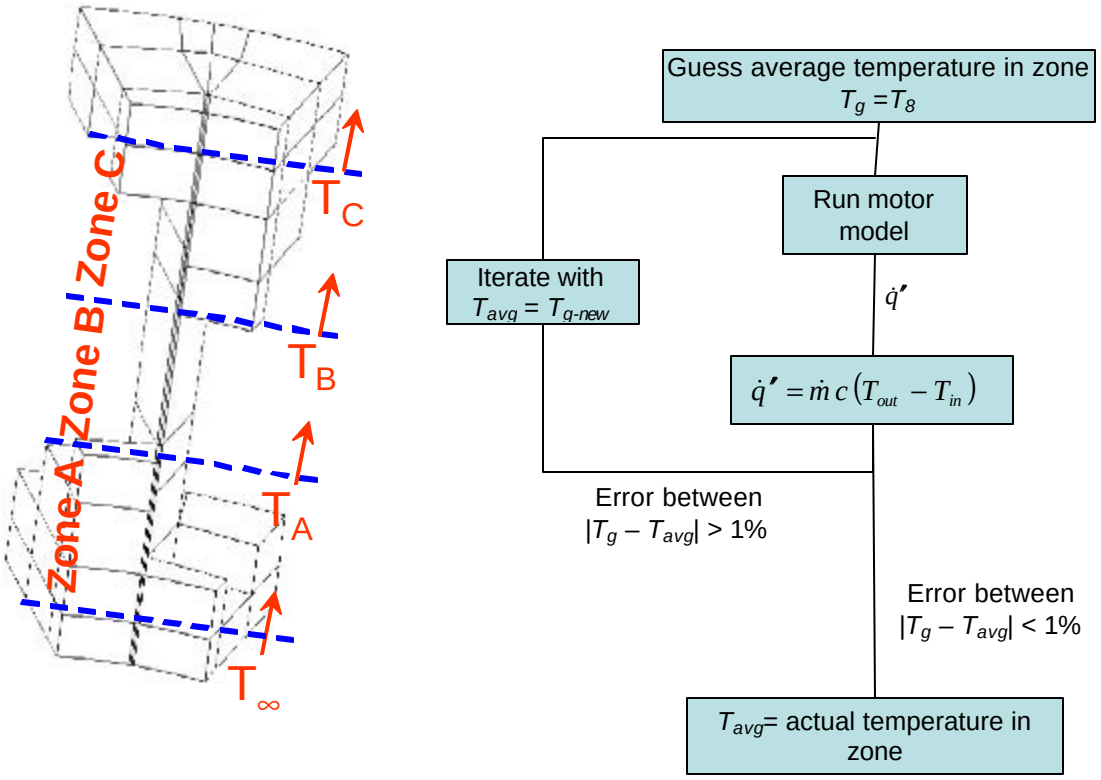

Figure 5.9. Location of zones A, B, and C and iterative calculations for determining local temperatures in inner passage.

This same iterative process used to calculate the inner passage air temperatures is completed to determine the air temperatures within the motor channel. The channel is broken into three equal zones: Zones D, E, and F along the direction of the airflow as shown in Fig. 5.10. The higher flow rates through the external passage lead to much lower temperature rise of the air than in the motor passage.

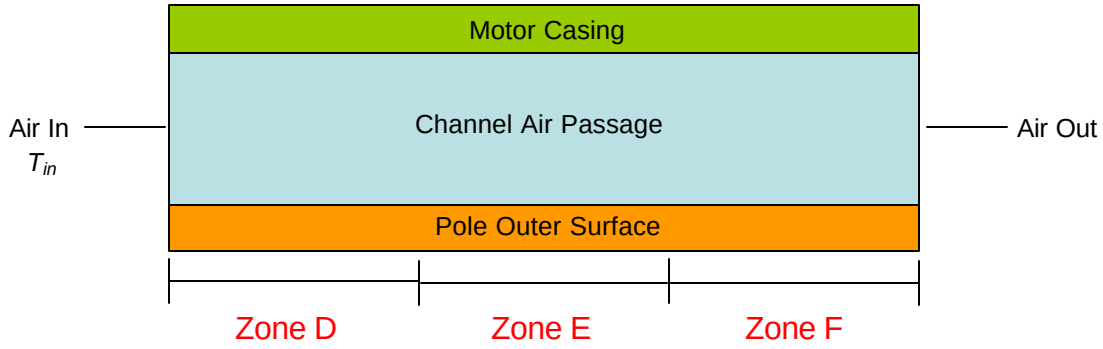

Figure 5.10. Zones for channel air temperature iterations.

The presence of the two air channels makes a significant difference in the maximum temperatures in the motor. To analyze the effects of the two channels on the motor temperature, three different models were run. The first, shown on the far left of Fig. 5.11, is the 'original' motor model, and contains both the inner passage and channel. If the inner passage is effectively removed from the motor by modeling its surfaces in the motor as adiabatic, the motor temperatures increase. This study shows how significant a part the outer channel plays in the cooling of the motor, as removing it from the model and forcing the air to flow only through the inner passage results in a overall temperature increase in the motor of approximately 100°C.

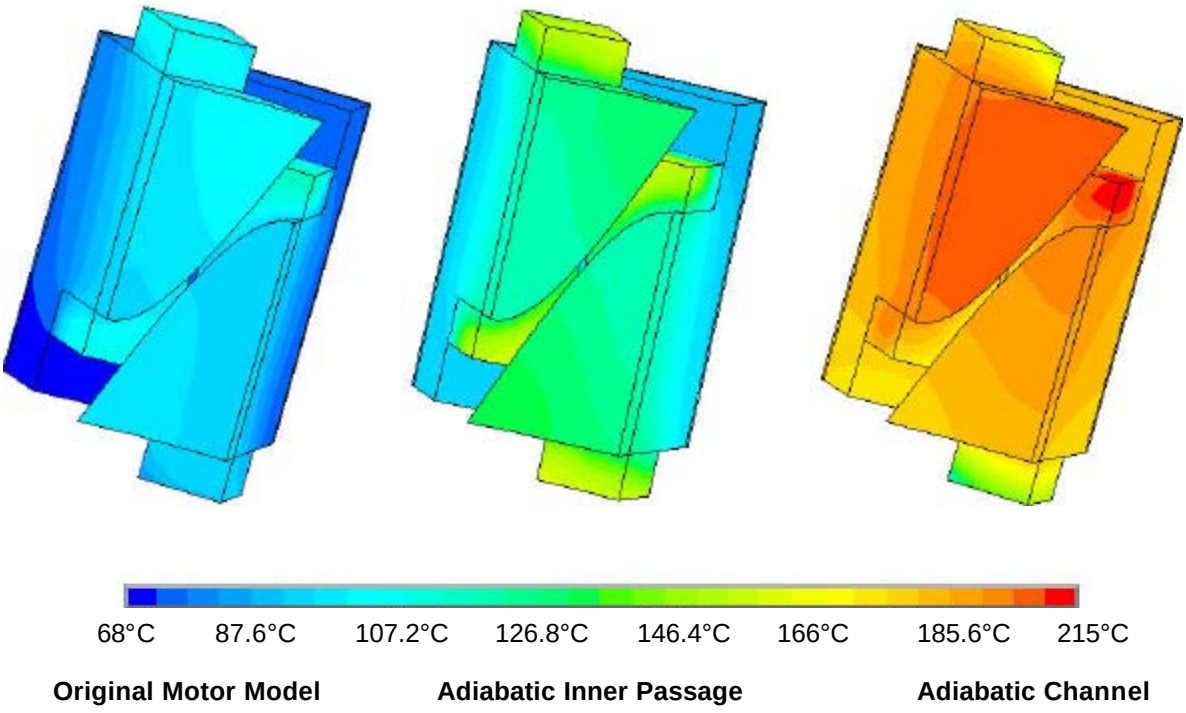

Figure 5.11. Temperature distribution in motor for original motor model (with both inner passage and channel), motor with adiabatic inner passage, and motor with adiabatic channel.

5.2.3 Maximum Temperatures in IPEM and Motor

The final step in the process is to determine the maximum temperature in the motor pole and IPEM. This is done by first applying the 20 W/cm^2 average heat flux that characterizes the bottom surface of the IPEM to the motor surface as a uniform heat flux at the IPEM mounting location. Next, the ANSYS motor model is run in order to determine both the maximum temperature in the motor, and the average temperature of the motor surface at the mounting location for the IPEM.

A key objective of this project is the design of a practical motor configuration that provides sufficient cooling so that the IPEM and motor are kept below their rated maximum temperatures. Figure 5.12 illustrates the maximum temperature in the IPEM and the motor

as a function of the fraction of the flow that passes through the outer channel. The two curves for the IPEM temperature are related to the IPEMs that are mounted on the inlet versus the outlet end of the motor poles. In order to maintain modularity in the motor configuration, every other IPEM is located on the outlet side of the motor where it is exposed to stagnant air which has been significantly heated as it passed through the motor. This stagnant, warmed air results in significantly higher maximum temperatures in the outlet side IPEMs.

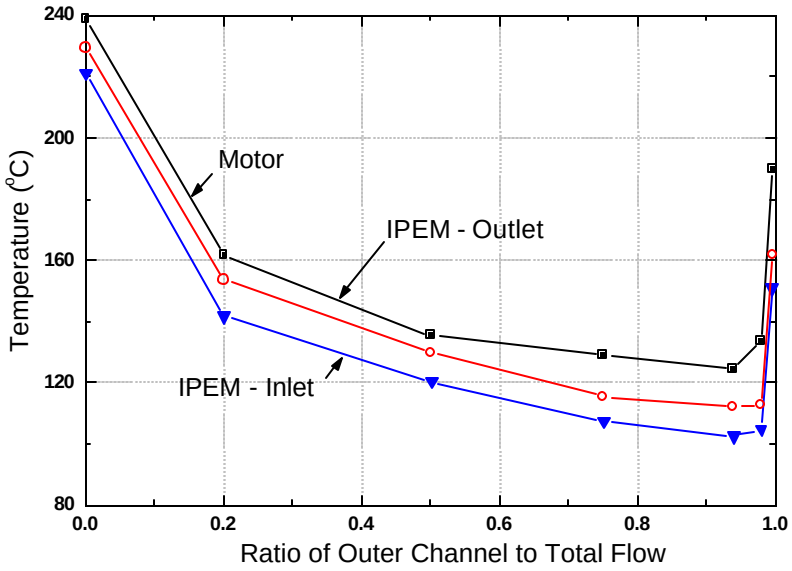

Figure 5.12. Maximum temperature of components as a function of the ratio of flow through the channel.

When the flow ratio through the channel is zero, meaning that no channel is modeled in the simulation, the maximum temperatures in all components are significantly higher than 200°C. These high temperatures are due to the fact that the channel is very effective at cooling the outer surfaces of the motor. As flow through the channel is increased by increasing the channel height, the temperatures in the motor and IPEM decrease until they reach a minimum at a channel ratio of approximately 0.95, which corresponds to a channel

height of 1 cm. Any further increases in the flow ratio through the channel significantly restricts flow through the inner passage, which is very effective at cooling the concentrated windings within the motor pole. As the temperatures within the windings increase, the maximum temperatures in the motor pole and IPEMs increase as well.

Figure 5.13 shows the temperature distribution through the motor pole for the optimum channel height of 1 cm. Notice that the highest temperatures in the motor occur where the IPEM is mounted. There is also a significant temperature increase moving from the inlet side of the motor to the outlet side.

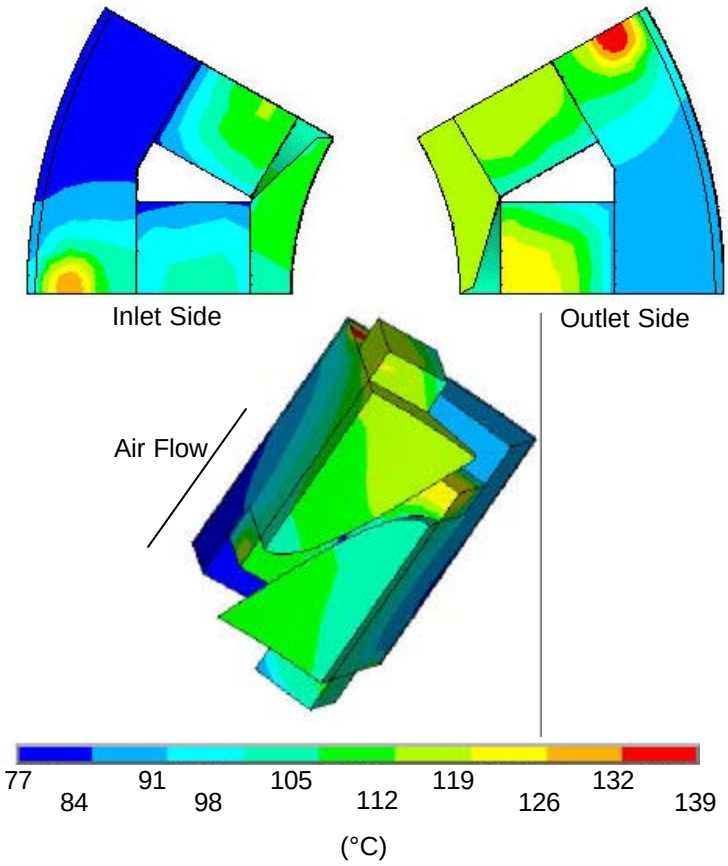

Figure 5.13. Temperature distribution in motor with IPEM thermally attached for a channel height of 1 cm.

Figure 5.14 shows the temperature distributions through both the inlet and outlet side IPEMs. While the temperature contours are approximately the same in both IPEMs, the outlet side IPEM experiences temperatures on average almost 8°C higher than the IPEM on the inlet side.

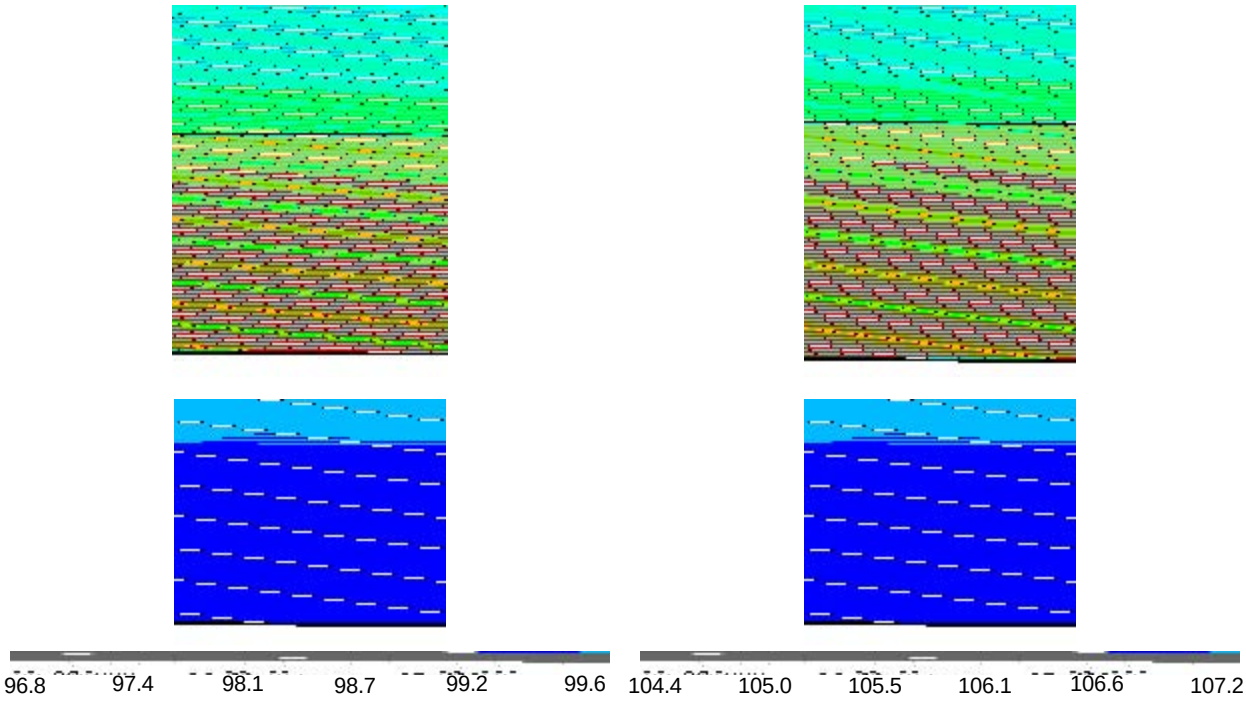

Figure 5.14. Temperature distributions in the inlet side and outlet side IPEMs for a channel height of 1 cm.

Based on these results, it would not be possible to simply conductively mount the IPEMs on the stator poles without providing some mechanism for cooling the outer surface of these poles, in this case an outer flow channel. With the presence of an outer flow channel, this configuration becomes a marginally feasible approach. However, this channel is undesirable from the standpoint of manufacturing.

5.3 IPEM Insulated from Motor

The previous configuration in which the IPEM was directly mounted on the motor had two major disadvantages. A localized area of high temperature was created on the surface of the motor at the IPEM mounting location causing a thermal resistance related to heat spreading. Also, the location of the IPEM in relation to the air flow from the fan resulted in little to no air cooling and the IPEM had to be cooled indirectly through the air by the motor. This implies that the motor temperature must be less than the IPEM temperature (as the motor lies closer to the heat sink, the air, than the IPEM). However, the IPEM temperature limit is less than that of the motor and therefore this is not the most advantageous configuration. A more attractive alternative would couple the IPEM directly to the air flow and insulate it from the motor, as shown in Fig. 5.15. Here, the IPEM is mechanically (but not thermally) attached to the motor in the outer channel and interfaced with the air flow via a finned heat sink shown in Fig. 5.16. In this configuration the air flow from the fan is used to cool both the motor and the IPEM.

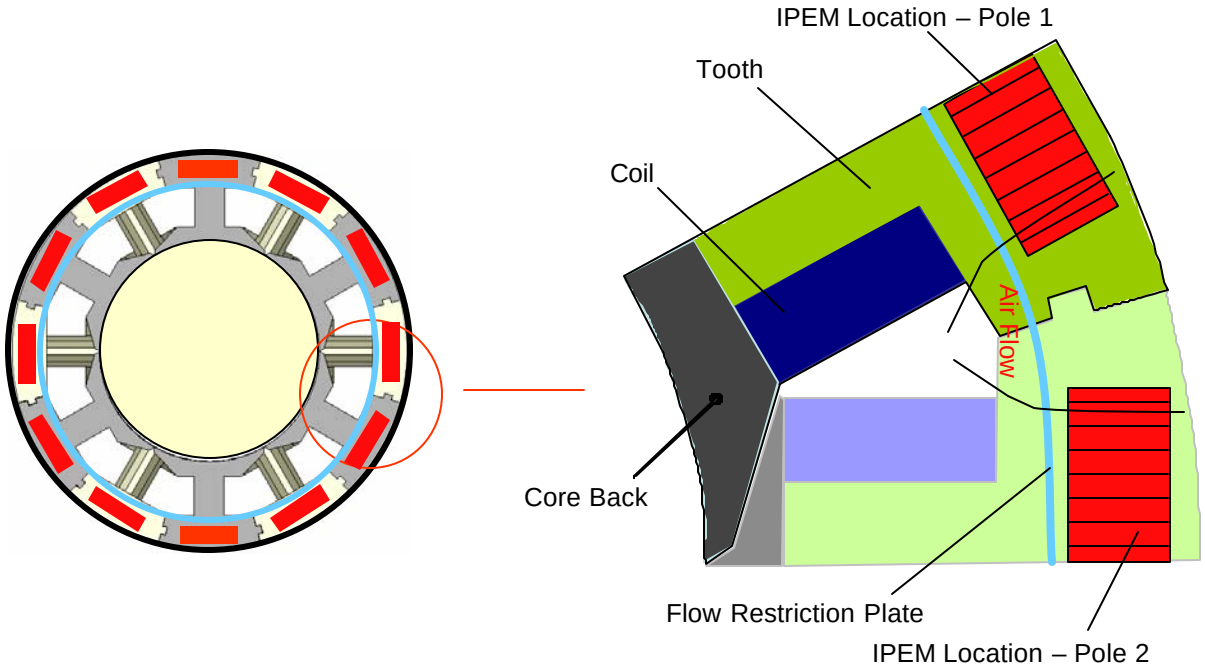

Figure 5.15. IPEM placement for insulated configuration scheme.

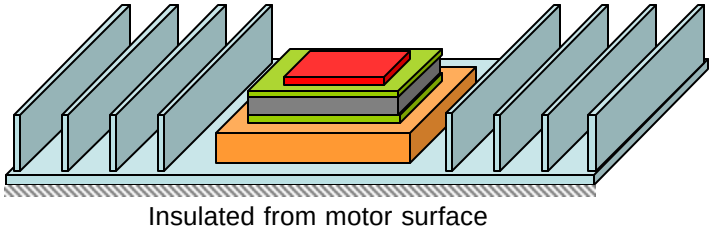

Figure 5.16. IPEM geometry for insulated configuration scheme.

5.3.1 System Resistance Curves

This new system configuration changes the total system resistance curves. There are now two air paths in series: the IPEM fins followed by the inner passage, which remains unaltered. The pressure drop in the fins, $?P_{fin}$, is calculated using Eq. 5-6 [5.3]:

$$\Delta P_{fin} = \frac{1}{2}\, r\, v_{fin}^2 \left(f_{fin}\, \frac{L}{D_{hy,\,fin}} + K_{e,\,fin} + K_{c,\,fin} \right) \tag{5-6}$$

where v_{fin} is the air velocity through the fins, *?* is the air density, is the friction factor of the fins, $D_{hy,fin}$ is the hydraulic diameter of fins. The friction factor, f_{fin}, is defined by Eq. 5-7:

$$f_{fin} = \frac{0.1268}{\mathrm{Re}_{fin}^{0.3}} \tag{5-7}$$

where Re_{fin} is the Reynolds number of the airflow through the fins. Here $K_{e,fin}$ and $K_{c,fin}$ are coefficients based on the fin cross-sectional area, A_{fin}, and the outlet area of the fan, calculated using Eqs. 5-8 and 5-9.

$$K_{e,\,fin} = 0.4\left[1 - \frac{A_{fin}}{A_{inlet}}\right] \tag{5-8}$$

$$K_{c,\,fin} = \left[1 - \frac{A_{fin}}{A_{inlet}}\right]^2 \tag{5-9}$$

The volumetric flow rate of the air through the fins is calculated using Eq. 5-10,

$$\dot{Q}_{fin} = v_{fin}\, A_{fin}\, N_f \tag{5-10}$$

where N_f is the number of fins.

The total system resistance curve is defined by the sum of the pressure drops in the fins and inner passage, since the air passages are in series as shown in Fig. 5.17.

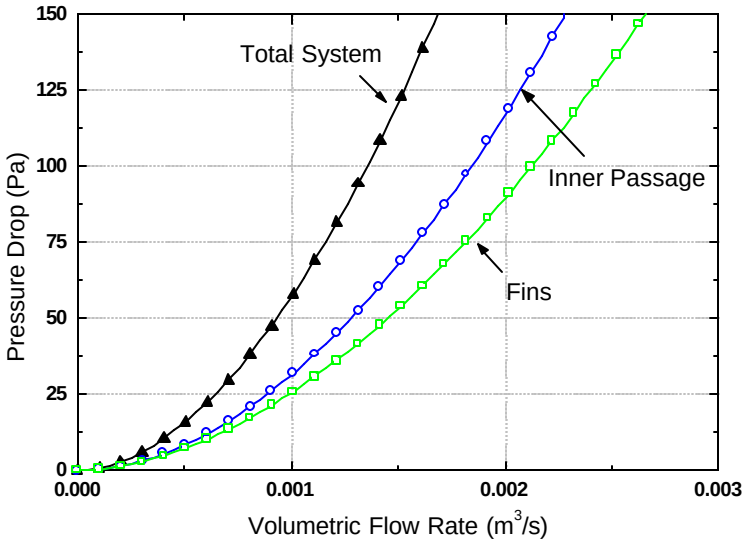

Figure 5.17. System resistance curves.

Again, the point of operation for the system is where the total system pressure drop and the fan curve intersect as shown in Fig. 5.18. This intersection point allows for the estimation of the air flow through each passage.

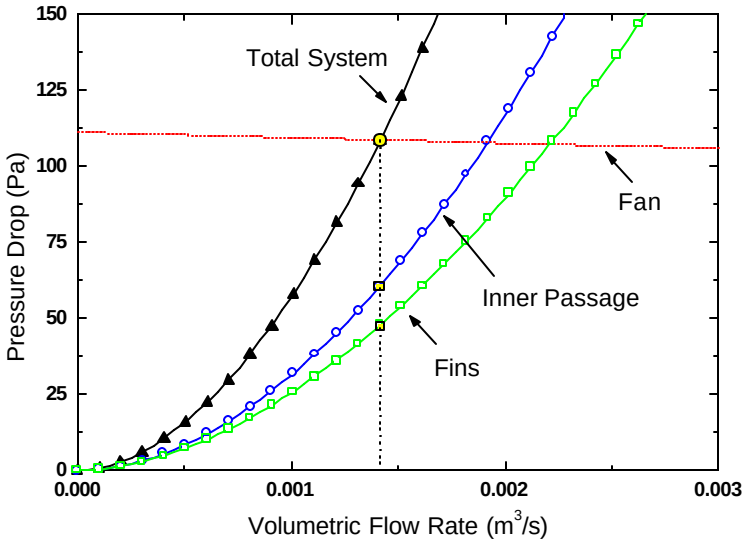

Figure 5.18. System point of operation.

5.3.2 Maximum Temperatures in IPEM and Motor

The remainder of the system integration procedure remains essentially the same for this second configuration scheme. The temperature distribution in the motor and IPEM are shown in Fig. 5.19 and Fig. 5.20.

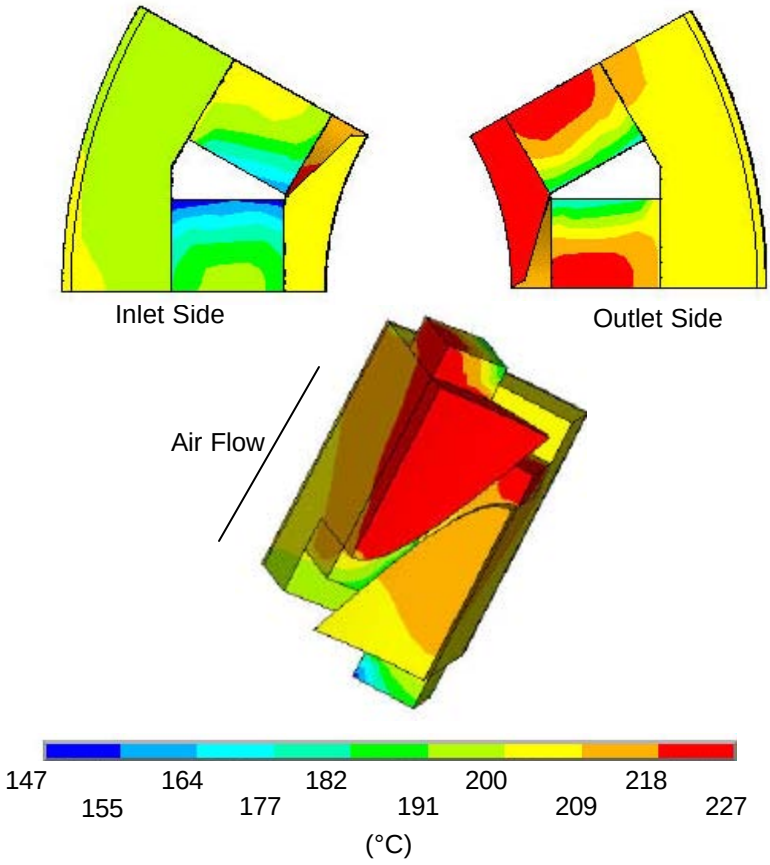

Figure 5.19. Temperature distribution in motor with IPEM thermally insulated from motor surface.

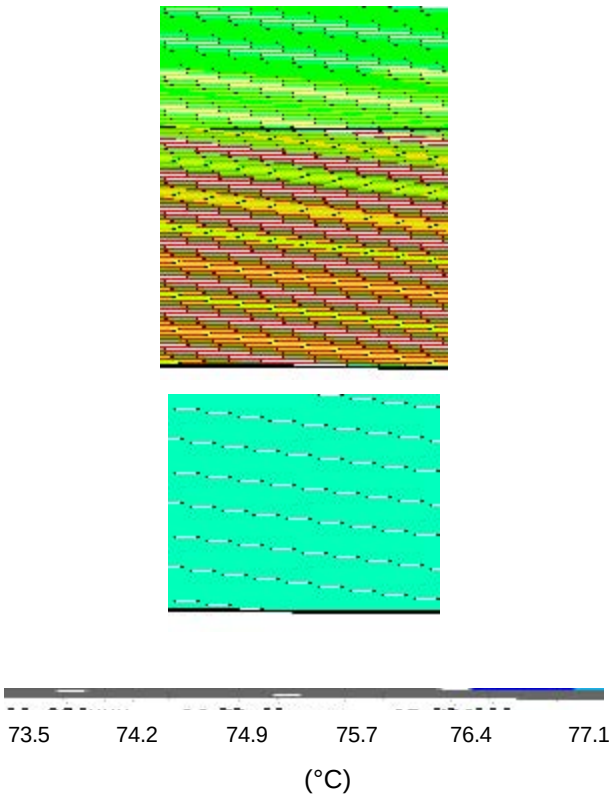

Figure 5.20. Temperature distribution in IPEM for thermally isolated configuration.

This configuration is very effective at cooling the IPEM; temperatures are on average 30°C less than in the previous configuration. Also, the temperature distribution through the motor is significantly different in this configuration. There is a much greater increase in the local air temperatures within the motor due to the removal of the outer channel, leading to a lower air flow rate since the inner air passage is fairly restrictive. Also, the primary thermal load on the motor is now related to the coil since the IPEMs are all decoupled from the tooth. These factors together result in a significant increase in overall motor temperature between the inlet and outlet sides of the motor. The maximum motor temperature is located within the concentrated windings for this configuration.

5.4 References

[5.1] NuAire Ltd., Western Industrial Estate, Caerphilly, Mid-Glamorgan, UK CF83 1XH, www.nuaire.co.uk, info@nuaire.co.uk, Phone: 02920 885911, Fax: 02920 887033.

[5.2] Engineering Equation Solver (EES) V7.041, F-Chart Software, Box 44042, Madison, WI 53744, www.fchart.com, info@fchart.com, Phone: (608) 836-8531, Fax: (608) 836-8536.

[5.3] Fay, J.A., Introduction to Fluid Mechanics, The MIT Press, Cambridge, MA, 1994.

6 Experimental Validation

The overall goal of this project is the development of a modeling methodology that is capable of accurately predicting the thermal response of the motor and IPEM components in the context of a specific cooling configuration. The accuracy of the modeling technique must be verified through experiment in order to be applied with confidence to the design of the thermal management system. The eventual experimental verification will utilize two SMC poles that are nominally identical to those modeled in the simulations which have been described in the previous chapters. These poles will be mounted in an enclosure that provides an environment that is consistent with the air flow in a subsection of the motor assembly. Unfortunately, these motor poles were not available within the timeframe of this project. However, it is still possible provide some experimental verification of the general modeling methodology using an alternative experimental configuration.

A new set of models was developed using the tools and methodology described in previous chapters. These models predicted the thermal response of a wound E-type ferrite core transformer rather than the more complex stator poles. These E-type poles were procured and used as the basis of an experimental test setup. The comparison of the measured and predicted behavior of these poles provides a measure of the accuracy of the thermal models. Also, the test facility is constructed in a flexible manner and therefore allows the installation of alternative and more advanced stators and additional heaters which can be used to simulate integrated power electronics components.

This chapter describes the new thermal models that were constructed, the experimental setup and procedure, and the experimental results. A comparison of the measured and predicted results is also provided.

6.1 E-Core Finite Element Models

This section describes the finite element model of the E-type cores and associated air passages that were used in the experiment. These finite elements models were developed using the ANSYS and FLUENT software. The ANSYS code required to generate the thermal model is found in Appendix F.

6.1.1 Thermal Model of the E-Core

The geometry modeled is a 'pole' consisting of two identical E-cores energized by a concentrated winding, as shown in Fig. 6.1.

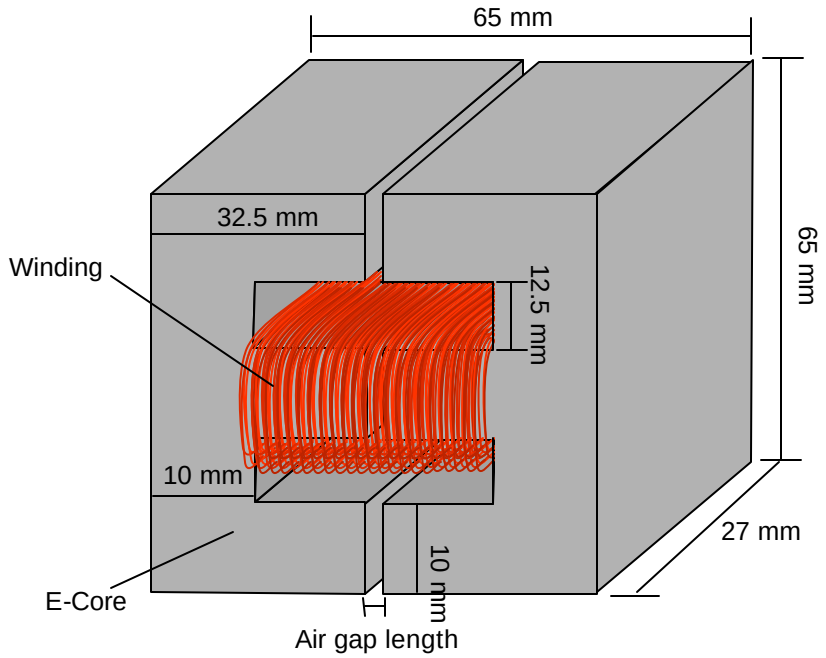

Figure 6.1. E-core and winding geometry.

The simplicity of the E-core geometry and its commercial availability provide the primary motivation for its use in this experiment. Also, the behavior of the E-core is well understood and therefore the thermal loading on the experiment can be accurately determined. The ANSYS model takes advantage of the symmetry that is inherent in the pole structure and consists of one-fourth of the entire core/winding apparatus, as shown in Fig. 6.2. The symmetry in the E-core geometry is represented in the finite element model by adiabatic surfaces. The winding thickness used in the model is dependant on the number of turns of wire and on the tightness of the winding.

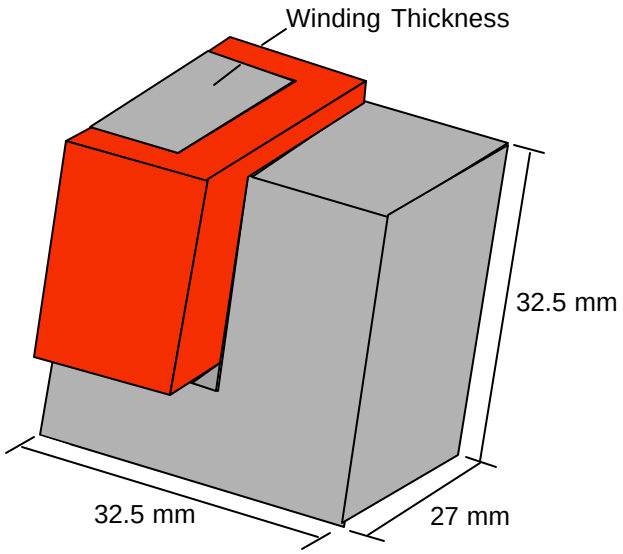

Figure 6.2. One-fourth of core/winding geometry, as modeled in ANSYS.

6.1.1.1 Material Properties

Both E-cores are made of 3C85 soft ferrite and manufactured by Philips [6.1]. The ferrites are ceramic, homogenous materials composted of various oxides with iron oxide as their main constituent. The material has a high resistivity and good magnetic properties,

which makes it an excellent core material. Also, ferrite has very low losses in conjunction with a high permeability and is very stable thermally.

The winding is constructed using 24 AWG heavy insulated copper magnet wire with a nominal diameter of 0.56 mm that is manufactured by Fay Electric Wire Corp [6.2]. The wire is insulated with a 25 μm polyimide coating based on the NEMA Magnet Wire Standard [6.3]. The material properties of the winding are calculated using the equivalent thermal conductivity method presented in Section 2.2.2. A packing factor of 0.57 is used for the winding and was achievable through hand-winding, calculated by measuring the number of turns of wire and the cross-sectional area of the winding. Table 6.1 summarizes the properties of the materials used in the E-core model.

Table 6.1. Material properties used in E-core model.

Component	Material	Density (kg/m^3)	Thermal Conductivity (W/m-K)	Specific Heat (J/kg-K)
E-Core	Soft Ferrite [6.1]	4700	4.19	1047
Coil	Copper	8900	393.5	385
	Polyamide	1350	0.37	-
	Air	0.87	0.03	-
	Equivalent	4340	0.23	-

6.1.1.2 Thermal Loads

As with the motor pole model, there are core losses and winding losses in the E-core and these thermal loads result in a temperature rise within the system. The simplicity of the geometry of the E-core configuration makes the calculation of these losses much simpler than it would be for the more complex shaped SMC motor poles. The core loss (*Core Loss* in W) is calculated using Eq. 6-1 [6.4]:

$$Core\ Loss = a\ f^{c}\ B^{d} \tag{6-1}$$

where f is the frequency in kHz, B is the saturation flux density in kGauss, and a, c, and d are constants based on the type of material. The E-core used in the experiment is composed of f-type material and therefore a = 0.790, c = 1.06, and d = 2.85. The saturation flux density is calculated using Eq. 6-3 [6.5]:

$$B = \frac{V\,t}{N\,A_c} \tag{6-2}$$

where V is the applied voltage in the winding in Volts, t is the time that the voltage is applied in seconds, N is the number of turns in the winding, and A_c is the cross-sectional area of the conductor in m^2. Table 6.2 shows the calculated core loss for each of the four input current values. As expected, these loss values are very low due to the 60 Hz operation frequency. Therefore, the core loss is assumed to be negligible in the ANSYS model.

Table 6.2. Calculated core loss.

Input Current (A)	**Core Loss (W)**
0.25	$3.53e^{-5}$
0.5	$2.55e^{-4}$
1.0	$1.84e^{-3}$
1.5	$5.83e^{-3}$

The winding loss is calculated using Eq. 6-2 [6.6]:

$$Winding\ Loss = 0.022\,L_w\left(\frac{I}{d_c}\right)^2 \tag{6-3}$$

where L_w is the length of the winding, I is the rms current of the winding, and d_c is the diameter of the conductor.

6.1.2 Air Flow Model

Although the geometry of the E-core configuration is less complex than that of the motor-pole model, the geometry of the internal air passages that are formed by the E-cores, the windings, and the test section housing is still complex and therefore warrants a three-dimensional CFD model as opposed to a simpler flow model based on correlations. These air passages provide the primary means of cooling for all of the components and therefore the behavior of the flow must be adequately considered. Figure 6.3 shows the mesh used for the 3-D CFD model of the air passages.

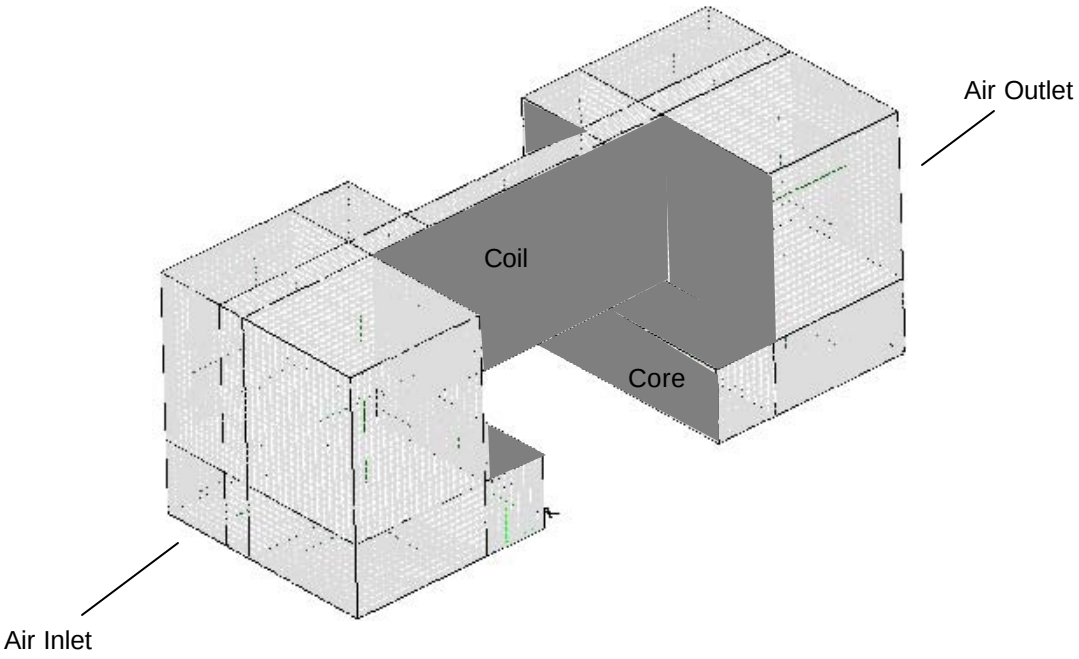

Figure 6.3. 3-D model of internal air passage through the E-core.

Three different boundary conditions are applied to the 3-D model. The solid wall surfaces on which the fluid comes into contact with the E-core and coil are modeled as a constant wall temperature. The air inlet side of the model has a constant inlet velocity and constant inlet temperature. The air outlet surface has an outlet pressure boundary. The air

properties used in the model can be found in Table 3.1. Once the mesh is complete, the same turbulent modeling approach that was described in Section 3.1.1 is used to determine the air velocities within the passage. The heat transfer coefficients on all of the E-core and coil surfaces and the pressure drop through the passage were determined for the inlet velocity measured for the experiment. The heat transfer coefficients are applied to the E-core model.

As described in Chapter 5, the heat transfer coefficients provide only part of the boundary condition for the model. The local air temperatures exposed to the surfaces within the air passages must also be taken into account. This is done by dividing the air passage in several sections and using the iterative energy balance process described in Section 5.2.2.

6.2 Experiment

This section describes the experimental setup and procedure that was used to verify the E-core finite element modeling results.

6.2.1 Experimental Setup and Procedure

Figure 6.4 is a photograph of the overall experimental setup, while Fig. 6.5 and Fig. 6.6 show a schematic of the experiment test section chamber.

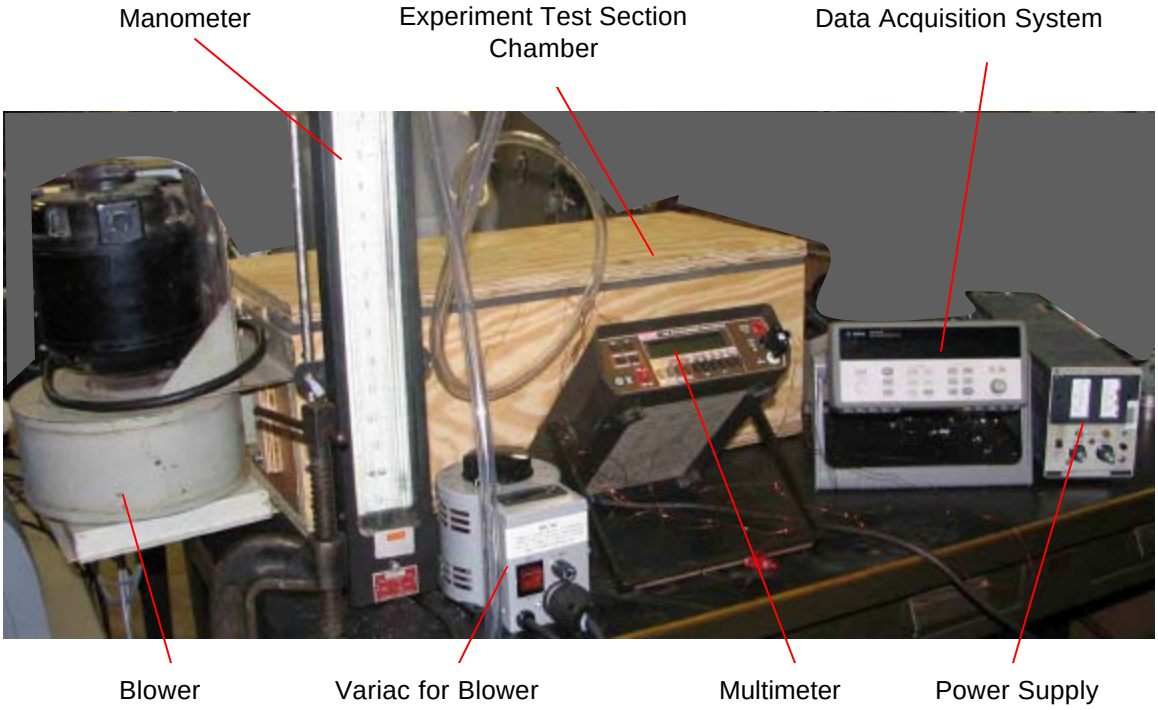

Figure 6.4. Overview of experiment setup.

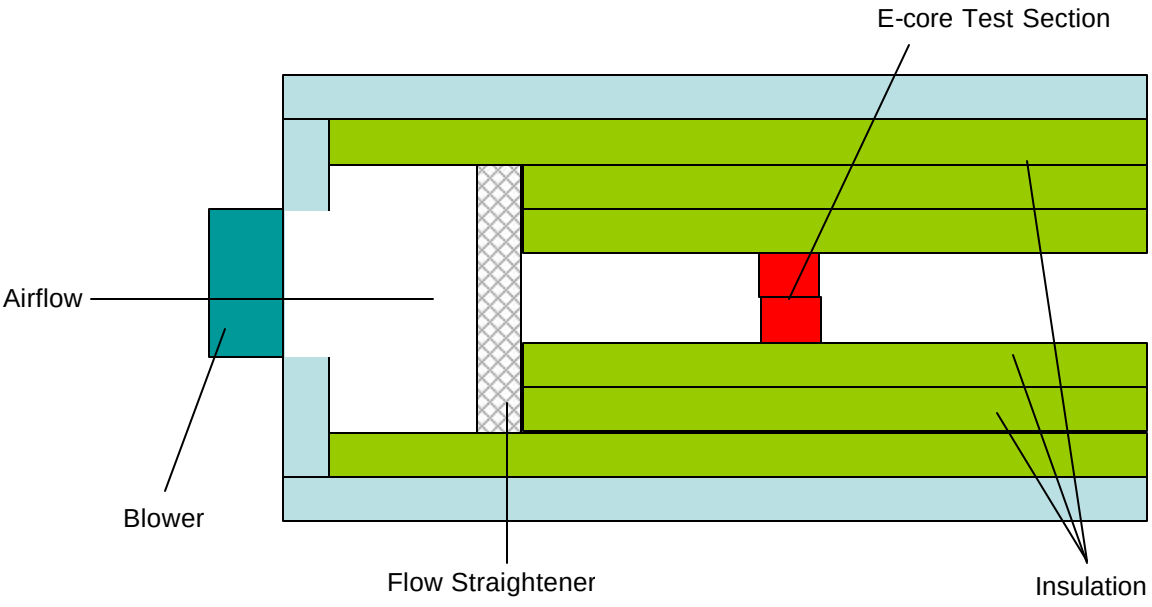

Figure 6.5. Experimental test section chamber setup - top view.

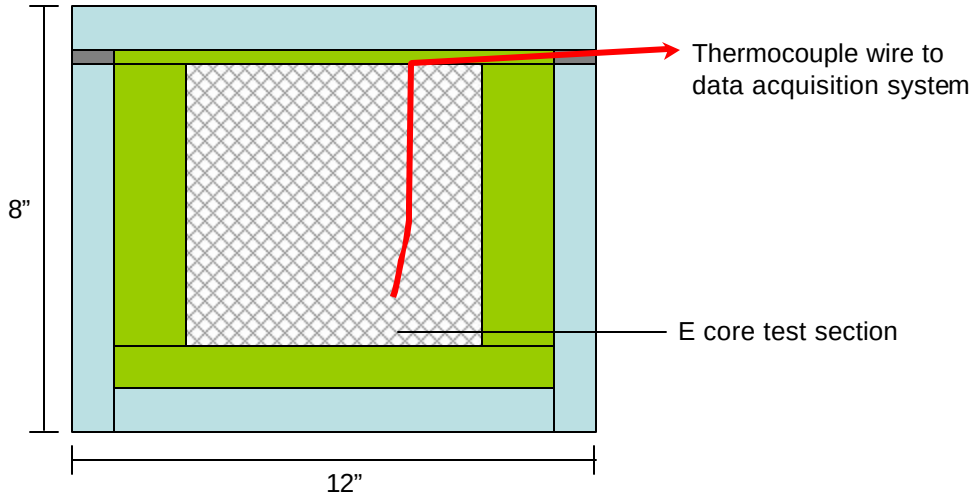

Figure 6.6. Experimental test section chamber setup – cross-sectional view at inlet to flow straightener.

The setup is fabricated from plywood and the top section is removable to allow the internal details to be adjusted. Air at ambient temperature is forced into the enclosure by a Leland centrifugal fan. The air passes through a flow straightener that is constructed of perforated stainless steel sheets with a 6.35 mm hexagonal mesh as shown in Fig. 6.7. Styrofoam is used to insulate the test section and also constrict the airflow down to the cross-sectional area of the 65.2 mm × 65.2 mm inlet face of the E-core test section. The test section, which is shown in Fig. 6.8, is two E-cores separated by a 3.3 mm thick piece of G10, an insulating polymer. The E-cores are hand wound with 400 turns apiece; the magnet wire used for the winding is described in Section 6.1.1.1. The inlet air velocity to the test section is measured at the locations around the duct cross-section that are shown in Fig. 6.9 and at a single axial location that is 8 hydraulic diameters of the flow straightener (5.3 cm) downstream from the flow straightener and 1 cm upstream of the test section using a Solomat MPM 500e [6.7] anemometer with an accuracy of ±0.15 m/s based on the manufacturer’s specification.

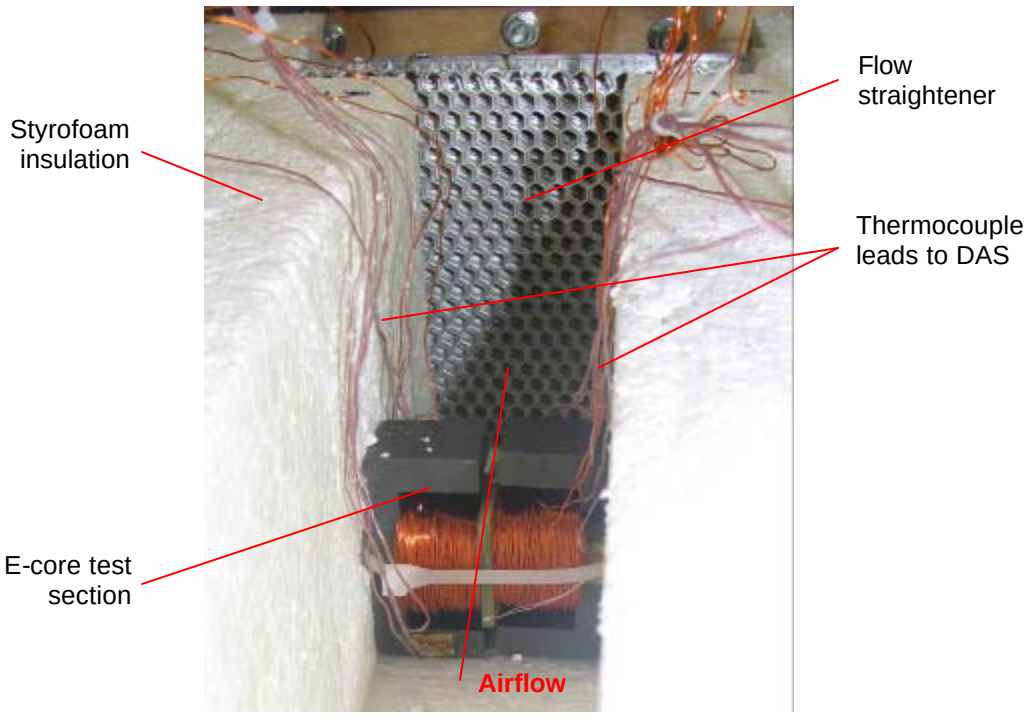

Figure 6.7. Test section placed inside experimental chamber.

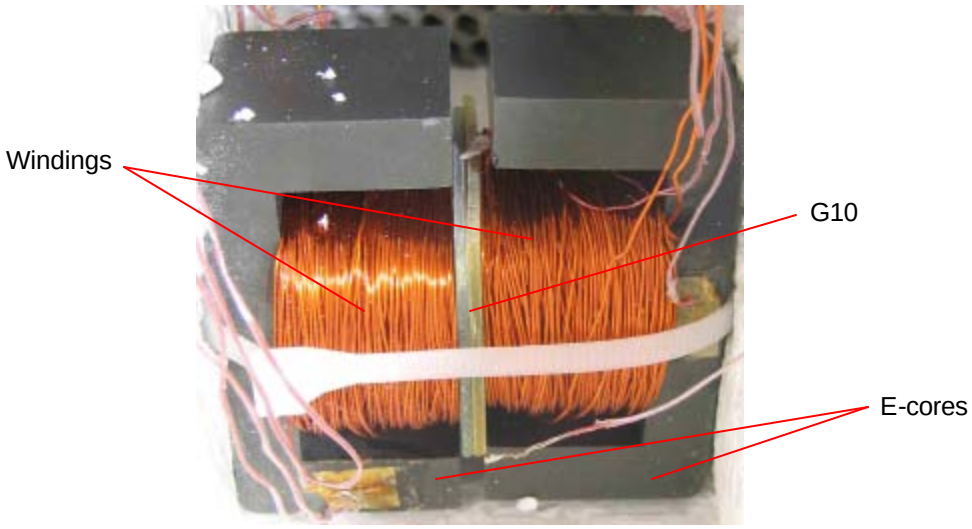

Figure 6.8. E-core test section.

The velocity profiles of the airflow in the channel are shown in Fig. 6.10 through Fig. 6.12. An average velocity of at the inlet to the test section is calculated by weighting all

measured velocity values equally and averaging them. The pressure drop across the test section is measured using a u-tube manometer with an accuracy ±0.1 inches H_2O.

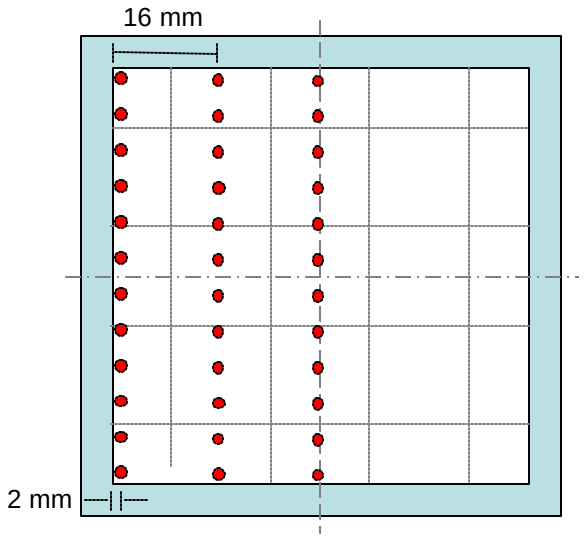

Figure 6.9. Velocity test locations.

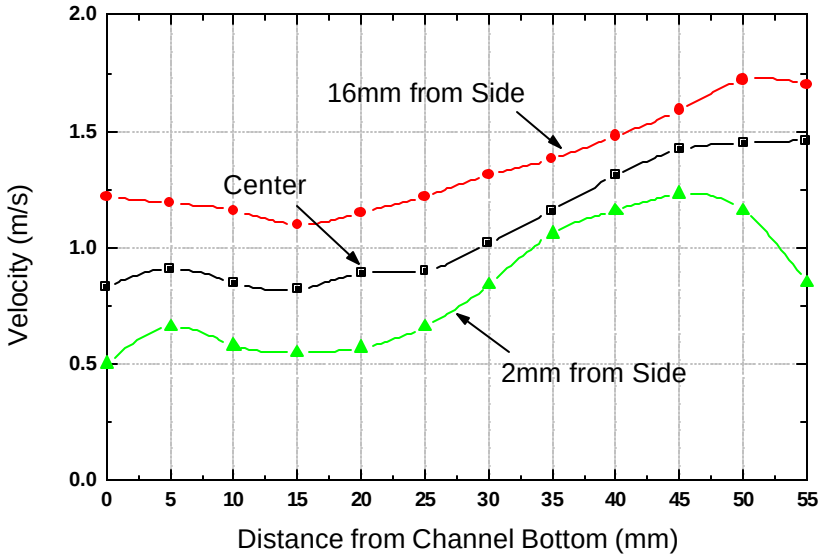

Figure 6.10. Air velocity distribution in channel for 1.1 m/s inlet airflow.

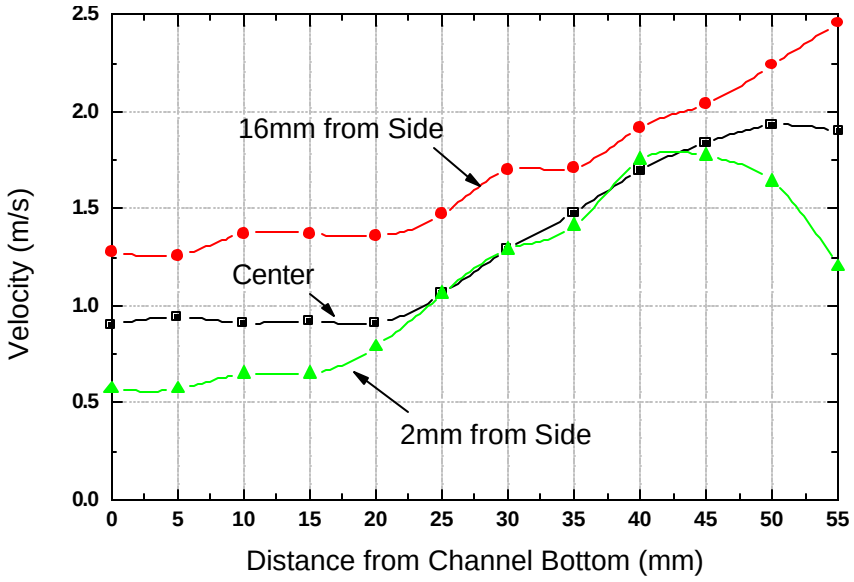

Figure 6.11. Air velocity distribution in channel for 1.4 m/s inlet airflow.

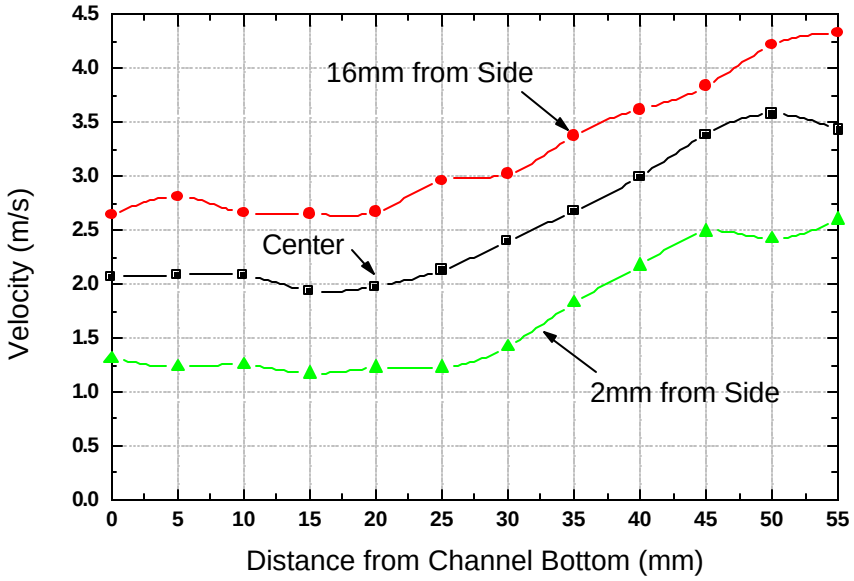

Figure 6.12. Air velocity distribution in channel for 2.5 m/s inlet airflow.

The temperature of the test section is measured using 12 thermocouples located at various positions on the ferrite core and embedded within the windings, as shown in Fig. 6.13. Two additional thermocouples are located in the inlet (#22) and outlet (#23) air streams to monitor the rise in air temperature across the core. Another thermocouple (#24) is

affixed to the magnet wire at the end of the winding in order to monitor against wire overheating. LabVIEW software [6.88] coupled with a data acquisition system is used to record the temperature data for the system.

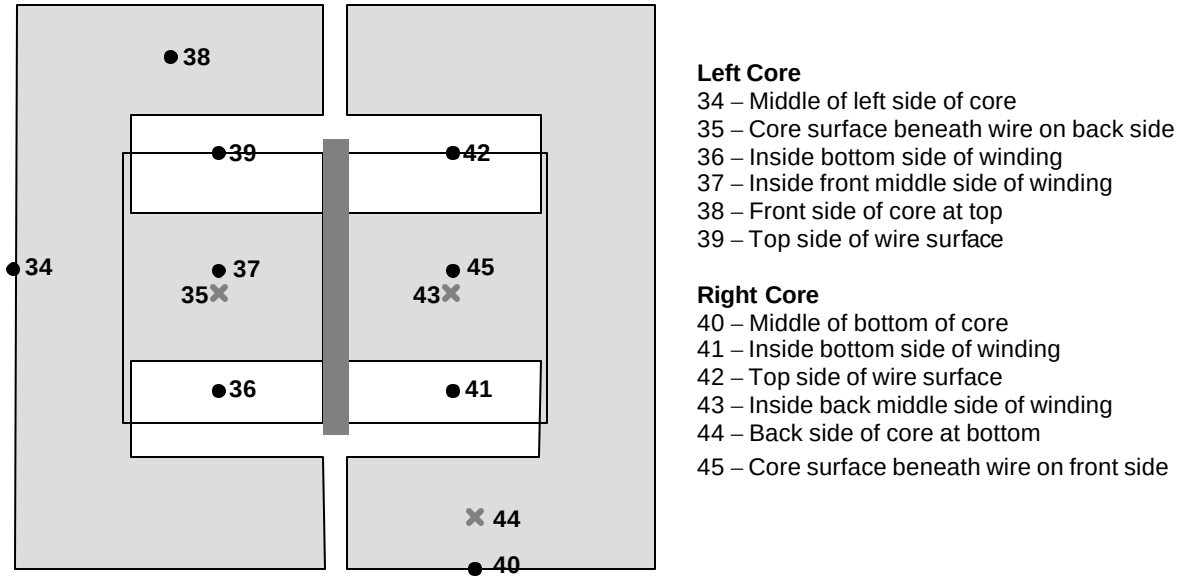

Figure 6.13. Location of thermocouples on winding and core.

Temperature data are collected at four different input current values: 0.25 A, 0.5 A, 1.0 A, and 1.5 A and three different fan speeds which correspond to inlet air velocities of 1.1 m/s, 1.4 m/s, and 2.5 m/s. Figure 6.14 shows the temperatures recorded in the experiment as a function of time for an input current of 1.0 A at an air velocity of 2.5 m/s. In order to allow the system to reach steady state, the experiment is run for approximately 2000 s. Once data are collected, the steady state temperature at each location is calculated by averaging the temperatures of the associated thermocouple over the last 1000 s of experimentation. The steady-state temperatures for I = 1.0 A and v = 2.5 m/s are shown in Fig. 6.15.

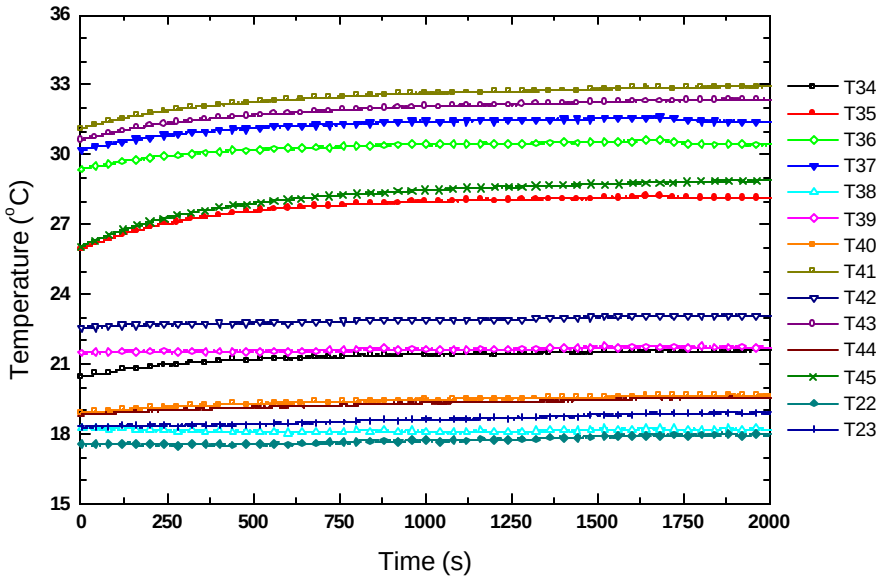

Figure 6.14. Experimental transient temperatures for all thermocouples at I = 1.0 A and v = 2.5 m/s.

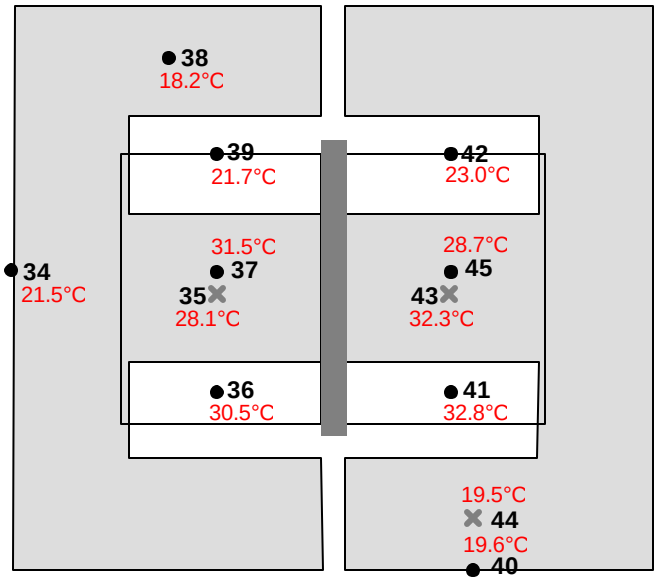

Left Core
34 – Middle of left side of core
35 – Core surface beneath wire on back side
36 – Inside bottom side of winding
37 – Inside front middle side of winding
38 – Front side of core at top
39 – Top side of wire surface

Right Core
40 – Middle of bottom of core
41 – Inside bottom side of winding
42 – Top side of wire surface
43 – Inside back middle side of winding
44 – Back side of core at bottom
45 – Core surface beneath wire on front side

Figure 6.15. Steady-state temperatures for all thermocouples at I = 1.0 A and v = 2.5 m/s.

For each input current value and air velocity, the temperatures at all thermocouples were normalized based on the inlet air temperature measured by Thermocouple 22. The

temperature data summarized in Table 6.3 represents the increase in temperature from the inlet air temperature as measured by each thermocouple.

Table 6.3. Thermocouple temperature data – increase in temperature from inlet air (°C).

Location	**Temperatures**											
	***v* = 1.1 m/s**				***v* = 1.4 m/s**				***v* = 2.5 m/s**			
	0.25 A	**0.5 A**	**1.0 A**	**1.5 A**	**0.25 A**	**0.5 A**	**1.0 A**	**1.5 A**	**0.25 A**	**0.5 A**	**1.0 A**	**1.5 A**
34	0.7	2.2	7.8	17.5	0.8	1.6	5.5	13.0	0.8	1.1	3.7	7.8
35	1.1	4.2	15.9	36.8	1.1	3.5	13.2	31.1	1.1	2.7	10.3	22.9
36	1.4	5.2	20.3	45.9	1.4	4.3	16.6	38.8	1.3	3.3	12.6	28.1
37	1.3	5.2	20.8	47.2	1.3	4.4	17.4	40.5	1.2	3.4	13.6	30.3
38	0.2	0.2	0.3	0.5	0.2	0.1	0.2	0.3	0.4	0.2	0.3	0.3
39	0.6	2.3	9.4	21.2	0.6	1.6	6.3	15.1	0.5	1.0	3.8	8.6
40	0.2	1.2	4.4	10.6	0.2	0.8	3.0	7.4	0.3	0.4	1.7	3.9
41	1.3	5.6	23.0	54.7	1.3	4.7	19.3	47.5	1.1	3.6	15.0	36.0
42	0.7	2.9	12.0	27.8	0.7	2.1	8.5	21.0	0.5	1.3	5.1	12.3
43	1.3	5.5	22.5	53.4	1.3	4.5	18.7	46.1	1.0	3.5	14.4	34.6
44	0.2	1.1	4.2	10.0	0.2	0.7	2.8	6.9	0.3	0.4	1.6	3.7
45	0.9	4.3	17.5	41.8	0.9	3.5	14.5	35.7	0.8	2.6	10.9	26.2
22	0	0	0	0	0	0	0	0	0	0	0	0
23	0.1	0.5	2.1	4.8	0.1	0.4	1.5	3.6	0.0	0.2	0.9	2.1
24	0	0.2	0.8	1.8	0	0.1	0.5	1.2	0	0.1	0.2	0.6

6.3 Comparison of Experiment and Model

The next step in the experimental verification process is to compare the model predictions with the experiment using the measured air inlet velocity and inlet temperature together with the power losses that are predicted for the given input current.

6.3.1 Heat Transfer Coefficients

The average air velocity measured for the experiment is used as the uniform inlet velocity in the FLUENT air flow model described in Section 6.1.2. The heat transfer coefficients on all outer surfaces on the core and winding are determined and summarized in in Table 6.4.

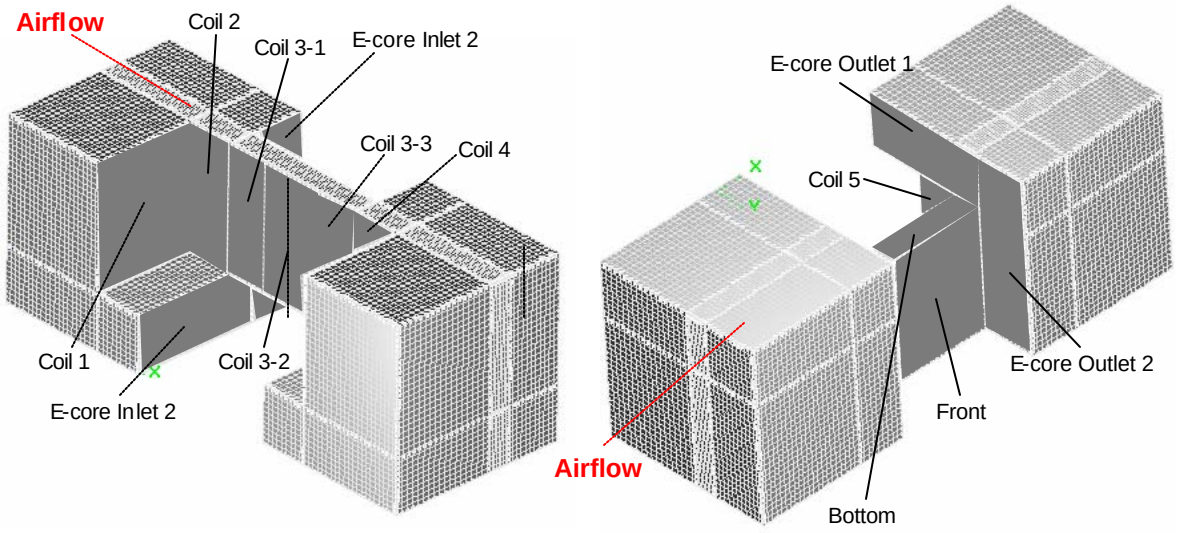

Figure 6.16. Heat transfer coefficient surfaces.

Table 6.4. Heat transfer coefficients (W/m^2-K) for E-core and winding surfaces.

		Heat Transfer Coefficient (W/m^2-K)		
		***v* = 1.1 m/s**	***v* = 1.4 m/s**	***v* = 2.5 m/s**
Coil	**1**	47.1	53.70	74.25
	2	40.7	43.98	56.49
	3-1	112.28	129.08	190.93
	3-2	128.03	154.51	242.30
	3-3	95.25	115.68	184.72
	4	35.54	37.20	42.57
	5	40.61	42.20	51.22
E-core Inlet	**1**	40.99	44.72	61.70
	2	68.86	80.62	120.20
E-core Outlet	**1**	33.77	35.70	40.39
	2	34.79	37.63	47.54
Front		115.67	138.92	218.31
Bottom		85.14	103.74	167.16

6.3.2 Results

6.3.2.1 Predicted Temperature Distributions

Figures 6.17 through 6.19 show the predicted temperature distributions for the three input air velocities at an input current of 1.5 A. The highest temperatures are experienced at the center of the concentrated winding, with the maximum temperatures found at the air outlet side. The numbers on Fig. 17, 18 and 19 correspond to the locations of the thermocouples used in the experiment.

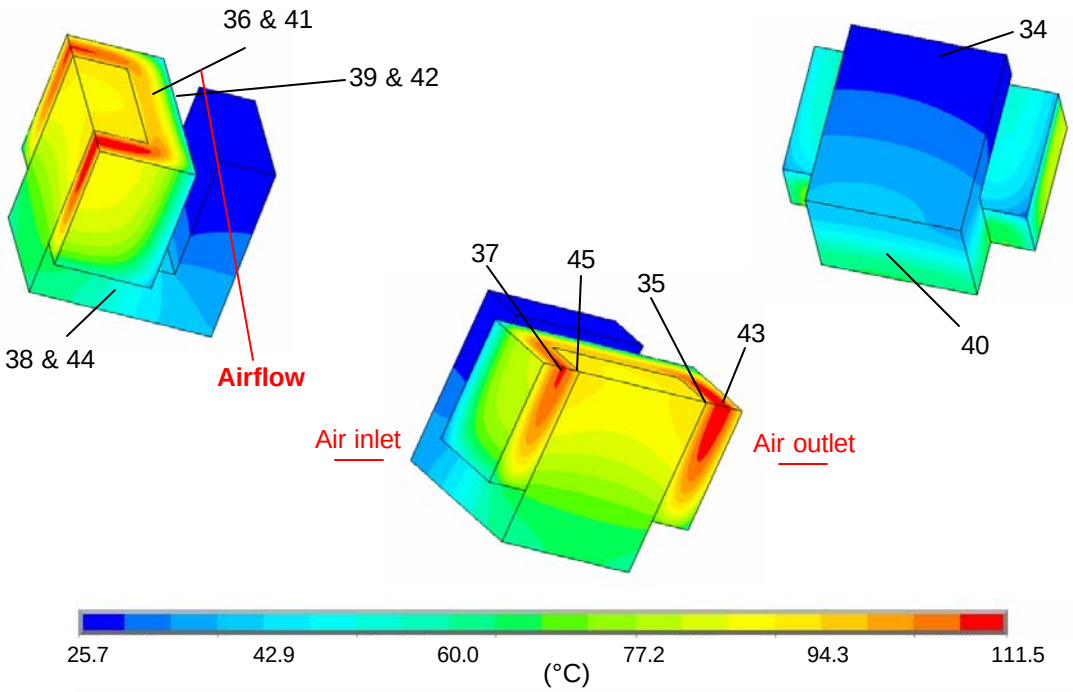

Figure 6.17. Model temperature distribution for I = 1.5 A at v = 1.1 m/s.

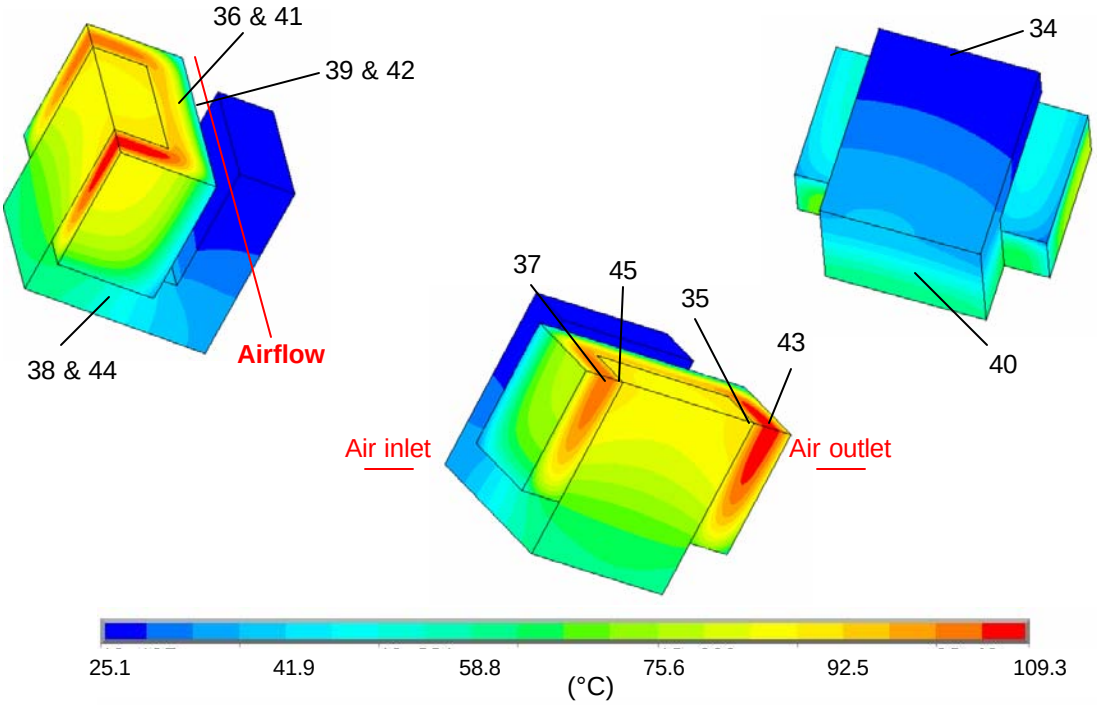

Figure 6.18. Model temperature distribution for I = 1.5 A at v = 1.4 m/s.

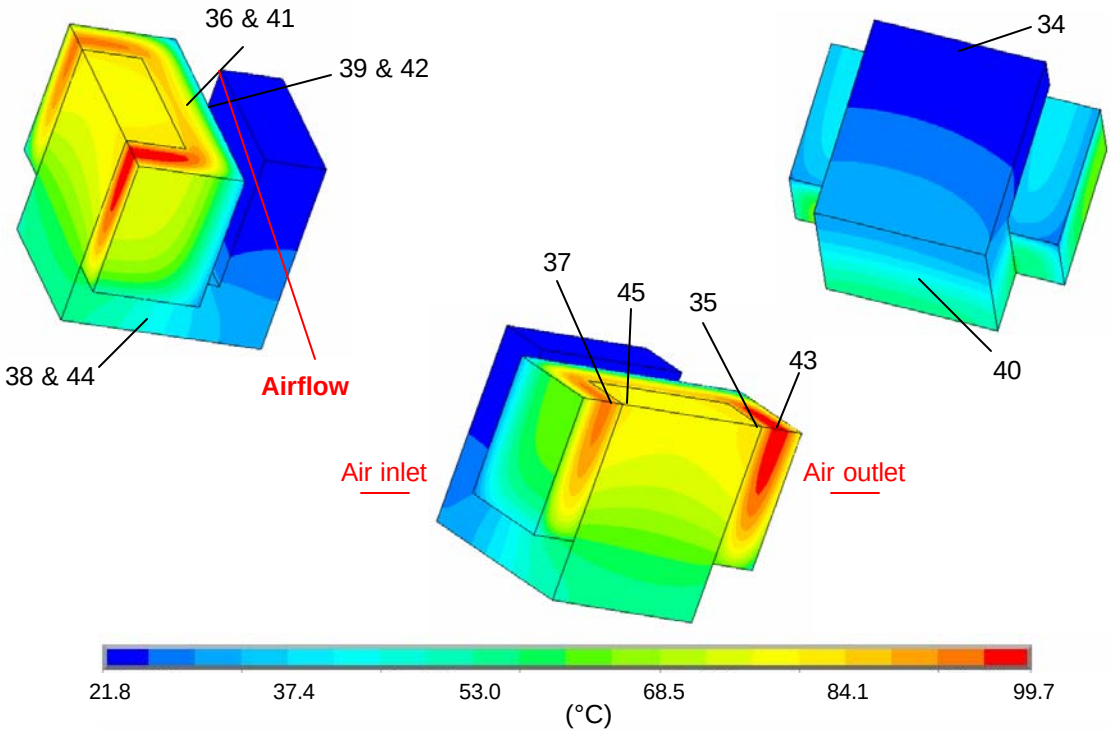

Figure 6.19. Model temperature distribution for I = 1.5 A at v = 2.5 m/s.

6.3.2.2 Experiment and Model Temperature Comparison

A comparison of the model and experiment temperature results as a function of the input current and inlet velocity is shown in Fig. 6.20 through Fig. 6.25 for three selected thermocouple locations of interest: inside the winding (#36), on the winding surface (#39), and on the core surface beneath the winding (#35). An explanation of the error associated with the error bars and model upper and lower limits that is presented in these figures follows in the next section. Overall, the model is capable of accurately predicting the temperature distribution within the E-core; all of the experimental measurements fall within the range of uncertainty related to the experiment measurements and the model predictions. The greatest discrepancies between the model and experimental temperatures exist at the locations within the windings, and may be due to poor thermal contact between the winding and the thermocouple or a systematic underestimate of the equivalent thermal conductivity of the winding.

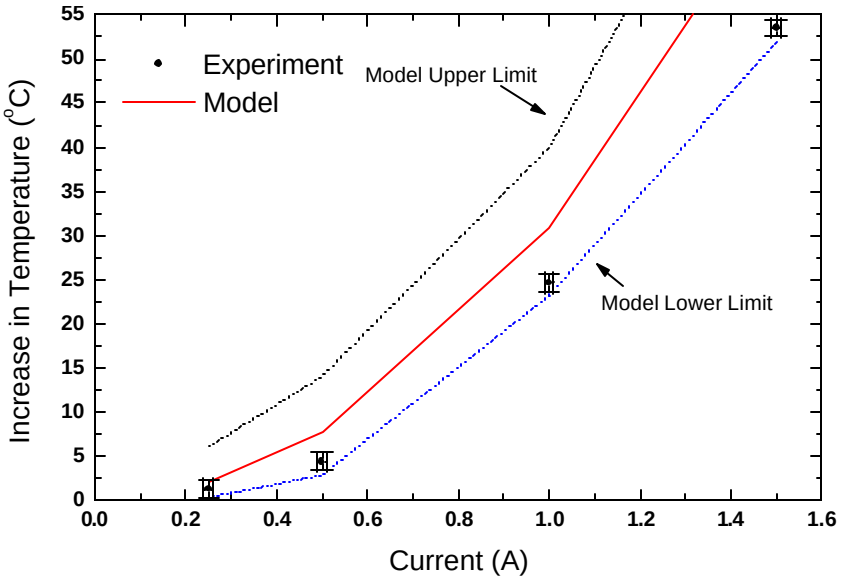

Figure 6.20. Measured and predicted increase in temperature at thermocouple 36 which is located on the inside, bottom side of the windings as a function of input current values at v = 1.4 m/s.

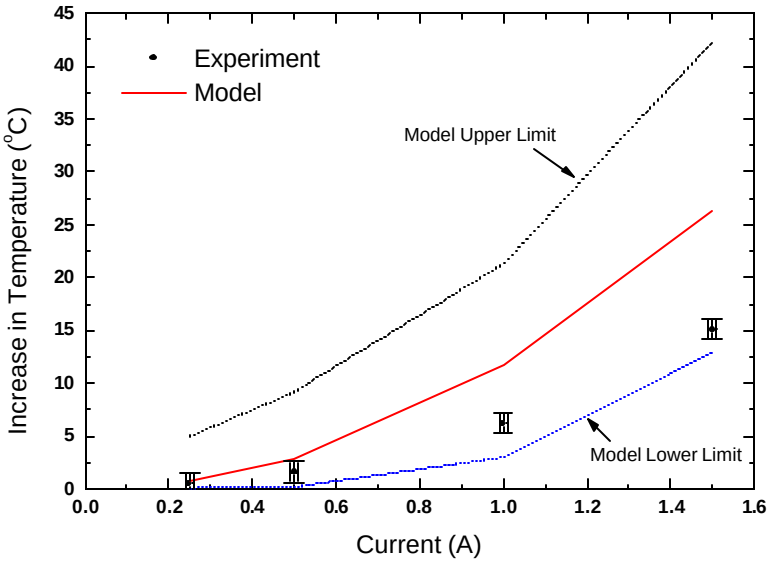

Figure 6.21. Measured and predicted increase in temperature at thermocouple 39 which is located on the top side of the wire surface as a function of input current values at v = 1.4 m/s.

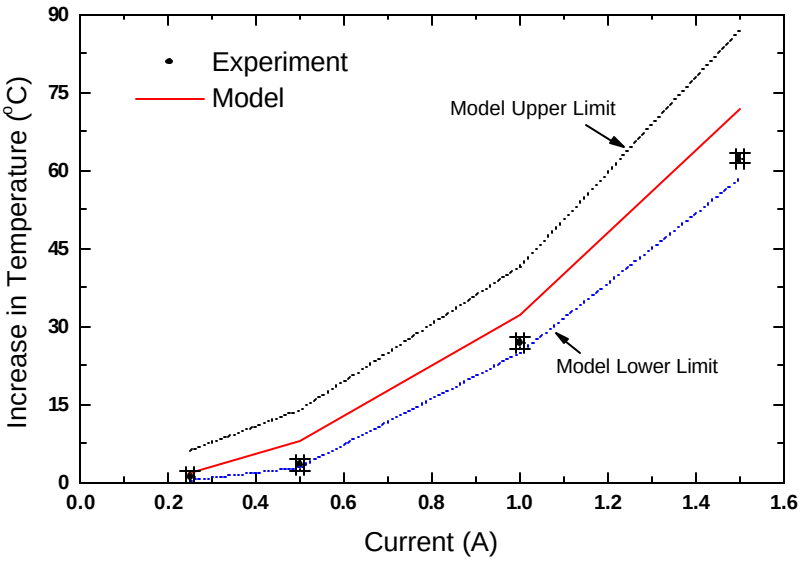

Figure 6.22. Measured and predicted increase in temperature at thermocouple 35 which is located on the core surface beneath the wire on the back side of the E-core as a function of input current values at v = 1.4 m/s.

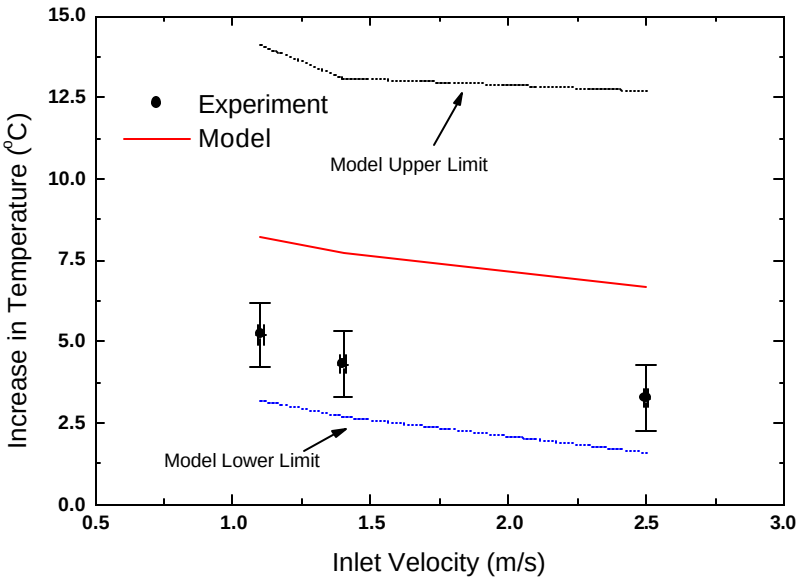

Figure 6.23. Measured and predicted increase in temperature at thermocouple 36 as a function of inlet air velocity at I = 0.5 A.

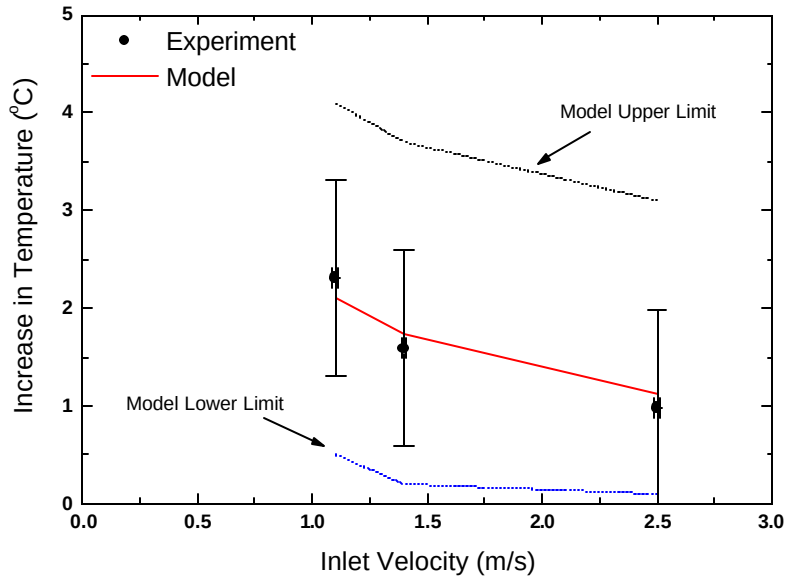

Figure 6.24. Measured and predicted increase in temperature at thermocouple 39 as a function of inlet air velocity at I = 0.5 A.

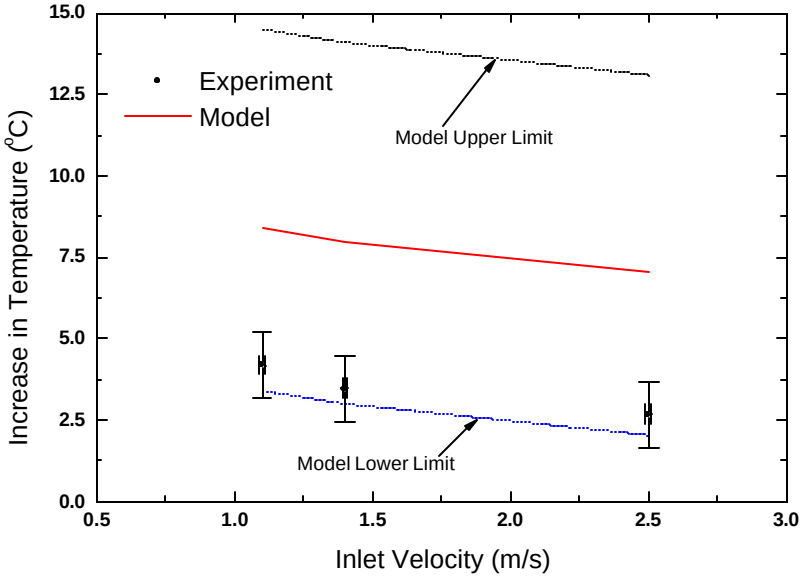

Figure 6.25. Measured and predicted increase in temperature at thermocouple 35 as a function of inlet air velocity at I = 0.5 A.

6.4 Uncertainty

Four major contributors to uncertainty were considered in the analysis of the model prediction and experimental data: surface heat transfer coefficient, wire equivalent thermal

conductivity, input current to the experiment, and measurement error in the thermocouples. This section describes the derivation and ultimate effect that each of these possible sources of error had on the results of both the model and experiment.

6.4.1 Thermocouples

The thermocouples are attached to the E-core and windings using GE varnish in order to provide a conductive connection between the thermocouple and contact surface. However, it is still possible that there are errors in the thermocouple readings due to inconsistent contact between the thermocouple and contact surface, irregularities in the varnish, and also in the manufacture of the thermocouple itself. Due to the small diameter of the wire and the extremely small volume that the air occupies between the wires, it is assumed that the error caused by the thermocouple location is relatively small. Therefore, the main contributor to the error is in the thermocouples themselves and a ±1°C uncertainty is incorporated for all experimental temperature readings.

6.4.2 Input Current

During any given experimental trial, the temperature increase in the windings created fluctuations in the resistivity of the wire and resulted in a non-steady input current to the windings. While efforts were made to maintain the desired input current, it must be assumed that the possible error in the current value played some role in creating error in the data. Therefore, a ±0.005 A uncertainty is incorporated in the results.

6.4.3 Heat Transfer Coefficient

As described in Section 6.1.2, the heat transfer coefficients applied to the surfaces of the E-core model are based on the inlet air velocity in the channel. To account for possible error in velocity measurement, a ±0.15 m/s measurement error on the average inlet air speed is accounted for in the FLUENT air flow model. The heat transfer coefficients calculated from the FLUENT model are used as bounds in the ANSYS E-core model. Table 6.5 shows the heat transfer coefficient values for an inlet velocity of 1.4 m/s.

Table 6.5. Heat transfer coefficients corresponding to a +/- 0.15 m/s measurement error in average inlet velocity.

		Heat Transfer Coefficient (W/m^2-K)		
		***v* = 1.25 m/s**	***v* = 1.4 m/s**	***v* = 1.55 m/s**
Coil	**1**	50.72	53.70	56.66
	2	42.34	43.98	45.62
	3-1	120.73	129.08	137.88
	3-2	141.32	154.51	167.18
	3-3	105.51	115.68	125.57
	4	36.67	37.20	37.92
	5	41.42	42.20	42.97
E-core Inlet	**1**	42.86	44.72	46.74
	2	74.64	80.62	86.40
E-core Outlet	**1**	34.74	35.70	34.48
	2	36.21	37.63	38.88
Front		127.31	138.92	150.24
Bottom		94.44	103.74	112.74

6.4.4 Wire Equivalent Thermal Conductivity

The thermal conductivity of the winding plays an integral role in determining the temperature distribution within the model and particularly affects the temperature of the winding. The calculation of the thermal conductivity relies on accurate measurements of the wire length and diameter as well as knowledge of the insulation thickness and overall

packing factor. Since only the outer wire diameter was measured for the experiment, the internal copper wire and insulation dimensions used in calculations were based on the published NEMA magnet wire standards. There may be some difference between these published values and the actual wire used in the experiment. Another possible source of error exists with respect to the exact number of winding turns and in the measurement of the winding cross-sectional area for the packing factor calculation. To account for these possible errors, a ±1 mm measurement error is assumed for measuring the wire cross section and a 5 turn error is assumed for the total number of turns, resulting in a lower and upper bounds of 0.47 and 0.68, respectively, for the equivalent packing factor.

6.5 Sensitivity Analysis

A sensitivity analysis was performed in order to determine which input variables had the greatest effect on the temperature distribution predicted for the E-core. Table 6.6 provides a summary of the average percent change in temperature at two thermocouple locations, at the core surface (#45) and at the coil center (#37), when one of the parameters discussed above (heat transfer coefficient, wire equivalent thermal conductivity, and input current) is varied with everything else held constant. Table 6.7 takes the same data and shows the effect of the change in variable as a non-dimensional constant based on the ratio of the percent change in temperature from the nominal case to the percent change in the given key variable.

Table 6.6. Average percent change for thermocouples 37 and 45 from nominal temperature data for I = 1.5 A and v = 1.4 m/s.

	Thermocouple 37	**Thermocouple 45**
Heat Transfer Coefficient (+10%)	0.32%	2.28%
Heat Transfer Coefficient (-10%)	-0.23%	-2.63%
Equivalent Wire Thermal Conductivity (+10%)	0.26%	1.38%
Equivalent Wire Thermal Conductivity (-10%)	-0.18%	-1.07%
Current (+10%)	-15.22%	-14.68%
Current (-10%)	17.72%	17.09%

Table 6.7. Ratio of average percent change in temperature to percent change in variable for I = 1.5 A and v = 1.4 m/s.

	Thermocouple 37	**Thermocouple 45**
Heat Transfer Coefficient (+10%)	0.03	0.28
Heat Transfer Coefficient (-10%)	-0.02	-0.46
Equivalent Wire Thermal Conductivity (+10%)	0.03	0.12
Equivalent Wire Thermal Conductivity (-10%)	-0.02	-0.19
Current (+10%)	-1.52	-1.47
Current (-10%)	1.77	1.71

Based on Table 6.6 and Table 6.7, the input current has the greatest effect on the temperatures in the model. Any change to either the heat transfer coefficients or the equivalent thermal conductivity in the winding affects the temperatures by a smaller amount.

6.6 References

[6.1] Philips Components, Magnetic Products Division, Saugerties, NY, www.philips.com, Phone: (914) 246-2811, Fax: (914) 246-0487.

[6.2] Fay Electric Wire Corp., 752 North Larch Ave., Elmhurst, IL 60126, www.faywire.com, Phone: (800) 245-9473, Fax: (630) 530-7536.

[6.3] National Electrical Manufacturers Association Dimensions for Bare and Film Insulated Round Magnet Wire, MW 1000-2003 Part 1, Washington D.C., 2003.

[6.4] Magnetics – Ferrite Cores, Powder Cores, Tap and Custom Cores, P.O. Box 11422, Pittsburgh, PA 15238, www.mag-inc.com, Phone: (412) 696-1333, Fax: (412) 696-0333.

[6.5] Billings, K., Switchmode Power Supply Handbook – 2nd Ed., McGraw-Hill, Columbus, OH, 1999.

[6.6] Transformers, Inductors, and Coil Design Guide, Acetown Electrocoil Inc., P.O. Box 248 2414, Highview St., Spring Grove, IL 60081, www.acetown.com, Phone: (815) 675-6641, Fax: (815) 675-2050.

[6.7] Solomat, The Waterside Building, 26 Pearl Street, Norwalk, CT 06850, Phone: (203) 849-3111, Fax: (203) 847-9320.

[6.8] LabVIEW 7.1, National Instruments Corporation, 11500 N. Mopac Expwy, Austin, TX 78759, www.ni.com, Phone: (888) 280-7645, Fax: (512) 683-8411.

7 Summary and Conclusions

Conventional induction-type electric motors are manufactured using thin laminations in order to improve the overall efficiency of the motor. Although efforts have been taken to improve this efficiency, there is limited opportunity for further advancements that do not also result in increased production costs or degraded mechanical properties and therefore reduced reliability. Laminated machines have other drawbacks as well, including geometry and size constraints and reliability issues due to the long cable interconnections that run between the motor and the power supply.

Faced with the limitations of the current laminated machines, the research in this thesis explores the feasibility of a new electric motor configuration scheme: a modular permanent magnet machine. This modular, integrated motor/controller is constructed of identical, individual stator poles, that are each closely integrated with their own power electronics module. The integration between the motor and power supply creates a more efficient machine and eliminates the reliability issues currently encountered by cable interconnections. This research specifically focuses on the thermal feasibility of this motor/controller design as the maximum safe temperature in the power electronics is far less that temperatures typical during normal motor operation.

Individual, finite element component-level models are constructed to accurately model the thermal behavior of the stator piece, air flow passages, and the power electronics module. Once constructed, these component models are subsequently integrated in order to obtain a system level model of the motor. The models are developed in so that they can be integrated in various ways depending on the cooling system configuration.

The overall goal of this project was the development of a modeling methodology capable of accurately predicting the thermal response of the motor and IPEM components in a given cooling configuration. The accuracy of the modeling technique would then be verified through experiment. Unfortunately, we were not able to obtain the exact motor poles to match those modeled in the timeframe of the project. Instead, it was decided to develop a new set of models using the same tools and methodology that was used for the motor/controller design. These models predict the thermal response of a wound E-type ferrite core transformer rather than the more complex stator poles. The comparison of the measured and predicted behavior of these poles provides a measure of accuracy of the thermal models.

Both the effects of changing the input current and altering the inlet velocity were studied in the comparison of the model and experimental temperature results. Overall, the E-core model does an excellent job of predicting the thermal response of the core and winding when current is applied, with all experimental temperature results falling within the upper and lower bounds of the model results. For all cases the models over predict the temperature rise within the E-core test section, with this discrepancy increasing significantly as the input current increases.

The future work on this project is twofold. More work must be done to study the cause of the temperature discrepancy between the model and experiment. Additional thermocouples must be added at the locations of interest in order to get a better idea of how accurately the models predict the increase in temperature at specific locations. Other instruments, such as an infrared camera might also be used to get a better picture of the

overall temperature distribution. Placing additional thermocouples in the inlet and outlet airstreams will allow for a more cohesive study of the energy balance across the test section. The second stage future work involves the procurement of the actual motor poles modeled in the motor/controller design and the subsequent experimental validation of the motor models.

Appendix A

ANSYS MOTOR MODEL CODE

```
/FILNAME,Trial1,1
/config,nproc,2
/PREP7
/TITLE, Steady-State Thermal Analysis of
an Elec. Motor
/SHOW,
*AFUN, DEG  !Use degrees for trigonometry
functions

!======= I-PHYSICAL PROPERTIES==========
!Material (1) First Pole Core Back,
Powdered Iron
MP,DENS,1,7360/1000000000     ![kg/mm3]
MP,KXX,1,17/1000              ![W/mm-K]
MP,C,1,447                    ![J/kg-K]

!Material (2) First Pole Tooth, Iron
MP,DENS,2,7650/1000000000     ![kg/mm3]
MP,KXX,2,42/1000              ![W/mm-K]
MP,KYY,2,42/1000
MP,KZZ,2,3.1/1000             ![W/mm-K]
MP,C,2,447                    ![J/kg-K]

!Material (3) First Pole Coil, Copper
MP,DENS,3,8900/1000000000     ![kg/mm3]
MP,KXX,3,1.323/1000           ![W/mm-K]
MP,C,3,385                    ![J/kg-K]

!Material (4) First Pole Casing, Aluminum
MP,DENS,4,2705/1000000000     ![kg/mm3]
MP,KXX,4,230/1000             ![W/mm-K]
MP,C,4,900                    ![J/kg-K]

!=========III-Physical Dimensions=========
theta=30/2     ![deg]

y0=0           ![mm]
y1=4.75/2      ![mm]
y_o1=4.284499  ![mm]
y_p1=6.193973  ![mm]
y_o2=22.806000 ![mm]
y_p2=23.667050 ![mm]
y2=20.33/2     ![mm]
y3=43.89/2     ![mm]
y5=y2+18.55    ![mm]
!y6=59.67/2    ![mm]
y7=y2+19.83    ![mm]
!y9=y2+21.67   ![mm]
!y10=y2+23.09  ![mm]
y11=69.88/2    ![mm]
y12=75/2       ![mm]

r1=75          ![mm]
x0=SQRT((r1*r1)-(y12*y12))+3.75
x3=84.67       ![mm]
x4=x3+26.68    ![mm]
x5=x3+33.26    ![mm]
x6=x3+34.14    ![mm]
x7=x3+38.54    ![mm]
x8=x3+39.45    ![mm]
r6=x6/cos(13.5)        ![mm]
r8=x8/cos(13.5)        ![mm]
r9=135         ![mm]
r10=137        ![mm]

y4=y5*(x4/x6)          ![mm]
y6=x4*tan(theta)       ![mm]
y9=x5*tan(theta)       ![mm]
y10=x7*tan(theta)      ![mm]

Theta10=0              ![deg]
Theta12=ASIN(y2/r1)    ![deg]
Theta13=ASIN(y3/r1)    ![deg]
Theta112=ASIN(y12/r1)  ![deg]

Theta61=ASIN(y1/r6)    ![deg]
Theta6o1=ASIN(y_o1/r6)![deg]
Theta6p1=ASIN(y_p1/r6)![deg]
Theta62=ASIN(y2/r6)    ![deg]
Theta63=ASIN(y3/r6)    ![deg]
Theta65=13.5           ![deg]

Theta81=ASIN(y1/r8)    ![deg]
Theta8o1=ASIN(y_o1/r8)![deg]
Theta8p1=ASIN(y_p1/r8)![deg]
Theta82=ASIN(y2/r8)    ![deg]
Theta83=ASIN(y3/r8)    ![deg]
Theta87=13.5   ![deg]

Theta91=ASIN(y1/r9)    ![deg]
Theta9o1=ASIN(y_o1/r9)![deg]
Theta9p1=ASIN(y_p1/r9)![deg]
Theta92=ASIN(y2/r9)    ![deg]
Theta93=ASIN(y3/r9)    ![deg]
Theta98=13.5           ![deg]
Theta911=30/2

z_o1=59.284499 ![mm]
z_p1=61.193996 ![mm]
z_o2=33.806000 ![mm]
z_p2=34.667047 ![mm]

H_S=90
H_W=63
H_w1=57.659984         ![mm]
H10=(H_S-H_w)-(y3-y2)  ![mm]
H11=H_W-H_W1
H1=H10+H11
H2=y3-y2               ![mm]
H3=H_w1-(H1+H2)        ![mm]
!H4=y3-y2              ![mm]
H4=63-(H1+H2+H3)+(y3-y2)
H5=H_s-(H1+H2+H3+H4)
!======= IV-Creating the Geometry!======
/TITLE,GEOMETRY-Creating the SINE Shaped
Body
!1-CORE BACK
!1.1 Defining Key Points for the arcs in
Cylindrical Coordinates
CSYS,1
K,100,r1,Theta10,0
K,101,r1,Theta12,0
K,102,r1,Theta13,0
K,103,r1,Theta112,0
```

```
!1.2-Defining Arcs in Cylindrical
Coordinates
L,100,101              !Line 1
L,101,102              !Line 2
L,102,103              !Line 3

!1.3-Defining Key Points for the lines in
Cartesian Coordinates
CSYS,0
K,104,x3,y0,0
K,105,x3,y2,0
K,106,x3,y3,0
K,107,x0,y12,0

!1.4-Defining Lines in Cartesian
Coordinates
L,104,105              !Line 4
L,105,106              !Line 5
L,106,107              !Line 6
L,100,104              !Line 7
L,101,105              !Line 8
L,102,106              !Line 9
L,103,107              !Line 10

!1.5-Defining the Areas to be Extruded
AL,1,7,4,8             !Area 1, web
connection
AL,2,8,5,9             !Area 2, overhang1
AL,3,9,6,10            !Area 3, overhang2

!=============Geo-TUBE BODY=============
!2-TUBE BODY
!2.1-Defining Key Points in Cartesian
Coordinates
K,200,x4,0.000000,63.000000
K,201,x4,2.375000,63.000000
K,202,x4,3.138795,62.766609
K,203,x4,3.902589,62.468976
K,204,x4,4.666384,62.107406
K,205,x4,5.430179,61.682267
K,206,x4,6.193973,61.193996
K,207,x4,6.988179,60.619869
K,208,x4,7.782384,59.978658
K,209,x4,8.576589,59.271072
K,210,x4,9.370795,58.497896
K,211,x4,10.165000,57.659984
K,212,x4,12.865410,54.339761
K,213,x4,15.565820,50.325008
K,214,x4,18.266230,45.667038
K,215,x4,20.966640,40.425386
K,216,x4,23.667050,34.667047
K,217,x4,26.433640,28.308737
K,218,x4,29.200230,21.570674
K,219,x4,31.966820,14.543246
K,220,x4,34.733410,7.320726
K,221,x4,37.500000,0.000000
K,222,x4,0.000000,59.284499
K,223,x4,2.375000,59.284499
K,224,x4,4.284499,59.284499
K,225,x4,0.000000,57.659984
K,226,x4,2.375000,57.659984
K,227,x4,4.284499,57.659984
K,228,x4,0.000000,33.806000
K,229,x4,2.375000,33.806000
K,230,x4,4.284499,33.806000
K,231,x4,10.165000,33.806000
K,232,x4,22.806000,33.806000
K,233,x4,0.000000,0.000000
K,234,x4,2.375000,0.000000
K,235,x4,4.284499,0.000000
K,236,x4,10.165000,0.000000
K,237,x4,22.806000,0.000000

!2.2-Defining Lines & Splines
L,200,201 !Line 11
L,222,223 !Line 12
L,223,224 !Line 13
L,224,206 !Line 14
L,225,226 !Line 15
L,226,227 !Line 16
L,227,211 !Line 17
L,228,229 !Line 18
L,229,230 !Line 19
L,230,231 !Line 20
L,231,232 !Line 21
L,232,216 !Line 22
L,233,234 !Line 23
L,234,235 !Line 24
L,235,236 !Line 25
L,236,237 !Line 26
L,237,221 !Line 27
L,200,222 !Line 28
L,222,225 !Line 29
L,225,228 !Line 30
L,228,233 !Line 31
L,201,223 !Line 32
L,223,226 !Line 33
L,226,229 !Line 34
L,229,234 !Line 35
L,224,227 !Line 36
L,227,230 !Line 37
L,230,235 !Line 38
L,211,231 !Line 39
L,231,236 !Line 40
L,232,237 !Line 41
BSPLIN,201,202,203,204,205,206  !Line 42
BSPLIN,206,207,208,209,210,211  !Line 43
BSPLIN,211,212,213,214,215,216  !Line 44
BSPLIN,216,217,218,219,220,221  !Line 45


!2.3-Defining the Areas to be Extruded
AL,11,32,12,28 !Area 4
AL,12,33,15,29 !Area 5
AL,15,34,18,30 !Area 6
AL,18,35,23,31 !Area 7
AL,42,14,13,32 !Area 8
AL,13,36,16,33 !Area 9
AL,16,37,19,34 !Area 10
AL,19,38,24,35 !Area 11
AL,14,43,17,36 !Area 12
AL,17,39,20,37 !Area 13
AL,20,40,25,38 !Area 14
AL,44,22,21,39 !Area 15
AL,21,41,26,40 !Area 16
AL,22,45,27,41 !Area 17

!2.4-Defining the “CORE BACK” Volume
ALLSEL
ASEL,S,LOC,X,0,x3-0.001
VEXT,ALL,,,,,H10       !Extrude all areas
to the first overlap
ALLSEL
ASEL,S,LOC,Z,H10
```

```
VEXT,ALL,,,,,H11       !Extrude all areas
to the second overlap
ALLSEL
ASEL,S,LOC,Z,H1
VEXT,ALL,,,,,H2        !Extrude all areas
to the second overlap
ALLSEL
ASEL,S,LOC,Z,H1+H2
VEXT,ALL,,,,,H3-(Z_o2-(H1+H2))-(38.39797-
z_o2)   !Extrude all areas to the third
overlap
ALLSEL
ASEL,S,LOC,Z,H1+H2+(H3-(Z_o2-(H1+H2))-
(38.39797-z_o2))
VEXT,ALL,,,,,(38.39797-z_o2)  !Extrude all
areas to the third overlap
ALLSEL
ASEL,S,LOC,Z,H1+H2+(H3-(Z_o2-(H1+H2))-
(38.39797-z_o2))+(38.39797-z_o2)
VEXT,ALL,,,,,Z_o2-(H1+H2)     !Extrude all
areas to the third overlap
ALLSEL
ASEL,S,LOC,Z,H1+H2+H3
VEXT,ALL,,,,,H5        !Extrude all areas
to the third overlap

!2.5-Defining the “TUBE BODY” Volume
ALLSEL
ASEL,S,LOC,X,x4
VEXT,ALL,,,-x4,,

!2.6-UNION “CORE BACK” Volumes & “TUBE
BODY” Volumes
ALLSEL
VINP,ALL
ALLSEL
ASLV,S
CM,VOL_AREA,AREA
LSLA,S
CM,AREA_LIN,LINE
KSLL,S
CM,LIN_KP,KP
ALLSEL
CMSEL,U,VOL_AREA
CMSEL,U,AREA_LIN
CMSEL,U,LIN_KP
ADEL,ALL
LDEL,ALL
KDEL,ALL

ALLSEL
CM,VCORBAK1,VOLU
!==========Geo-TOOTH====================
!3-TOOTH
/TITLE,GEOMETRY-Creating the BASE Volume
ALLSEL
VPLOT
!3.1-Defining Key Points for the arcs in
Cylindrical Coordinates

CSYS,1
K,406,r6,0,0,,
K,407,r6,Theta61,0
K,408,r6,Theta62,0
K,409,r6,Theta63,0
K,410,r6,Theta65,0
K,412,r8,0,0
K,413,r8,Theta81,0
K,414,r8,Theta82,0
K,415,r8,Theta83,0
K,416,r8,Theta87,0
K,418,r9,0,0
K,419,r9,Theta91,0
K,420,r9,Theta92,0
K,421,r9,Theta93,0
K,422,r9,Theta98,0
K,423,r9,Theta911,0

!3.2-Defining Arcs
L,406,407      !Line1
L,407,408      !Line3
L,408,409      !Line4
L,409,410      !Line6
L,412,413      !Line11
L,413,414      !Line12
L,414,415      !Line13
L,415,416      !Line14
L,418,419      !Line15
L,419,420      !Line16
L,420,421      !Line17
L,421,422      !Line18
L,422,423      !Line19

!3.3-Defining Key Points for the inner
Lines in Cartesian Coordinates
CSYS,0
K,400,x4,0,0
K,401,x4,y1,0
K,402,x4,y2,0
K,403,x4,y3,0
K,404,x4,y4,0
K,405,x4,y6,0
K,411,x5,y9,0
K,417,x7,y10,0

!3.4-Defining Lines in Cartesian
Coordinates
L,400,401      !Line20
L,401,402      !Line21
L,402,403      !Line22
L,403,404      !Line23
L,404,405      !Line24
L,400,406      !Line25
L,401,407      !Line26
L,402,408      !Line27
L,403,409      !Line28
L,404,410      !Line29
L,405,411      !Line30
L,411,410      !Line31
L,406,412      !Line32
L,407,413      !Line33
L,408,414      !Line34
L,409,415      !Line35
L,410,416      !Line36
L,416,417      !Line37
L,412,418      !Line38
L,413,419      !Line39
L,414,420      !Line40
L,415,421      !Line41
L,416,422      !Line42
L,417,423      !Line43
L,411,417      !Line44

!3.5-Defining the Areas
AL,20,25,1,26
AL,21,26,3,27
```

```
AL,22,27,4,28
AL,23,28,6,29
AL,24,29,31,30
AL,1,32,11,33
AL,3,33,12,34
AL,4,34,13,35
AL,6,35,14,36
AL,11,38,15,39
AL,12,39,16,40
AL,13,40,17,41
AL,14,41,18,42
AL,37,42,19,43
AL,31,36,37,44

!3.6-Defining the Volumes
ALLSEL
ASEL,S,LOC,X,x4,r9
VEXT,ALL,,,,,H10

ALLSEL
ASEL,S,LOC,Z,H10
ASEL,R,LOC,X,x4,r9
VEXT,ALL,,,,,H11

ALLSEL
ASEL,S,LOC,Z,H1
ASEL,R,LOC,X,x4,r9
VEXT,ALL,,,,,H2

ALLSEL
ASEL,S,LOC,Z,H1+H2
ASEL,R,LOC,X,x4,r9
VEXT,ALL,,,,,33.806000-(H1+H2)

ALLSEL
ASEL,S,LOC,Z,33.806000
ASEL,R,LOC,X,x4,r9
ASEL,U,LOC,Y,0,y3
VEXT,ALL,,,,,(38.39797-33.806000)

ALLSEL
ASEL,S,LOC,Z,38.39797
ASEL,R,LOC,X,x4,r9
ASEL,U,LOC,Y,0,y3
VEXT,ALL,,,,,H3-2*(Z_o2-(H1+H2))-
2*(38.39797-z_o2)

ALLSEL
ASEL,S,LOC,Z,33.806000
ASEL,R,LOC,X,x4,r9
ASEL,R,LOC,Y,0,y3
VEXT,ALL,,,,,(H3-2*(Z_o2-(H1+H2))-
(38.39797-z_o2))

ALLSEL
ASEL,S,LOC,Z,38.39797+(H3-2*(Z_o2-
(H1+H2))-2*(38.39797-z_o2))
ASEL,R,LOC,X,x4,r9
!ASEL,U,LOC,Y,0,y3
VEXT,ALL,,,,,(38.39797-z_o2)

ALLSEL
ASEL,S,LOC,Z,38.39797+(H3-2*(Z_o2-
(H1+H2))-2*(38.39797-z_o2))+(38.39797-
z_o2)
ASEL,R,LOC,X,x4,r9
!ASEL,U,LOC,Y,0,y3
VEXT,ALL,,,,,(Z_o2-(H1+H2))

ALLSEL
ASEL,S,LOC,Z,H1+H2+H3
ASEL,R,LOC,X,x4,r9
VEXT,ALL,,,,,H4-H11
!========= Geo-WEB======================
!4-WEB
/TITLE,GEOMETRY-Creating the WEB
ALLSEL
VPLOT

!4.1-Defining the Volumes
ALLSEL
CSYS,0
ASEL,S,LOC,X,x3
ASEL,R,LOC,Y,0,y2
VEXT,ALL,,,x4-x3
!============Geo-COIL==============
!5-COIL
/TITLE,Geometry-Creating the Coil
ALLSEL
VPLOT

!5.1-Defining the Volumes
ALLSEL
ASEL,S,LOC,Y,y2,y3
ASEL,R,LOC,Z,0,H1+H2+H3+H4-H11
ASEL,R,LOC,X,x4
VEXT,ALL,,,-(x4-x3)

ALLSEL
VSEL,S,LOC,X,(X3+X4)/2
VSEL,U,LOC,Y,Y2,Y3
VSEL,U,LOC,Z,0,H1+H2+H3
VSEL,U,LOC,Y,0,Y1
CM,VTPCRBK,VOLU

ALLSEL
ASEL,S,LOC,Z,H1+H2+H3,H1+H2+H3+H4-H11
ASEL,R,LOC,X,x3,x4
ASEL,R,LOC,Y,y2
VEXT,ALL,,,,-(y2-y_p1)

ALLSEL
ASEL,S,LOC,Z,H1+H2+H3,H1+H2+H3+H4-H11
ASEL,R,LOC,X,x3,x4
ASEL,R,LOC,Y,y_p1
VEXT,ALL,,,,-(y_p1-y1)

ALLSEL
VSEL,S,LOC,X,(X3+X4)/2
VSEL,U,LOC,Y,Y2,Y3
VSEL,U,LOC,Z,0,H1+H2+H3
VSEL,U,LOC,Y,0,Y1
CMSEL,U,VTPCRBK,VOLU
CM,VTPCOIL,VOLU

ALLSEL
CMSEL,S,VTPCRBK,VOLU
CMSEL,A,VTPCOIL,VOLU
VSBV,VTPCOIL,VTPCRBK,,DELETE,KEEP

ALLSEL
ASEL,S,LOC,Z,(63+H1+H2+H3+H4-H11)/2
VEXT,ALL,,,,-y1

ALLSEL
ASEL,S,LOC,X,x3,x4
```

```
ASEL,R,LOC,Y,y2,y3
ASEL,R,LOC,Z,0
VEXT,ALL,,,,,-H2

ALLSEL
ASEL,S,LOC,Z,-H2/2
ASEL,R,LOC,Y,y2
VEXT,ALL,,,,-(y2-y_o1)

ALLSEL
ASEL,S,LOC,z,-H2/2
ASEL,R,LOC,y,y_o1
VEXT,ALL,,,,-(y_o1-y1)

ALLSEL
ASEL,S,LOC,z,-H2/2
ASEL,R,LOC,y,y1
VEXT,ALL,,,,-y1
!==========Geo-WEB====================
!6-WEB
/TITLE,GEOMETRY-ReCreating the WEB
ALLSEL
VPLOT

ASEL,S,LOC,x,x3
ASEL,U,LOC,z,-H2/2
VEXT,ALL,,,r9-x3
ALLSEL
VOVLAP,all

ALLSEL
CSYS,1
vsel,s,loc,x,r9,r10
VDELE,all,,,1
!==================Geo-Base==============
!7-Base
/TITLE,GEOMETRY-Finish Creating the Tooth
ALLSEL
VPLOT

CSYS,0
ASEL,S,LOC,Z,H1+H2+H3+H4-H11
VEXT,ALL,,,,,H11       !Extrude all areas
to the third overlap

CSYS,0
ASEL,S,LOC,Z,H1+H2+H3+H4
ASEL,R,LOC,X,x4,r9
VEXT,ALL,,,,,H5               !Extrude all
areas to the third overlap

!============Geo-Outside Casing===========
!8-Outside Casing
/TITLE,GEOMETRY-Creating the Outside
Casing
ALLSEL
VPLOT

CSYS,1
ASEL,S,LOC,X,r9
VEXT,ALL,,,r10-r9

!=============== V-Grouping Pole-1========
/TITLE,Grouping lines, areas, and volumes
associated with first pole piece.
ALLSEL
VPLOT

ALLSEL
VSEL,S,LOC,X,r9,r10
VSEL,R,LOC,Y,0,2*theta
CM,VCASING1,VOLU

ALLSEL
VSEL,S,LOC,X,(r6+r8)/2
VSEL,U,LOC,Y,0,13.5
CM,VTBASE2,VOLU

ALLSEL
CSYS,0
VSEL,S,LOC,X,x3,x4
VSEL,R,LOC,Y,y2,y3
CM,VCOIL1,VOLU

ALLSEL
VSEL,S,LOC,X,x3,x4
VSEL,R,LOC,Y,0,y2
VSEL,R,LOC,Z,63,H1+H2+H3+H4
CMSEL,A,VCOIL1,VOLU
CM,VCOIL1,VOLU

ALLSEL
VSEL,S,LOC,Y,0,y2
VSEL,R,LOC,Z,-H2/2
CMSEL,A,VCOIL1,VOLU
CM,VCOIL1,VOLU

ALLSEL
VSEL,S,LOC,X,0,x3
CM,VCORBAK1,VOLU

ALLSEL
CMSEL,U,VCORBAK1,VOLU
CMSEL,U,VTBASE2,VOLU
CMSEL,U,VCOIL1,VOLU
CMSEL,U,VCASING1,VOLU
CM,VTOOTH1,VOLU

ALLSEL
CMSEL,S,VTOOTH1,VOLU
VSEL,U,LOC,X,0,x4
CM,BASE1,VOLU

ALLSEL
CMSEL,S,VTOOTH1,VOLU
VSEL,U,LOC,X,x4,r9
CM,WEB1,VOLU

ALLSEL
CMSEL,U,VTBASE2,VOLU
CM,VPole1,VOLU

ALLSEL
CSYS,1
ASEL,S,LOC,X,(r6+r8)/2
ASEL,U,LOC,Y,0,13.5
CM,ATBASE2,AREA

ALLSEL
CSYS,0
CMSEL,U,ATBASE2,AREA
CM,APole1,AREA

ALLSEL
CSYS,1
LSEL,S,LOC,X,(r6+r8)/2
```

```
LSEL,U,LOC,Y,0,13.5
CM,LTBASE2,LINE

ALLSEL
CSYS,0
CMSEL,U,LTBASE2,LINE
CM,LPole1,LINE

!==========VI-SECOND GEOMETRY=============
/Title,Creating the Second Pole
ALLSEL
VPLOT

ALLSEL
CSYS,0
VSYMM,Y,ALL

ALLSEL
VSEL,U,LOC,Y,0,y12
LOCAL,11,0,0,0,-H2
VSYMM,Z,ALL

ALLSEL
VSEL,U,LOC,Y,0,y12
VSEL,U,LOC,Z,0,H1+H2+H3+H4+H5+2*H2
CSYS,1
VGEN,2,ALL,,,,2*theta,H1+H2+H3+H4+H5+2*H2

ALLSEL
CSYS,0
VSEL,U,LOC,Y,0,2*y12
VDELE,ALL,,,1
ALLSEL

!=========VII-Grouping Pole-2============
/TITLE,Grouping lines, areas, and volumes
associated with second pole piece.
ALLSEL
VPLOT

CSYS,1
LOCAL,20,0,0,0,H1+H2+H3+H4+H5,2*theta,180
CSYS,1
LOCAL,21,1,0,0,H1+H2+H3+H4+H5,2*theta,180

ALLSEL
CMSEL,U,VPole1,VOLU
CMSEL,U,APOLE1,AREA
CMSEL,U,LPOLE1,LINE
CSYS,20
VSEL,S,LOC,X,0,x3
CM,VCORBAK2,VOLU

ALLSEL
CMSEL,U,VPole1,VOLU
CMSEL,U,APOLE1,AREA
CMSEL,U,LPOLE1,LINE
CSYS,20
VSEL,S,LOC,X,x3,x4
VSEL,R,LOC,Y,y2,y3
CM,VCOIL2,VOLU

ALLSEL
CMSEL,U,VPole1,VOLU
CMSEL,U,APOLE1,AREA
CMSEL,U,LPOLE1,LINE
VSEL,S,LOC,X,x3,x4
VSEL,R,LOC,Y,0,y2
VSEL,R,LOC,Z,63,H1+H2+H3+H4
CMSEL,A,VCOIL2,VOLU
CM,VCOIL2,VOLU

ALLSEL
CMSEL,U,VPole1,VOLU
CMSEL,U,APOLE1,AREA
CMSEL,U,LPOLE1,LINE
VSEL,S,LOC,Y,0,y2
VSEL,R,LOC,Z,-H2/2
CMSEL,A,VCOIL2,VOLU
CM,VCOIL2,VOLU

ALLSEL
CSYS,20
CMSEL,U,VPole1,VOLU
CMSEL,U,APOLE1,AREA
CMSEL,U,LPOLE1,LINE
CSYS,21
VSEL,S,LOC,X,r9,r10
VSEL,U,LOC,Y,30,60
CM,VCASING2,VOLU

ALLSEL
CSYS,20
CMSEL,U,VPole1,VOLU
CMSEL,U,VCORBAK2,VOLU
CMSEL,U,VCOIL2,VOLU
CMSEL,U,VCASING2,VOLU
CMSEL,A,VTBASE2,VOLU
CM,VTOOTH2,VOLU

ALLSEL
CMSEL,S,VTOOTH2,VOLU
VSEL,U,LOC,X,0,x4
CM,BASE2,VOLU

ALLSEL
CMSEL,S,VTOOTH2,VOLU
VSEL,U,LOC,X,x4,r9
CM,WEB2,VOLU

!==========VIII-MERGE=============
/TITLE,Merging Coincident or Equivalently
Defined Items.
ALLSEL
VPLOT

ALLSEL
NUMMRG,ALL

!========IX-GENERTAING THE MESH========
/TITLE,GENERTAING THE MESH
ALLSEL
VPLOT

!bcsopt,,force,1800,,,-5
ET,1,SOLID90   !ELEMENT TYPE

!DESIZE,2,,,,,,,,
MSHKEY,0
MSHAPE,1,3
SMRTSIZE,10

ALLSEL
VSEL,S,VOLU,,VCORBAK1
TYPE,1
MAT,1
```

```
VMESH,ALL

ALLSEL
VSEL,S,VOLU,,VCORBAK2
VSEL,U,VOLU,,VCORBAK1
TYPE,1
MAT,1
VMESH,ALL

ALLSEL
VSEL,S,VOLU,,VCOIL1
TYPE,1
MAT,3
VMESH,ALL

ALLSEL
VSEL,S,VOLU,,VCOIL2
TYPE,1
MAT,3
VMESH,ALL

ALLSEL
VSEL,S,VOLU,,WEB1
TYPE,1
MAT,2
VMESH,ALL

ALLSEL
VSEL,S,VOLU,,WEB2
TYPE,1
MAT,2
VMESH,ALL

ALLSEL
VSEL,S,VOLU,,BASE1
VSEL,A,VOLU,,BASE2
TYPE,1
MAT,2
VMESH,ALL

ALLSEL
VSEL,S,VOLU,,VCASING1
VSEL,A,VOLU,,VCASING2
TYPE,1
MAT,4
VMESH,ALL

!=========VIII-MERGE================
/TITLE,Merging Coincident or Equivalently
Defined Items.
ALLSEL
VPLOT

ALLSEL
NUMMRG,ALL
NUMCMP,ALL
bcsopt,,,,,,-5
```

```
/FILNAME,Trial1,1
/config,nproc,2
/PREP7
/TITLE, Steady-State Thermal Analysis of
an Elec. Motor
/SHOW,
*AFUN, DEG     !Use degrees for
trigonometry functions

!=== II-Boundary Conditions & Body Loads==
T_inf_1=40     ![C]    !Channel temp-Zone A
T_inf_2=40     ![C]    !Channel temp-Zone B
T_inf_3=40     ![C]    !Channel temp-Zone C

T_i6=40![C]    !Inner Passage temp-Zone A
T_i3=40![C]    !Inner Passage temp-Zone B
T_i4=40![C]    !Inner Passage temp-Zone C

h_inf_1=255.1/1000000  ![W/mm2-K]
       !Channel htc - Zone A
h_inf_2=187.2/1000000  ![W/mm2-K]
       !Channel htc - Zone B
h_inf_3=163.5/1000000  ![W/mm2-K]
       !Channel htc - Zone C

h_i4=15/1000000               ![W/mm2-K]
       !Htc Side 1 Tooth 1.
h_i6=33.8/1000000             ![W/mm2-K]
       !Htc Side 1 Tooth 2.
h_i5=15/1000000               ![W/mm2-K]
       !Htc Side 1 Tooth 3.
h_i3=54.6/1000000             ![W/mm2-K]
       !Htc Side 1 Tooth 4.

h_i25=34.4/1000000            ![W/mm2-K]
       !Htc Side 2 Tooth 1.
h_i27=12.8/1000000            ![W/mm2-K]
       !Htc Side 2 Tooth 2.
h_i26=35.8/1000000            ![W/mm2-K]
       !Htc Side 2 Tooth 3.
h_i24=51.6/1000000            ![W/mm2-K]
       !Htc Side 2 Tooth 4.

h_i7=79/1000000               ![W/mm2-K]
       !Htc Side 1 Coil 1.
h_i9=59/1000000               ![W/mm2-K]
       !Htc Side 1 Coil 2.
h_i8=12/1000000               ![W/mm2-K]
       !Htc Side 1 Coil 3.
h_i10=21.3/1000000            ![W/mm2-K]
       !Htc Side 1 Coil 4.
h_i12=23.3/1000000            ![W/mm2-K]
       !Htc Side 1 Coil 5.
h_i11=8.8/1000000             ![W/mm2-K]
       !Htc Side 1 Coil 6.

h_i28=69/1000000              ![W/mm2-K]
       !Htc Side 2 Coil 1.
h_i17=41/1000000              ![W/mm2-K]
       !Htc Side 2 Coil 2.
h_i16=23.3/1000000            ![W/mm2-K]
       !Htc Side 2 Coil 3.
h_i18=15.5/1000000            ![W/mm2-K]
       !Htc Side 2 Coil 4.
h_i20=17.2/1000000            ![W/mm2-K]
       !Htc Side 2 Coil 5.
h_i19=22/1000000              ![W/mm2-K]
       !Htc Side 2 Coil 6.

h_i13=10/1000000              ![W/mm2-K]
       !Htc Side 1 Core Back 1.
h_i14=12.7/1000000            ![W/mm2-K]
       !Htc Side 1 Core Back 2.
h_i23=54.6/1000000            ![W/mm2-K]
       !Htc Side 1 Core Back 3.

h_i21=32.3/1000000            ![W/mm2-K]
       !Htc Side 2 Core Back 1.
h_i22=4/1000000               ![W/mm2-K]
       !Htc Side 2 Core Back 2.
h_i29=5.8/1000000             ![W/mm2-K]
       !Htc Side 2 Core Back 3.

!Inner Passage Zone B Temperatures
T_i7=T_i3
T_i24=T_i3
T_i28=T_i3

!Inner Passage Zone C Temperatures
T_i5=T_i4
T_i8=T_i5
T_i11=T_i8
T_i14=T_i11
T_i17=T_i14
T_i18=T_i17
T_i20=T_i18
T_i21=T_i20
T_i24=T_i4
T_i29=T_i4

!Inner Passage Zone A Temperatures
T_i9=T_i6
T_i23=T_i6
T_i25=T_i6
T_i26=T_i6
T_i10=T_i9
T_i12=T_i10
T_i13=T_i12
T_i27=T_i13
T_i16=T_i27
T_i19=T_i16
T_i22=T_i19

n_poles=12![pole] !Total number of poles

VOl_coil=2*34037 ![mm3]!Coil Volume
vol_corbak=2*15699
Vol_tooth=2*81850![mm3]!Stator volumE

P_MOTOR=5000   ![W]    !Motor input Power
Q_genCoil=0.1*P_MOTOR/VOl_coil/n_poles
Q_gencorbak=0.04*P_MOTOR/Vol_corbak/n_pole
s
Q_gentooth=0.02*P_MOTOR/Vol_tooth/n_poles

!==IX-Boundary Conditions and Body Loads==
/TITLE,Applying Boundary Conditions and
Body Loads
ALLSEL
VPLOT

ET,2,SURF152,,,,0,1,0
KEYOPT,2,7,0
KEYOPT,2,8,4
KEYOPT,2,9,0
```

```
ET,3,SURF152,,,,0,1,0
KEYOPT,3,7,0
KEYOPT,3,8,4
KEYOPT,3,9,0

ET,4,SURF152,,,,0,1,0
KEYOPT,4,7,0
KEYOPT,4,8,4
KEYOPT,4,9,0

ET,5,SURF152,,,,0,1,0
KEYOPT,5,7,0
KEYOPT,5,8,4
KEYOPT,5,9,0

ET,6,SURF152,,,,0,1,0
KEYOPT,6,7,0
KEYOPT,6,8,4
KEYOPT,6,9,0

ET,7,SURF152,,,,0,1,0
KEYOPT,7,7,0
KEYOPT,7,8,4
KEYOPT,7,9,0

ET,8,SURF152,,,,0,1,0
KEYOPT,8,7,0
KEYOPT,8,8,4
KEYOPT,8,9,0

ET,9,SURF152,,,,0,1,0
KEYOPT,9,7,0
KEYOPT,9,8,4
KEYOPT,9,9,0

ET,10,SURF152,,,,0,1,0
KEYOPT,10,7,0
KEYOPT,10,8,4
KEYOPT,10,9,0

ET,11,SURF152,,,,0,1,0
KEYOPT,11,7,0
KEYOPT,11,8,4
KEYOPT,11,9,0

ET,12,SURF152,,,,0,1,0
KEYOPT,12,7,0
KEYOPT,12,8,4
KEYOPT,12,9,0

ET,13,SURF152,,,,0,1,0
KEYOPT,13,7,0
KEYOPT,13,8,4
KEYOPT,13,9,0

ET,14,SURF152,,,,0,1,0
KEYOPT,14,7,0
KEYOPT,14,8,4
KEYOPT,14,9,0

ET,15,SURF152,,,,0,1,0
KEYOPT,15,7,0
KEYOPT,15,8,4
KEYOPT,15,9,0

ET,16,SURF152,,,,0,1,0
KEYOPT,16,7,0
KEYOPT,16,8,4
KEYOPT,16,9,0

ET,17,SURF152,,,,0,1,0
KEYOPT,17,7,0
KEYOPT,17,8,4
KEYOPT,17,9,0

ET,18,SURF152,,,,0,1,0
KEYOPT,18,7,0
KEYOPT,18,8,4
KEYOPT,18,9,0

ET,19,SURF152,,,,0,1,0
KEYOPT,19,7,0
KEYOPT,19,8,4
KEYOPT,19,9,0

ET,20,SURF152,,,,0,1,0
KEYOPT,20,7,0
KEYOPT,20,8,4
KEYOPT,20,9,0

ET,21,SURF152,,,,0,1,0
KEYOPT,21,7,0
KEYOPT,21,8,4
KEYOPT,21,9,0

ET,22,SURF152,,,,0,1,0
KEYOPT,22,7,0
KEYOPT,22,8,4
KEYOPT,22,9,0

ET,23,SURF152,,,,0,1,0
KEYOPT,23,7,0
KEYOPT,23,8,4
KEYOPT,23,9,0

ET,24,SURF152,,,,0,1,0
KEYOPT,24,7,0
KEYOPT,24,8,4
KEYOPT,24,9,0

ET,25,SURF152,,,,0,1,0
KEYOPT,25,7,0
KEYOPT,25,8,4
KEYOPT,25,9,0

ET,26,SURF152,,,,0,1,0
KEYOPT,26,7,0
KEYOPT,26,8,4
KEYOPT,26,9,0

ET,27,SURF152,,,,0,1,0
KEYOPT,27,7,0
KEYOPT,27,8,4
KEYOPT,27,9,0

ET,28,SURF152,,,,0,1,0
KEYOPT,28,7,0
KEYOPT,28,8,4
KEYOPT,28,9,0

ET,29,SURF152,,,,0,1,0
KEYOPT,29,7,0
KEYOPT,29,8,4
KEYOPT,29,9,0

ET,30,SURF152,,,,0,1,0
KEYOPT,30,7,0
```

```
KEYOPT,30,8,4
KEYOPT,30,9,0

ET,31,SURF152,,,,0,1,0
KEYOPT,31,7,0
KEYOPT,31,8,4
KEYOPT,31,9,0

!================ BC-OutSide============
!1-Outside Convection Boundary Condition
(T_inf,h_inf)
ALLSEL
CSYS,0
ASEL,S,LOC,z,0,H_s/3
CSYS,1
ASEL,R,LOC,X,r10
NSLA,S,1
N,3600032,r10+5,-5,0
TYPE,2
ESURF,3600032
D,3600032,TEMP,T_inf_1
ESEL,R,TYPE,,2
SFE,all,1,conv,0,h_inf_1,h_inf_1,h_inf_1,h
_inf_1

ALLSEL
CSYS,0
ASEL,S,LOC,z,H_s/3,2*H_s/3
CSYS,1
ASEL,R,LOC,X,r10
NSLA,S,1
N,3600030,r10+5.1,-5,0
TYPE,30
ESURF,3600030
D,3600030,TEMP,T_inf_2
ESEL,R,TYPE,,30
SFE,all,1,conv,0,h_inf_2,h_inf_2,h_inf_2,h
_inf_2

ALLSEL
CSYS,0
ASEL,S,LOC,z,2*H_s/3,H_s
CSYS,1
ASEL,R,LOC,X,r10
NSLA,S,1
N,3600031,r10+5.2,-5,0
TYPE,31
ESURF,3600031
D,3600031,TEMP,T_inf_3
ESEL,R,TYPE,,31
SFE,all,1,conv,0,h_inf_3,h_inf_3,h_inf_3,h
_inf_3
!=========== BC-Tooth Inside==============
!2-Inside Convection Boundary Condition
(T_i,h_i)
!2.1 Tooth interior between coils
ALLSEL
CSYS,0
ASEL,S,LOC,X,x4
ASEL,U,LOC,Y,0,y3
ASEL,U,LOC,Y,y9,100
NSLA,S,1
N,360003,x4,-5,0
TYPE,3
ESURF,360003
D,360003,TEMP,T_i3
ESEL,R,TYPE,,3
SFE,all,1,conv,0,h_i3,h_i3,h_i3,h_i3

!++++++++++++++++++++++++++++++++++++++++
!2.2 Tooth above coils
ALLSEL
CSYS,0
ASEL,S,LOC,X,x4
ASEL,R,LOC,Y,0,y3
ASEL,U,LOC,Y,y9,100
ASEL,R,LOC,Z,H1+H2+H3+H4,H1+H2+H3+H4+H5
NSLA,S,1
N,360004,x4,-5,1
TYPE,4
ESURF,360004
D,360004,TEMP,T_i4
ESEL,R,TYPE,,4
SFE,all,1,conv,0,h_i4,h_i4,h_i4,h_i4

!++++++++++++++++++++++++++++++++++++++++
!2.3 Tooth ends
!2.3.1 Top end
ALLSEL
CSYS,0
ASEL,S,AREA,,APole1
ASEL,R,LOC,Z,H1+H2+H3+H4+H5
NSLA,S,1
N,360005,x4,-5,2
TYPE,5
ESURF,360005
D,360005,TEMP,T_i5
ESEL,R,TYPE,,5
SFE,all,1,conv,0,h_i5,h_i5,h_i5,h_i5

!++++++++++++++++++++++++++++++++++++++++
!2.3.2 Bottom end
ALLSEL
CSYS,0
ASEL,S,LOC,Z,0
ASEL,R,LOC,Y,0,Y5
CSYS,1
ASEL,R,LOC,X,R6,R9
ASEL,U,AREA,,14
CM,IPEM1,AREA

ALLSEL
CSYS,0
ASEL,S,AREA,,APole1
ASEL,R,LOC,Z,0
ASEL,U,LOC,X,0,x4
ASEL,U,AREA,,IPEM1
NSLA,S,1
N,360006,x4,-5,3
TYPE,6
ESURF,360006
D,360006,TEMP,T_i6
ESEL,R,TYPE,,6
SFE,all,1,conv,0,h_i6,h_i6,h_i6,h_i6

!============BC-Coil Inside===============
!2.4 Coil interior
ALLSEL
CSYS,0
ASEL,S,AREA,,APole1
ASEL,R,LOC,X,(x3+x4)/2
ASEL,R,LOC,Y,y3
NSLA,S,1
N,360007,x3,-5,0
TYPE,7
ESURF,360007
D,360007,TEMP,T_i7
ESEL,R,TYPE,,7
```

```
SFE,all,1,conv,0,h_i7,h_i7,h_i7,h_i7

!+++++++++++++++++++++++++++++++++++++++
!2.5 Coil ends
!2.5.1 Coil tops
ALLSEL
CSYS,0
ASEL,S,AREA,,APole1
ASEL,R,LOC,X,(x3+x4)/2
ASEL,R,LOC,Z,H1+H2+H3+H4
NSLA,S,1
N,360008,x3,-5,1
TYPE,8
ESURF,360008
D,360008,TEMP,T_i8
ESEL,R,TYPE,,8
SFE,all,1,conv,0,h_i8,h_i8,h_i8,h_i8

!+++++++++++++++++++++++++++++++++++++++
!2.5.2 Coil bottoms
ALLSEL
CSYS,0
ASEL,S,AREA,,APole1
ASEL,R,LOC,Z,-H2
NSLA,S,1
N,360009,x3,-5,2
TYPE,9
ESURF,360009
D,360009,TEMP,T_i9
ESEL,R,TYPE,,9
SFE,all,1,conv,0,h_i9,h_i9,h_i9,h_i9

!+++++++++++++++++++++++++++++++++++++++
!2.6 Coil sides
!2.6.1a Bottom Inner sides
ALLSEL
CSYS,0
VSEL,S,VOLU,,VCOIL1
ASLV
ASEL,R,LOC,Y,0,y3
ASEL,R,LOC,X,x3
ASEL,R,LOC,Z,-11.78,0
NSLA,S,1
N,3600010,x3,-5,3
TYPE,10
ESURF,3600010
D,3600010,TEMP,T_i10
ESEL,R,TYPE,,10
SFE,all,1,conv,0,h_i10,h_i10,h_i10,h_i10
!+++++++++++++++++++++++++++++++++++++++
!2.6 Coil sides
!2.6.1b Top Inner sides
ALLSEL
CSYS,0
VSEL,S,VOLU,,VCOIL1
ASLV
ASEL,R,LOC,Y,0,y3
ASEL,R,LOC,X,x3
ASEL,R,LOC,Z,57.65998,74.78
NSLA,S,1
N,3600011,x3,-5,4
TYPE,11
ESURF,3600011
D,3600011,TEMP,T_i11
ESEL,R,TYPE,,11
SFE,all,1,conv,0,h_i11,h_i11,h_i11,h_i11
!+++++++++++++++++++++++++++++++++++++++
!2.6.2 Outer sides
ALLSEL
CSYS,0
ASEL,S,AREA,,APole1
ASEL,R,LOC,X,x4
ASEL,R,LOC,Z,-H2,0
NSLA,S,1
N,3600012,x3,-5,5
TYPE,12
ESURF,3600012
D,3600012,TEMP,T_i12
ESEL,R,TYPE,,12
SFE,all,1,conv,0,h_i12,h_i12,h_i12,h_i12
!==============BC-Core Back Inside======
!2.7 Core back
!2.7.1 (Surface 1)
ALLSEL
CSYS,0
ASEL,S,AREA,,APole1
ASEL,R,LOC,Y,y_o2
ASEL,R,LOC,Z,0,z_o2
CM,INCORBAK1,AREA

ALLSEL
CSYS,0
ASEL,S,AREA,,APole1
ASEL,R,LOC,X,71.44849,82.90222
ASEL,R,LOC,Y,y_o2,23.66705
ASEL,R,LOC,Z,z_o2,34.66705
CMSEL,A,INCORBAK1,AREA
CM,INCORBAK1,AREA

ALLSEL
CSYS,0
ASEL,S,AREA,,APole1
ASEL,U,LOC,X,x3,r10
ASEL,U,LOC,Y,y3,y12
ASEL,U,LOC,Y,0
ASEL,U,LOC,Y,y1
ASEL,U,LOC,Y,y2
ASEL,U,LOC,Y,y_O1
ASEL,U,LOC,Y,y_p1,y12
ASEL,U,LOC,Z,z_p1,63
ASEL,U,LOC,Z,0,38.39797
ASEL,U,LOC,Z,38.39797+(H3-2*(Z_o2-
(H1+H2))-2*(38.39797-z_o2))
ASEL,U,LOC,Z,38.39797+(H3-2*(Z_o2-
(H1+H2))-2*(38.39797-z_o2))+(38.39797-
z_o2)
ASEL,U,LOC,Z,H1+H2+H3
CSYS,1
ASEL,U,LOC,X,r1
CMSEL,A,INCORBAK1,AREA
CM,INCORBAK1,AREA

ALLSEL
CSYS,0
ASEL,S,AREA,,APole1
ASEL,U,LOC,X,x3,r10
ASEL,U,LOC,Y,0,y3
CSYS,1
ASEL,U,LOC,X,r1
ASEL,U,LOC,Z,H1
ASEL,U,LOC,Z,H1+H2
ASEL,U,LOC,Z,z_o2
ASEL,U,LOC,Z,H10
ASEL,U,AREA,,INCORBAK1
CM,SACORBAK1,AREA

ALLSEL
CSYS,0
```

```
ASEL,S,AREA,,APole1
ASEL,U,LOC,X,x3,r10
ASEL,U,LOC,Y,y3,y12
ASEL,U,LOC,Y,0
ASEL,U,LOC,Y,y1
ASEL,U,LOC,Y,y2
ASEL,U,LOC,Y,y_O1
ASEL,U,LOC,Z,0.1,38.39797
ASEL,U,LOC,Z,38.39797+(H3-2*(Z_o2-
(H1+H2))-2*(38.39797-z_o2))
ASEL,U,LOC,Z,38.39797+(H3-2*(Z_o2-
(H1+H2))-2*(38.39797-z_o2))+(38.39797-
z_o2)
ASEL,U,LOC,Z,H1+H2+H3
CSYS,1
ASEL,U,LOC,X,r1
ASEL,U,AREA,,INCORBAK1
CMSEL,A,SACORBAK1,AREA
CM,SACORBAK1,AREA
ASEL,R,LOC,Z,0
NSLA,S,1
N,3600013,x3,-5,6
TYPE,13
ESURF,3600013
D,3600013,TEMP,T_i13
ESEL,R,TYPE,,13
SFE,all,1,conv,0,h_i13,h_i13,h_i13,h_i13

!2.7.2 (Surface 2)

ALLSEL
CSYS,0
ASEL,S,AREA,,APole1
ASEL,U,LOC,X,x3,r10
ASEL,U,LOC,Y,y3,y12
ASEL,U,LOC,Y,0
ASEL,U,LOC,Y,y1
ASEL,U,LOC,Y,y2
ASEL,U,LOC,Y,y_O1
ASEL,U,LOC,Z,0.1,38.39797
ASEL,U,LOC,Z,38.39797+(H3-2*(Z_o2-
(H1+H2))-2*(38.39797-z_o2))
ASEL,U,LOC,Z,38.39797+(H3-2*(Z_o2-
(H1+H2))-2*(38.39797-z_o2))+(38.39797-
z_o2)
ASEL,U,LOC,Z,H1+H2+H3
CSYS,1
ASEL,U,LOC,X,r1
ASEL,U,AREA,,INCORBAK1
CMSEL,A,SACORBAK1,AREA
CM,SACORBAK1,AREA
ASEL,U,LOC,Z,0
ASEL,U,AREA,,1226
ASEL,U,AREA,,961
ASEL,U,AREA,,1229
ASEL,U,AREA,,885
ASEL,U,AREA,,1216
ASEL,U,AREA,,1210
ASEL,U,AREA,,873
ASEL,U,AREA,,175
ASEL,U,AREA,,952
NSLA,S,1
N,3600014,x3,-5,7
TYPE,14
ESURF,3600014
D,3600014,TEMP,T_i14
ESEL,R,TYPE,,14
SFE,all,1,conv,0,h_i14,h_i14,h_i14,h_i14

ALLSEL
CSYS,0
ASEL,S,AREA,,1226
ASEL,A,AREA,,961
ASEL,A,AREA,,1229
ASEL,A,AREA,,885
ASEL,A,AREA,,1216
ASEL,A,AREA,,1210
ASEL,A,AREA,,873
ASEL,A,AREA,,175
ASEL,A,AREA,,952
NSLA,S,1
N,3600023,x4,-5.1,1
TYPE,23
ESURF,3600023
D,3600023,TEMP,T_i23
ESEL,R,TYPE,,23
SFE,all,1,conv,0,h_i23,h_i23,h_i23,h_i23

!==============BC-Tooth Inside=========
!2-Inside Convection Boundary Condition
(T_i,h_i)
!2.1 Tooth interior between coils

ALLSEL
CSYS,20
ASEL,S,LOC,X,x4
ASEL,U,LOC,Y,0,y3
ASEL,U,LOC,Y,y9,100
NSLA,S,1
N,3600024,x4,-5.2,1
TYPE,24
ESURF,3600024
D,3600024,TEMP,T_i24
ESEL,R,TYPE,,24
SFE,all,1,conv,0,h_i24,h_i24,h_i24,h_i24
!++++++++++++++++++++++++++++++++++++++++

!2.2 Tooth above coils

ALLSEL
CSYS,20
ASEL,S,LOC,X,x4
ASEL,R,LOC,Y,0,y3
ASEL,U,LOC,Y,y9,100
ASEL,R,LOC,Z,H1+H2+H3+H4,H1+H2+H3+H4+H5
NSLA,S,1
N,3600025,x4,-5.3,1
TYPE,25
ESURF,3600025
D,3600025,TEMP,T_i25
ESEL,R,TYPE,,25
SFE,all,1,conv,0,h_i25,h_i25,h_i25,h_i25
!++++++++++++++++++++++++++++++++++++++++
!2.3 Tooth ends
!2.3.1 Top end

ALLSEL
CSYS,20
ASEL,U,AREA,,APole1
ASEL,R,LOC,Z,H1+H2+H3+H4+H5
NSLA,S,1
N,3600026,x4,-5.4,1
TYPE,26
ESURF,3600026
D,3600026,TEMP,T_i26
ESEL,R,TYPE,,26
SFE,all,1,conv,0,h_i26,h_i26,h_i26,h_i26
!++++++++++++++++++++++++++++++++++++++++
```

```
!2.3.2 Bottom end
ALLSEL
CSYS,20
ASEL,S,LOC,Z,0
ASEL,R,LOC,Y,0,Y5
CSYS,21
ASEL,R,LOC,X,R6,R9
ASEL,U,AREA,,1366
CM,IPEM2,AREA

ALLSEL
CSYS,20
ASEL,U,AREA,,APole1
ASEL,R,LOC,Z,0
ASEL,U,LOC,X,0,x4
ASEL,U,AREA,,IPEM2
NSLA,S,1
N,3600027,x4,-5.5,1
TYPE,27
ESURF,3600027
D,3600027,TEMP,T_i27
ESEL,R,TYPE,,27
SFE,all,1,conv,0,h_i27,h_i27,h_i27,h_i27

!==================BC-Coil Inside==========
!2.4 Coil interior

ALLSEL
CSYS,20
ASEL,U,AREA,,APole1
ASEL,S,LOC,X,(x3+x4)/2
ASEL,R,LOC,Y,y3
NSLA,S,1
N,3600028,x4,-5.6,1
TYPE,28
ESURF,3600028
D,3600028,TEMP,T_i28
ESEL,R,TYPE,,28
SFE,all,1,conv,0,h_i28,h_i28,h_i28,h_i28
!++++++++++++++++++++++++++++++++++++++++
!2.5 Coil ends
!2.5.1 Coil tops

ALLSEL
CSYS,20
ASEL,U,AREA,,APole1
ASEL,S,LOC,X,(x3+x4)/2
ASEL,R,LOC,Z,H1+H2+H3+H4
NSLA,S,1
N,3600016,x3,-5,1
TYPE,16
ESURF,3600016
D,3600016,TEMP,T_i16
ESEL,R,TYPE,,16
SFE,all,1,conv,0,h_i16,h_i16,h_i16,h_i16
!++++++++++++++++++++++++++++++++++++++++
!2.5.2 Coil bottoms

ALLSEL
CSYS,20
ASEL,U,AREA,,APole1
ASEL,S,LOC,Z,-H2
NSLA,S,1
N,3600017,x3,-5,2
TYPE,17
ESURF,3600017
D,3600017,TEMP,T_i17
ESEL,R,TYPE,,17
SFE,all,1,conv,0,h_i17,h_i17,h_i17,h_i17
!++++++++++++++++++++++++++++++++++++++++

!2.6 Coil sides
!2.6.1a Bottom Inner sides

ALLSEL
CSYS,20
VSEL,S,VOLU,,VCOIL2
ASLV
ASEL,R,LOC,Y,0,y3
ASEL,R,LOC,X,x3
ASEL,R,LOC,Z,-11.78,0
NSLA,S,1
N,3600018,x3,-5,3
TYPE,18
ESURF,3600018
D,3600018,TEMP,T_i18
ESEL,R,TYPE,,18
SFE,all,1,conv,0,h_i18,h_i18,h_i18,h_i18
!++++++++++++++++++++++++++++++++++++++++
!2.6 Coil sides
!2.6.1b Top Inner sides

ALLSEL
CSYS,20
VSEL,S,VOLU,,VCOIL2
ASLV
ASEL,R,LOC,Y,0,y3
ASEL,R,LOC,X,x3
ASEL,R,LOC,Z,57.65998,74.78
NSLA,S,1
N,3600019,x3,-5,4
TYPE,19
ESURF,3600019
D,3600019,TEMP,T_i19
ESEL,R,TYPE,,19
SFE,all,1,conv,0,h_i19,h_i19,h_i19,h_i19
!++++++++++++++++++++++++++++++++++++++++
!2.6.2 Outer sides

ALLSEL
CSYS,20
ASEL,U,AREA,,APole1
ASEL,S,LOC,X,x4
ASEL,R,LOC,Z,-H2,0
NSLA,S,1
N,3600020,x3,-5,5
TYPE,20
ESURF,3600020
D,3600020,TEMP,T_i20
ESEL,R,TYPE,,20
SFE,all,1,conv,0,h_i20,h_i20,h_i20,h_i20
!==============BC-Core Back Inside======
!2.7 Core back

ALLSEL
CSYS,20
ASEL,U,AREA,,APole1
ASEL,S,LOC,Y,y_o2
ASEL,R,LOC,Z,0,z_o2
CM,INCORBAK2,AREA

ALLSEL
CSYS,20
ASEL,U,AREA,,APole1
ASEL,S,LOC,X,71.44849,82.90222
ASEL,R,LOC,Y,y_o2,23.66705
ASEL,R,LOC,Z,z_o2,34.66705
```

```
CMSEL,A,INCORBAK2,AREA
CM,INCORBAK2,AREA

ALLSEL
CSYS,20
ASEL,U,AREA,,APole1
ASEL,U,LOC,X,x3,r10
ASEL,U,LOC,Y,y3,y12
ASEL,U,LOC,Y,0
ASEL,U,LOC,Y,y1
ASEL,U,LOC,Y,y2
ASEL,U,LOC,Y,y_O1
ASEL,U,LOC,Y,y_p1,y12
ASEL,U,LOC,Z,z_p1,63
ASEL,U,LOC,Z,0,38.39797
ASEL,U,LOC,Z,38.39797+(H3-2*(Z_o2-
(H1+H2))-2*(38.39797-z_o2))
ASEL,U,LOC,Z,38.39797+(H3-2*(Z_o2-
(H1+H2))-2*(38.39797-z_o2))+(38.39797-
z_o2)
ASEL,U,LOC,Z,H1+H2+H3
CSYS,21
ASEL,U,LOC,X,r1
CMSEL,A,INCORBAK2,AREA
CM,INCORBAK2,AREA

ALLSEL
CSYS,20
ASEL,U,AREA,,APole1
ASEL,U,LOC,X,x3,r10
ASEL,U,LOC,Y,0,y3
CSYS,21
ASEL,U,LOC,X,r1
ASEL,U,LOC,Z,H1
ASEL,U,LOC,Z,H1+H2
ASEL,U,LOC,Z,z_o2
ASEL,U,LOC,Z,H10
ASEL,U,AREA,,INCORBAK2
CM,SACORBAK2,AREA

ALLSEL
CSYS,20
ASEL,U,AREA,,APole1
ASEL,U,LOC,X,x3,r10
ASEL,U,LOC,Y,y3,y12
ASEL,U,LOC,Y,0
ASEL,U,LOC,Y,y1
ASEL,U,LOC,Y,y2
ASEL,U,LOC,Y,y_O1
ASEL,U,LOC,Z,0.1,38.39797
ASEL,U,LOC,Z,38.39797+(H3-2*(Z_o2-
(H1+H2))-2*(38.39797-z_o2))
ASEL,U,LOC,Z,38.39797+(H3-2*(Z_o2-
(H1+H2))-2*(38.39797-z_o2))+(38.39797-
z_o2)
ASEL,U,LOC,Z,H1+H2+H3
CSYS,21
ASEL,U,LOC,X,r1
ASEL,U,AREA,,INCORBAK2
CMSEL,A,SACORBAK2,AREA
CM,SACORBAK2,AREA
ASEL,R,LOC,Z,0
NSLA,S,1
N,3600021,x3,-5,6
TYPE,21
ESURF,3600021
D,3600021,TEMP,T_i21
ESEL,R,TYPE,,21
SFE,all,1,conv,0,h_i21,h_i21,h_i21,h_i21

ALLSEL
CSYS,20
ASEL,U,AREA,,APole1
ASEL,U,LOC,X,x3,r10
ASEL,U,LOC,Y,y3,y12
ASEL,U,LOC,Y,0
ASEL,U,LOC,Y,y1
ASEL,U,LOC,Y,y2
ASEL,U,LOC,Y,y_O1
ASEL,U,LOC,Z,0.1,38.39797
ASEL,U,LOC,Z,38.39797+(H3-2*(Z_o2-
(H1+H2))-2*(38.39797-z_o2))
ASEL,U,LOC,Z,38.39797+(H3-2*(Z_o2-
(H1+H2))-2*(38.39797-z_o2))+(38.39797-
z_o2)
ASEL,U,LOC,Z,H1+H2+H3
CSYS,21
ASEL,U,LOC,X,r1
ASEL,U,AREA,,INCORBAK2
CMSEL,A,SACORBAK2,AREA
CM,SACORBAK2,AREA
ASEL,U,LOC,Z,0
ASEL,U,AREA,,2199
ASEL,U,AREA,,1461
ASEL,U,AREA,,2464
ASEL,U,AREA,,2118
ASEL,U,AREA,,2470
ASEL,U,AREA,,2134
ASEL,U,AREA,,2483
ASEL,U,AREA,,2215
ASEL,U,AREA,,2479
NSLA,S,1
N,3600022,x3,-5,7
TYPE,22
ESURF,3600022
D,3600022,TEMP,T_i22
ESEL,R,TYPE,,22
SFE,all,1,conv,0,h_i22,h_i22,h_i22,h_i22

ALLSEL
CSYS,20
ASEL,S,AREA,,2199
ASEL,A,AREA,,1461
ASEL,A,AREA,,2464
ASEL,A,AREA,,2118
ASEL,A,AREA,,2470
ASEL,A,AREA,,2134
ASEL,A,AREA,,2483
ASEL,A,AREA,,2215
ASEL,A,AREA,,2479
NSLA,S,1
N,3600029,x3,-5.1,7
TYPE,29
ESURF,3600029
D,3600029,TEMP,T_i29
ESEL,R,TYPE,,29
SFE,all,1,conv,0,h_i29,h_i29,h_i29,h_i29

!===================BC-Heat Gen=========
!3.Heat Generation
!3.1 Heat generation in poles

ALLSEL
ESEL,S,MAT,,1
BFE,ALL,HGEN,,Q_gencorbak

ALLSEL
ESEL,S,MAT,,2
```

```
BFE,ALL,HGEN,,Q_gentooth

!3.2 Heat generation in coils
ALLSEL
ESEL,S,MAT,,3
BFE,ALL,HGEN,,Q_genCoil

!3.3 Heat generation in IPEM
ALLSEL
ASEL,S,AREA,,IPEM1
ASEL,A,AREA,,IPEM2
NSLA,S,1
SF,ALL,HFLUX,(20.83/2)/322.85
![W/mm2]

!=========== VIII-MERGE==========
/TITLE,Merging Coincident or Equivalently
Defined Items.
ALLSEL
VPLOT
ALLSEL
NUMMRG,ALL
ALLSEL
NUMMRG,ALL
NUMCMP,ELEM
!bcsopt,,,,,,-5
!========== SOLVE================
/TITLE,SOLVING
ALLSEL
VPLOT

/SOLU
NROPT,AUTO
!TUNIF,T_i
AUTOTS,ON
NSUBST,50
KBC,0
OUTPR,NSOL,LAST
SOLVE
FINISH
```

Appendix B

MOTOR POLE DIMENSIONS

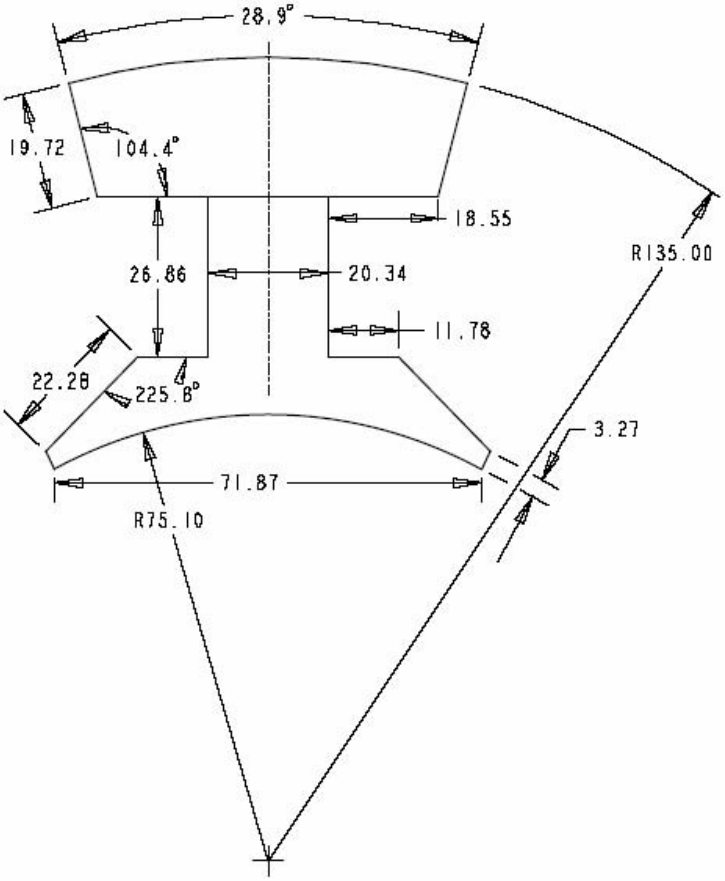

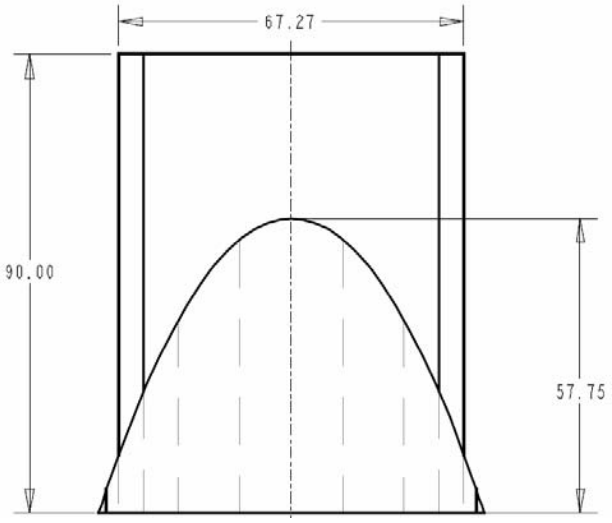

Appendix C

EES CODE FOR EQUIVALENT THERMAL CONDUCTIVITY CALCULATIONS

$$\bar{\lambda}_x = 2 \cdot \sqrt{3} \cdot (INT_1 + INT_2)$$

$$INT_1 = \int_0^{1-F} \left[\frac{\lambda_1 \cdot \lambda_2'}{(\lambda_2' - \lambda_1) \cdot \left(\sqrt{|F^2 - y^2|} \right) + \sqrt{3} \cdot \lambda_1} \right] dy$$

$$INT_2 = \int_{1-F}^{0.5} \left[\frac{\lambda_1 \cdot \lambda_2'}{(\lambda_1 - \lambda_2') \cdot \left(\sqrt{3} - \left[\sqrt{|F^2 - y1^2|} \right] - \left[\sqrt{|F^2 - (y1 - 1)^2|} \right] \right) + \sqrt{3} \cdot \lambda_2'} \right] dy1$$

$$\bar{\lambda}_y = \frac{2}{\sqrt{3}} \cdot (INT_3 + INT_4)$$

$$INT_3 = \int_0^{\sqrt{3}-F} \left[\frac{\lambda_1 \cdot \lambda_2'}{(\lambda_2' - \lambda_1) \cdot \left(\sqrt{|F^2 - x^2|} \right) + \lambda_1} \right] dx$$

$$INT_4 = \int_{\sqrt{3}-F}^{\sqrt{3}/2} \left[\lambda_1 \cdot \lambda_2' / (\lambda_1 - \lambda_2') \cdot \left(1 - \left[\sqrt{|F^2 - x1^2|} \right] - \left[\sqrt{\left| F^2 - \left(x1 - \sqrt{3} \right)^2 \right|} \right] \right) + \lambda_2' \right] dx1$$

$\bar{\lambda} =$ **Average** $(\bar{\lambda}_x + \bar{\lambda}_y)$

$$A_{Copper} = \frac{\pi}{2} \cdot \left[\frac{d}{2} \right]^2$$

$$A_{Total} = 1 / 4 \cdot \sqrt{3} \cdot a^2$$

$$a = d_i + t_{gap}$$

$$A_{Ins} = \frac{\pi}{8} \cdot (d_i^2 - d^2)$$

$$d_i = d + 2 \cdot t_{ins}$$

$$\phi_1 = \frac{A_{Copper}}{A_{Total}}$$

$$\phi_2 = \frac{A_{Ins}}{A_{Total}}$$

$$\phi_3 = 1 - (\phi_1 + \phi_2)$$

Appendix D

NEMA MAGNET WIRE SPECIFICATIONS

July 2003 Errata for
MW 1000-2003
Part 1—Page 12

Table 1-1 (mm)
DIMENSIONS FOR BARE AND FILM INSULATED ROUND MAGNET WIRE

AWG size	Bare Wire Diameter			Single Build		Heavy Build		Triple Build		Quad Build		AWG size
	Minimum	Nominal	Maximum	Minimum Increase In Diameter	Maximum Overall Diameter	Minimum Increase In Diameter	Maximum Overall Diameter	Minimum Increase In Diameter	Maximum Overall Diameter	Minimum Increase In Diameter	Maximum Overall Diameter	
4/0	11.567	11.684	11.801	—	—	—	—	—	—	—	—	4/0
3/0	10.300	10.404	10.508	—	—	—	—	—	—	—	—	3/0
2/0	9.174	9.266	9.357	—	—	—	—	—	—	—	—	2/0
1/0	8.171	8.252	8.334	—	—	—	—	—	—	—	—	1/0
1	7.275	7.348	7.422	—	—	—	—	—	—	—	—	1
2	6.477	6.543	6.609	—	—	—	—	—	—	—	—	2
3	5.768	5.827	5.885	—	—	—	—	—	—	—	—	3
4	5.138	5.189	5.240	—	—	0.094	5.329	—	—	—	—	4
5	4.575	4.620	4.666	—	—	0.094	4.755	—	—	—	—	5
6	4.074	4.115	4.156	—	—	0.091	4.244	—	—	—	—	6
7	3.630	3.665	3.701	—	—	0.089	3.787	—	—	—	—	7
8	3.231	3.264	3.297	—	—	0.089	3.383	—	—	—	—	8
9	2.878	2.906	2.934	—	—	0.086	3.023	—	—	—	—	9
10	2.563	2.588	2.614	—	—	0.086	2.703	—	—	—	—	10
11	2.281	2.304	2.327	—	—	0.084	2.416	—	—	—	—	11
12	2.032	2.052	2.073	—	—	0.081	2.159	—	—	—	—	12
13	1.811	1.829	1.847	—	—	0.081	1.935	—	—	—	—	13
14	1.613	1.628	1.643	0.041	1.692	0.081	1.732	0.122	1.773	0.163	1.814	14
15	1.435	1.450	1.466	0.038	1.509	0.076	1.549	0.117	1.588	0.155	1.626	15
16	1.278	1.290	1.303	0.036	1.349	0.074	1.384	0.109	1.422	0.147	1.458	16
17	1.138	1.151	1.163	0.036	1.207	0.071	1.240	0.104	1.275	0.140	1.311	17
18	1.013	1.024	1.034	0.033	1.077	0.066	1.110	0.099	1.143	0.132	1.179	18
19	0.902	0.912	0.922	0.030	0.963	0.064	0.993	0.094	1.028	0.127	1.062	19
20	0.805	0.813	0.820	0.030	0.864	0.061	0.892	0.089	0.922	0.119	0.955	20
21	0.716	0.724	0.732	0.028	0.770	0.056	0.800	0.086	0.828	0.114	0.861	21
22	0.635	0.643	0.650	0.028	0.686	0.053	0.714	0.081	0.742	0.109	0.775	22
23	0.569	0.574	0.579	0.025	0.617	0.051	0.643	0.076	0.668	0.102	0.704	23
24	0.505	0.511	0.516	0.025	0.551	0.048	0.577	0.074	0.599	0.097	0.636	24
25	0.450	0.455	0.460	0.023	0.493	0.046	0.516	0.069	0.538	0.091	0.574	25
26	0.399	0.404	0.409	0.023	0.439	0.043	0.462	0.066	0.485	0.089	0.518	26
27	0.358	0.361	0.363	0.020	0.396	0.041	0.419	0.064	0.439	0.084	0.467	27
28	0.318	0.320	0.323	0.020	0.356	0.041	0.373	0.058	0.394	0.079	0.419	28
29	0.284	0.287	0.290	0.018	0.320	0.038	0.338	0.056	0.358	0.076	0.384	29

Table continued on next page.

Appendix E

ANSYS IPEM MODEL CODE

```
/FILNAME,IPEM_long,1
/config,nproc,2
/PREP7
/TITLE, Steady-State Thermal Analysis of an
IPEM
/SHOW,
*AFUN, DEG

!=======PHYSICAL PROPERTIES==========

!Material (1) Chip - Silicon

MPTEMP,1,-73.15,26.85,126.85,326.85
MPDATA,DENS,1,1,2331/1000000,2330/1000000,2
328/1000000,2323/1000000      ![kg/cm3]
MPDATA,KXX,1,1,264/100,148/100,98.9/100,61.
9/100                  ![W/cm-K]
MPDATA,C,1,1,556,712,790,867  ![J/kg-K]

!Material (2) DBC Top/Bottom & Baseplate -
Copper

MPDATA,DENS,2,1,8976/1000000,8833/1000000,8
888/1000000,8791/1000000      ![kg/cm3]
MPDATA,KXX,2,1,413/100,401/100,393/100,379/
100                    ![W/cm-K]
MPDATA,C,2,1,356,385,397,417  ![J/kg-K]

!Material (3) DBC Middle - Alumina

MP,DENS,3,3980/1000000        ![kg/cm3]
MP,KXX,3,150/100              ![W/cm-K]
MP,C,3,750                    ![J/kg-K]

!Material (4) Heat Sink - Aluminum

MPDATA,DENS,4,1,2720/1000000,2702/1000000,2
682/1000000,2641/1000000      ![kg/cm3]
MPDATA,KXX,4,1,237/100,237/100,240/100,231/
100                    ![W/cm-K]
MPDATA,C,4,1,798,903,949,1033 ![J/kg-K]

!=== BOUNDARY CONDITIONS & BODY LOADS===

h_inf1=275/10000![W/cm2-K]

T_channel=40   ![C]

Q_gen=2773/2   ![W/cm^3]

T_SURF=250.58  ![C]

!=== PHYSICAL DIMENSIONS ===

!Define Points

x1=0
x2=0.1
x3=0.35
x4=1.35
x5=1.6
x6=1.7

x0=-0.125
x7=1.825

y1=0
y2=0.5
y3=1.04
y4=1.15
y5=2.75

z0=-1
z1=0
z2=0.5
z3=0.6
z4=0.6254
z5=0.6889
z6=0.7143
z7=0.8143
z8=0.8893

z9=0.8818

!Define Keypoints

K,1,x1,y1,z1
K,2,x2,y1,z1
K,3,x3,y1,z1
K,4,x4,y1,z1
K,5,x5,y1,z1
K,6,x6,y1,z1

K,7,x1,y2,z1
K,8,x2,y2,z1
K,9,x3,y2,z1
K,10,x4,y2,z1
K,11,x5,y2,z1
K,12,x6,y2,z1

K,13,x1,y3,z1
K,14,x2,y3,z1
K,15,x3,y3,z1
K,16,x4,y3,z1
K,17,x5,y3,z1
K,18,x6,y3,z1

K,19,x1,y4,z1
K,20,x2,y4,z1
K,21,x3,y4,z1
K,22,x4,y4,z1
K,23,x5,y4,z1
K,24,x6,y4,z1

K,25,X0,Y1,Z1
K,26,X0,Y2,Z1
K,27,X0,Y3,Z1
K,28,X0,Y4,Z1
K,29,X0,Y5,Z1
K,30,X1,Y5,Z1
```

```
K,31,X2,Y5,Z1
K,32,X3,Y5,Z1
K,33,X4,Y5,Z1
K,34,X5,Y5,Z1
K,35,X6,Y5,Z1
K,36,X7,Y5,Z1
K,37,X7,Y4,Z1
K,38,X7,Y3,Z1
K,39,X7,Y2,Z1
K,40,X7,Y1,Z1

!Define Lines

!Horizontal Lines
L,1,2                   !Line 1
L,2,3                   !Line 2
L,3,4                   !Line 3
L,4,5                   !Line 4
L,5,6                   !Line 5

L,7,8                   !Line 6
L,8,9                   !Line 7
L,9,10                  !Line 8
L,10,11                 !Line 9
L,11,12                 !Line 10
L,13,14                 !Line 11
L,14,15                 !Line 12
L,15,16                 !Line 13
L,16,17                 !Line 14
L,17,18                 !Line 15
L,19,20                 !Line 16
L,20,21                 !Line 17
L,21,22                 !Line 18
L,22,23                 !Line 19
L,23,24                 !Line 20

!Vertical Lines

L,1,7                   !Line 21
L,7,13                  !Line 22
L,13,19                 !Line 23
L,2,8                   !Line 24
L,8,14                  !Line 25
L,14,20                 !Line 26
L,3,9                   !Line 27
L,9,15                  !Line 28
L,15,21                 !Line 29
L,4,10                  !Line 30
L,10,16                 !Line 31
L,16,22                 !Line 32
L,5,11                  !Line 33
L,11,17                 !Line 34
L,17,23                 !Line 35
L,6,12                  !Line 36
L,12,18                 !Line 37
L,18,24                 !Line 38
L,25,1                  !Line 39
L,26,7                  !Line 40
L,27,13                 !Line 41
L,28,19                 !Line 42
L,29,30                 !Line 43
L,30,31                 !Line 44
L,31,32                 !Line 45
L,32,33                 !Line 46
L,33,34                 !Line 47
L,34,35                 !Line 48
L,35,36                 !Line 49
L,24,37                 !Line 50
L,18,38                 !Line 51
L,12,39                 !Line 52
L,6,40                  !Line 53
L,25,26                 !Line 54
L,26,27                 !Line 55
L,27,28                 !Line 56
L,28,29                 !Line 57
L,19,30                 !Line 58
L,20,31                 !Line 59
L,21,32                 !Line 60
L,22,33                 !Line 61
L,23,34                 !Line 62
L,24,35                 !Line 63
L,36,37                 !Line 64
L,37,38                 !Line 65
L,38,39                 !Line 66
L,39,40                 !Line 67

!Define Areas

AL,1,6,21,24            !Area 1
AL,2,7,24,27            !Area 2
AL,3,8,27,30            !Area 3
AL,4,9,30,33            !Area 4
AL,5,10,33,36           !Area 5
AL,6,11,22,25           !Area 6
AL,7,12,25,28           !Area 7
AL,8,13,28,31           !Area 8
AL,9,14,31,34           !Area 9
AL,10,15,34,37          !Area 10
AL,11,16,23,26          !Area 11
AL,12,17,26,29          !Area 12
AL,13,18,29,32          !Area 13
AL,14,19,32,35          !Area 14
AL,15,20,35,38          !Area 15
AL,39,54,40,21          !Area 16
AL,40,55,41,22          !Area 17
AL,41,56,42,23          !Area 18
AL,42,57,43,58          !Area 19
AL,58,44,59,16          !Area 20
AL,59,45,60,17          !Area 21
AL,60,46,61,18          !Area 22
AL,61,47,62,19          !Area 23
AL,62,48,63,20          !Area 24
AL,63,49,64,50          !Area 25
AL,38,50,65,51          !Area 26
AL,37,51,66,52          !Area 27
AL,36,52,67,53          !Area 28

!Define Volumes

ALLSEL
VEXT,ALL,,,,,Z0         !Heat Sink

ALLSEL
ASEL,S,LOC,X,X1,X6
ASEL,R,LOC,Y,Y1,Y4
ASEL,R,LOC,Z,Z1
VEXT,ALL,,,,,Z2         !Base Plate

ALLSEL
ASEL,S,LOC,X,X2,X5
ASEL,R,LOC,Y,Y0,Y3
ASEL,R,LOC,Z,Z2
AOFFST,ALL,Z3-Z2

ALLSEL
ASEL,S,LOC,Z,Z3
VEXT,ALL,,,,,Z4-Z3      !DBC Copper Bottom
```

```
ALLSEL
ASEL,S,LOC,Z,Z4
VEXT,ALL,,,,,Z5-Z4     !DBC Alumina

ALLSEL
ASEL,S,LOC,z,z5
VEXT,ALL,,,,,Z6-z5     !DBC Copper Top

ALLSEL
ASEL,S,LOC,x,x3,x4
ASEL,R,LOC,y,y1,y2
ASEL,R,LOC,z,z6
AOFFST,ALL,Z7-Z6

ALLSEL
ASEL,S,LOC,z,z7
VEXT,ALL,,,,,z9-z7     !Bottom Chip

ALLSEL
ASEL,S,LOC,z,z9
VEXT,ALL,,,,,z8-z9     !Top Chip

!==============DIVIDE GROUPED LINES=====

esize,,1

ALLSEL
LSEL,S,LENGTH,,X2-X1
CM,L1,LINES
ALLSEL
LSEL,S,LENGTH,,X3-X2
CM,L2,LINES
ALLSEL
LSEL,S,LENGTH,,X4-X3
CM,L3,LINES
ALLSEL
LSEL,S,LENGTH,,Y2-Y1
CM,L4,LINES
ALLSEL
LSEL,S,LENGTH,,Y3-Y2
CM,L5,LINES
ALLSEL
LSEL,S,LENGTH,,Z2-Z1
CM,L6,LINES
ALLSEL
LSEL,S,LENGTH,,(Z4-0.1)-(Z3-0.1)
CM,L7,LINES
ALLSEL
LSEL,S,LENGTH,,(Z5-0.1)-(Z4-0.1)
CM,L8,LINES
ALLSEL
LSEL,S,LENGTH,,(Z6-0.1)-(Z5-0.1)
CM,L9,LINES
ALLSEL
LSEL,S,LENGTH,,(Z9-0.2)-(Z7-0.2)
CM,L10,LINES
ALLSEL
LSEL,S,LENGTH,,Y5-Y4
CM,L11,LINES
ALLSEL
LSEL,S,LENGTH,,X1-X0
CM,L12,LINES
ALLSEL
CMSEL,S,L1
LESIZE,L1,,,2
ALLSEL
CMSEL,S,L2
LESIZE,L2,,,5
ALLSEL
CMSEL,S,L3
LESIZE,L3,,,10
ALLSEL
CMSEL,S,L4
LESIZE,L4,,,10
ALLSEL
CMSEL,S,L5
LESIZE,L5,,,4
ALLSEL
CMSEL,S,L6
LESIZE,L6,,,3
ALLSEL
CMSEL,S,L7
LESIZE,L7,,,2
ALLSEL
CMSEL,S,L8
LESIZE,L8,,,4
ALLSEL
CMSEL,S,L9
LESIZE,L9,,,2
ALLSEL
CMSEL,S,L10
LESIZE,L10,,,2
ALLSEL
CMSEL,S,L4
LESIZE,L4,,,10
ALLSEL
CMSEL,S,L11
LESIZE,L11,,,10
ALLSEL
CMSEL,S,L12
LESIZE,L12,,,10

!===========CREATE MESH=========

!Element Type 1 - Solid 70 for All Solid
Volumes

ET,1,SOLID70

ALLSEL
VSEL,S,LOC,Z,Z1,Z2
TYPE,1
MAT,2
VMESH,ALL
ALLSEL
VSEL,S,LOC,Z,Z3,Z4
TYPE,1
MAT,2
VMESH,ALL
ALLSEL
VSEL,S,LOC,Z,Z4,Z5
TYPE,1
MAT,3
VMESH,ALL
ALLSEL
VSEL,S,LOC,Z,Z5,Z6
TYPE,1
MAT,2
VMESH,ALL
ALLSEL
VSEL,S,LOC,Z,Z7,Z8
TYPE,1
MAT,1
VMESH,ALL
ALLSEL
VSEL,S,LOC,Z,Z0,Z1
TYPE,1
MAT,4
```

```
VMESH,ALL

!=============DEFINE TARGET SURFACE========

!Element Type 3 - Target Surface for
Contact Resistance

ET,3,TARGE170

ALLSEL
ASEL,S,LOC,Z,Z2
TYPE,3
AMESH,ALL

ALLSEL
ASEL,S,LOC,Z,Z6
TYPE,3
AMESH,ALL

!===========DEFINE CONTACT RESISTANCE=====

!Element Type 2 - Contact Resistance
Surface

ET,2,CONTA173,2,,,,1
KEYOPT,2,9,1
KEYOPT,2,12,5

R,1,,,,,
RMORE,
RMORE,,0.000000001

ALLSEL
ASEL,S,LOC,Z,Z3
TYPE,2
REAL,1
AMESH,ALL

ALLSEL
ASEL,S,LOC,Z,Z3
ESLA,S
ESURF,,REVERSE

ALLSEL
ASEL,S,LOC,Z,Z7
TYPE,2
REAL,1
AMESH,ALL

ALLSEL
ASEL,S,LOC,Z,Z7
ESLA,S
ESURF,,REVERSE

!=============CONNECT VOLUMES============

ALLSEL
VSEL,S,LOC,Z,Z0,Z2
VSEL,INVE
VGEN,2,ALL,,,,,-0.1,0,1,1

ALLSEL
VSEL,S,LOC,Z,Z7-0.1,Z8-0.1
VGEN,2,ALL,,,,,-0.1,0,1,1

!==============HEAT GENERATION============

ALLSEL
VSEL,S,LOC,Z,Z9-0.2,z8-0.2
ESLV,S
BFE,ALL,HGEN,,Q_gen

!=========SURFACE TEMPERATURE==========
h_b=64/10000

REAL,7
ET,7,SURF152,,,,1,1,0
KEYOPT,7,7,0
KEYOPT,7,8,4
KEYOPT,7,9,0

ALLSEL
ASEL,S,LOC,Z,Z0
NSLA,S
!N,400000,.45,.45,.45
!TYPE,7
!ESURF,400000
!D,400000,TEMP,T_cHANNEL
!ESEL,R,TYPE,,7
!SFE,ALL,1,CONV,0,h_b,h_b,h_b,h_b

D,ALL,TEMP,T_SURF

ALLSEL
NUMMRG,all,1e-9       !Merging Coincident
or Equivalently Defined Items.
!NUMCMP,ALL    !Compress the numbers of
lines, points, materials, nodes and
elements

!=========Solve Using Sparce Solver=======

/SOLU
NROPT,AUTO
!AUTOTS,ON
SOLCONTROL,ON
NSUBST
KBC,0
OUTPR,NSOL,LAST
!CHECK
SOLVE
```

Appendix F

ANSYS E-CORE MODEL CODE

```
/FILNAME,E_coil_2,1
/config,nproc,2
/PREP7
/TITLE, Steady-State Thermal Analysis of an
E_coil
/SHOW,
*AFUN, DEG

!====Wall Heat Transfer Coefficients=======

Q_coil=7.83            ![W]
Q_core=0.053           ![W]

T_i1=19.58037          ![C]
T_i2=20.50837          ![C]
T_i3=21.62193          ![C]

h_4=68.5/1000000 ![W/mm2-K]   !Coil 1
h_5=52.5/1000000 ![W/mm2-K]   !Coil 2
h_6=173.7/1000000![W/mm2-K]   !Coil 3_1
h_14=217.8/1000000![W/mm2-K]  !Coil 3_2
h_15=165.3/1000000![W/mm2-K]  !Coil 3_3
h_7=41.06/1000000![W/mm2-K]   !Coil 4
h_8=47.9/1000000![W/mm2-K]    !Coil 5
h_9=56.7/1000000![W/mm2-K]    !Ecore In 1
h_10=109.29/1000000![W/mm2-K] !Ecore In 2
h_11=39.1/1000000![W/mm2-K]   !Ecore Out 1
h_12=44.4/1000000![W/mm2-K]   !Ecore Out 2
h_13=195.9/1000000![W/mm2-K]  !Front 3

h_2=149.2/1000000![W/mm2-K]   !Bottom 2

!========PHYSICAL PROPERTIES============

!Material (1) Core - Ferrite

MP,DENS,1,4800/1000000000     ![kg/mm3]
MP,KXX,1,4/1000               ![W/mm-K]
MP,C,1,750                    ![J/kg-K]

!Material (2) - Copper wire winding
MP,DENS,2,4706/1000000000     ![kg/mm3]
MP,KXX,2,0.253/1000           ![W/mm-K]
MP,C,2,385                    ![J/kg-K]

!=======PHYSICAL DIMENSIONS=============

!Define Points (dimensions in mm)

w_coil=7.6

x0=0
x1=9.7
x2=9.7+w_coil
x3=x1+12.9
x4=32.6

y0=0
y1=w_coil
y2=26.8+w_coil
y3=26.8+2*w_coil

z0=0
z1=9.8
z2=32.6

!Define Keypoints

K,1,x0,y0,z1
K,2,x0,y1,z1
K,3,x0,y2,z1
K,4,x0,y3,z1
K,5,x1,y0,z1
K,6,x1,y1,z1
K,7,x1,y2,z1
K,8,x1,y3,z1
K,9,x2,y0,z1
K,10,x2,y1,z1
K,11,x2,y2,z1
K,12,x2,y3,z1
K,13,x3,y1,z1
K,14,x3,y2,z1
K,15,x4,y1,z1
K,16,x4,y2,z1


!Define Lines

L,1,2          !Line 1
L,1,5          !Line 2
L,2,6          !Line 3
L,5,6          !Line 4
L,2,3          !Line 5
L,3,7          !Line 6
L,6,7          !Line 7
L,3,4          !Line 8
L,4,8          !Line 9
L,7,8          !Line 10
L,5,9          !Line 11
L,6,10         !Line 12
L,9,10         !Line 13
L,7,11         !Line 14
L,8,12         !Line 15
L,11,12        !Line 16
L,10,11        !Line 17
L,10,13        !Line 18
L,11,14        !Line 19
L,13,14        !Line 20
L,13,15        !Line 21
L,14,16        !Line 22
L,15,16        !Line 23

!Define Areas

AL,1,2,3,4            !Area 1
AL,3,5,6,7            !Area 2
AL,8,9,10,6           !Area 3
AL,4,11,12,13         !Area 4
AL,7,12,14,17         !Area 5
AL,10,15,16,14        !Area 6
AL,18,19,20,17        !Area 7
AL,21,22,23,20        !Area 8
```

```
!Define Volumes

ALLSEL
ASEL,S,LOC,Y,Y1,Y2
VEXT,ALL,,,,,-Z1

ALLSEL
ASEL,S,LOC,X,X0,X2
ASEL,R,LOC,Z,Z1
VEXT,ALL,,,,,Z2-Z1

ALLSEL
ASEL,S,LOC,X,X3,X4
ASEL,R,LOC,Z,Z1
VEXT,ALL,,,,,Z2-Z1

!==============DIVIDE GROUPED LINES=====

ALLSEL
LSEL,S,LENGTH,,y2-y1
CM,L1,LINES

ALLSEL
LSEL,S,LENGTH,,y3-y2
CM,L2,LINES

ALLSEL
LSEL,S,LENGTH,,X1-X0
CM,L3,LINES

ALLSEL
LSEL,S,LENGTH,,X3-X2
CM,L4,LINES

ALLSEL
LSEL,S,LENGTH,,X4-X3
CM,L5,LINES

ALLSEL
LSEL,S,LENGTH,,z2-z1
CM,L6,LINES

ALLSEL
LSEL,S,LENGTH,,z1-z0
CM,L7,LINES

ALLSEL
CMSEL,S,L1
LESIZE,L1,,,26

ALLSEL
CMSEL,S,L2
LESIZE,L2,,,10

ALLSEL
CMSEL,S,L3
LESIZE,L3,,,12

ALLSEL
CMSEL,S,L4
LESIZE,L4,,,6

ALLSEL
CMSEL,S,L5
LESIZE,L5,,,12

ALLSEL
CMSEL,S,L6
LESIZE,L6,,,32

ALLSEL
CMSEL,S,L7
LESIZE,L7,,,12

!=============CREATE MESH================

!Element Type 1 - Solid 70 for All Solid
Volumes

ET,1,SOLID70

ALLSEL
VSEL,s,LOC,Z,(Z1-Z0)/2
VSEL,A,LOC,X,X3+(X4-X3)/2
VSEL,A,LOC,X,(X1-X0)/2
VSEL,R,LOC,y,y1,y2
CM,CORE,VOLU
TYPE,1
MAT,1
VMESH,ALL

ALLSEL
VSEL,S,LOC,Y,(Y1-Y0)/2
VSEL,A,LOC,Y,(Y3-Y2)/2+Y2
VSEL,A,LOC,X,(X2-X1)/2+X1
VSEL,R,LOC,Z,Z1+(Z2-Z1)/2
CM,COIL,VOLU
TYPE,1
MAT,2
VMESH,ALL

!============HEAT GENERATION==============
V_coil=(z2-z1)*(w_coil*(x2-
x0)*2+w_coil*(y2-y1))  ![mm^3]
V_CORE=20712           ![MM^3]

Q_gen=Q_coil/V_coil           ![W/mm^3]
Q_GEN_CORE=Q_CORE/V_CORE

ALLSEL
CMSEL,S,COIL
ESLV,S
BFE,ALL,HGEN,,Q_gen

ALLSEL
VSEL,S,MAT,,1
ESLV,S
BFE,ALL,HGEN,,Q_GEN_CORE

!=================CONVECTION==============

ET,2,SURF152,,,,0,1,0
KEYOPT,2,7,0
KEYOPT,2,8,4
KEYOPT,2,9,0

ET,3,SURF152,,,,0,1,0
KEYOPT,3,7,0
KEYOPT,3,8,4
KEYOPT,3,9,0

ET,4,SURF152,,,,0,1,0
KEYOPT,4,7,0
KEYOPT,4,8,4
KEYOPT,4,9,0

ET,5,SURF152,,,,0,1,0
```

```
KEYOPT,5,7,0
KEYOPT,5,8,4
KEYOPT,5,9,0

ET,6,SURF152,,,,0,1,0
KEYOPT,6,7,0
KEYOPT,6,8,4
KEYOPT,6,9,0

ET,7,SURF152,,,,0,1,0
KEYOPT,7,7,0
KEYOPT,7,8,4
KEYOPT,7,9,0

ET,8,SURF152,,,,0,1,0
KEYOPT,8,7,0
KEYOPT,8,8,4
KEYOPT,8,9,0

ET,9,SURF152,,,,0,1,0
KEYOPT,9,7,0
KEYOPT,9,8,4
KEYOPT,9,9,0

ET,10,SURF152,,,,0,1,0
KEYOPT,10,7,0
KEYOPT,10,8,4
KEYOPT,10,9,0

ET,11,SURF152,,,,0,1,0
KEYOPT,11,7,0
KEYOPT,11,8,4
KEYOPT,11,9,0

ET,12,SURF152,,,,0,1,0
KEYOPT,12,7,0
KEYOPT,12,8,4
KEYOPT,12,9,0

ET,13,SURF152,,,,0,1,0
KEYOPT,13,7,0
KEYOPT,13,8,4
KEYOPT,13,9,0

ET,14,SURF152,,,,0,1,0
KEYOPT,14,7,0
KEYOPT,14,8,4
KEYOPT,14,9,0

!Coil_1

ALLSEL
ASEL,S,LOC,Y,Y3
NSLA,S,1
N,100060,-5.2,-5.1,-5.1
TYPE,6
ESURF,100060
D,100060,TEMP,T_i1
ESEL,R,TYPE,,6
SFE,all,1,conv,0,h_4,h_4,h_4,h_4

!Coil_2

ALLSEL
ASEL,S,LOC,Z,Z1
ASEL,R,LOC,Y,Y2,Y3
NSLA,S,1
N,100040,-5.1,-5.1,-5
TYPE,4
ESURF,100040
D,100040,TEMP,T_i1
ESEL,R,TYPE,,4
SFE,all,1,conv,0,h_5,h_5,h_5,h_5

!Coil_3_1

ALLSEL
ASEL,S,LOC,X,X2
ASEL,R,LOC,Z,Z1,Z2
ASEL,R,LOC,Y,Y2,Y3
NSLA,S,1
N,100050,-5.1,-5.1,-5.1
TYPE,5
ESURF,100050
D,100050,TEMP,T_i1
ESEL,R,TYPE,,5
SFE,all,1,conv,0,h_6,h_6,h_6,h_6

!Coil_3_2

ALLSEL
ASEL,S,LOC,X,X2
ASEL,R,LOC,Z,Z1,Z2
ASEL,R,LOC,Y,Y1,Y2
NSLA,S,1
N,100130,-5.3,-5.3,-5.4
TYPE,13
ESURF,100130
D,100130,TEMP,T_i2
ESEL,R,TYPE,,13
SFE,all,1,conv,0,h_14,h_14,h_14,h_14

!Coil_3_3

ALLSEL
ASEL,S,LOC,X,X2
ASEL,R,LOC,Z,Z1,Z2
ASEL,R,LOC,Y,Y0,Y1
NSLA,S,1
N,100140,-5.3,-5.4,-5.4
TYPE,14
ESURF,100140
D,100140,TEMP,T_i3
ESEL,R,TYPE,,14
SFE,all,1,conv,0,h_15,h_15,h_15,h_15

!Coil_4

ALLSEL
ASEL,S,LOC,Z,Z1
ASEL,R,LOC,Y,Y0,Y1
NSLA,S,1
N,100010,-5.1,-5,-5
TYPE,3
ESURF,100010
D,100010,TEMP,T_i3
ESEL,R,TYPE,,3
SFE,all,1,conv,0,h_7,h_7,h_7,h_7

!Coil_5

ALLSEL
ASEL,S,LOC,Y,Y0
NSLA,S,1
N,100000,-5,-5,-5
TYPE,2
ESURF,100000
D,100000,TEMP,T_i3
```

```
ESEL,R,TYPE,,2
SFE,all,1,conv,0,h_8,h_8,h_8,h_8

!E_core_out

ALLSEL
ASEL,S,LOC,X,X0,X3
ASEL,R,LOC,Y,Y1
ASEL,R,LOC,Z,Z0,Z1
NSLA,S,1
N,100070,-5.2,-5.2,-5.1
TYPE,7
ESURF,100070
D,100070,TEMP,T_i3
ESEL,R,TYPE,,7
SFE,all,1,conv,0,h_11,h_11,h_11,h_11

ALLSEL
ASEL,S,LOC,X,X3,X4
ASEL,R,LOC,Y,Y1
NSLA,S,1
N,100080,-5.2,-5.2,-5.2
TYPE,8
ESURF,100080
D,100080,TEMP,T_i3
ESEL,R,TYPE,,8
SFE,all,1,conv,0,h_12,h_12,h_12,h_12

!E_core_in

ALLSEL
ASEL,S,LOC,X,X0,X3
ASEL,R,LOC,Y,Y2
ASEL,R,LOC,Z,Z0,Z1
NSLA,S,1
N,100090,-5.3,-5.2,-5.2
TYPE,9
ESURF,100090
D,100090,TEMP,T_i1
ESEL,R,TYPE,,9
SFE,all,1,conv,0,h_9,h_9,h_9,h_9

ALLSEL
ASEL,S,LOC,X,X3,X4
ASEL,R,LOC,Y,Y2
NSLA,S,1
N,100100,-5.3,-5.2,-5.4
TYPE,10
ESURF,100100
D,100100,TEMP,T_i1
ESEL,R,TYPE,,10
SFE,all,1,conv,0,h_10,h_10,h_10,h_10

!Bottom

ALLSEL
ASEL,S,LOC,Z,Z1
ASEL,R,LOC,X,X2,X3
NSLA,S,1
N,100110,-5.3,-5.3,-5.2
TYPE,11
ESURF,100110
D,100110,TEMP,T_i2
ESEL,R,TYPE,,11
SFE,all,1,conv,0,h_2,h_2,h_2,h_2

!Front

ALLSEL
ASEL,S,LOC,X,X3
ASEL,R,LOC,Z,Z1,Z2
NSLA,S,1
N,100120,-5.3,-5.3,-5.3
TYPE,12
ESURF,100120
D,100120,TEMP,T_i2
ESEL,R,TYPE,,12
SFE,all,1,conv,0,h_13,h_13,h_13,h_13

!=================VIII-MERGE=============
/TITLE,Merging Coincident or Equivalently
Defined Items.
ALLSEL
VPLOT

ALLSEL
NUMMRG,ALL
ALLSEL
NUMMRG,ALL
NUMCMP,ELEM

!================SOLVE================
/TITLE,SOLVING
ALLSEL
VPLOT

/SOLU
NROPT,AUTO
AUTOTS,ON
NSUBST,50
KBC,0
OUTPR,NSOL,LAST
SOLVE
FINISH
```